

# European Journal of Mineralogy

## What's in the sandwich? New P-T constraints for the (U)HP nappe stack of southern Dora-Maira Massif (Western Alps) --Manuscript Draft--

<b>Manuscript Number:</b>	ejm190006R1
<b>Article Type:</b>	Research paper
<b>Full Title:</b>	What's in the sandwich? New P-T constraints for the (U)HP nappe stack of southern Dora-Maira Massif (Western Alps)
<b>Short Title:</b>	Prograde P-T evolution of (U)HP units in the southern DMM
<b>Corresponding Author:</b>	Chiara Groppo University of Torino Torino, ITALY
<b>Corresponding Author E-Mail:</b>	chiara.groppo@unito.it
<b>Order of Authors:</b>	Chiara Groppo Simona Ferrando Manuele Gilio Serena Botta Francesco Nosenzo Gianni Balestro Andrea Festa Franco Rolfo
<b>Abstract:</b>	<p>The Brossasco-Isasca Unit (BIU) of the southern Dora-Maira Massif (DMM), Western Alps, is one of the most studied ultra-high pressure (UHP) units in the world. However, the interpretation of UHP metamorphism in the BIU is still a highly debated and challenging issue. The structural and tectonometamorphic setting of the southern DMM is described in the literature as a tectonic "sandwich", with the UHP unit in the middle, bounded by two high-pressure (HP) eclogitic units in the footwall (the San Chiaffredo Unit, SCU) and hanging wall (the Rocca Solei Unit, RSU), respectively. These three units are in turn sandwiched between two blueschist-facies units (the Pinerolo Unit, PU, at the bottom, and the Dronero-Sampeyre Unit, DSU, at the top). In contrast to the well-constrained P-T evolution of the BIU, peak P-T conditions for its bounding HP units are poorly constrained, most studies dating back to over 20 years ago and mostly relying on conventional thermobarometric methods. This study aims to update our knowledge about the P-T evolution experienced by the whole tectonometamorphic package of the southern DMM. For the first time, peak P-T conditions and prograde evolution for the five units (PU, SCU, BIU, RSU, DSU) forming the southern DMM tectonic "sandwich" are estimated using the same, internally consistent and therefore comparable, modern thermobarometric approaches. The study focuses on metapelites (i.e., garnet-bearing phengitic micaschists) and combines multi-equilibrium thermobarometry (Average PT) with the P-T pseudosection approach. Our results demonstrate that most of the southern DMM nappe stack (i.e., SCU, RSU and also the PU, that was originally considered as a blueschist-facies unit) experienced eclogite-facies metamorphism under similar peak P-T conditions (500-520°C, 20-24 kbar), and followed the same prograde path, suggesting similar burial mechanisms. The UHP BIU followed an early prograde evolution similar to that of the other eclogitic units of the southern DMM tectonic "sandwich". The attainment of UHP peak conditions occurred through an earlier steep, almost isothermal increase in pressure and a later increase in temperature. The DSU is the only unit of the southern DMM nappe stack that did not experience eclogite-facies metamorphism (peak metamorphism at blueschist-facies conditions: 450-470 °C, 17-18 kbar) and it is separated from the eclogitic units by a shear zone (the Valmala Shear Zone), whose interpretation requires further studies. These new data represent the inescapable starting point for any conceptual model aiming for a deeper understanding of the subduction/exhumation processes of UHP</p>

	continental units.
<b>Keywords:</b>	(U)HP metamorphism; southern Dora-Maira Massif; peak P-T conditions; prograde evolution; P-T pseudosections
<b>Manuscript Region of Origin:</b>	ITALY
<b>Requested Editor:</b>	Patrick Cordier, Editor-in-Chief
<b>Additional Information:</b>	
<b>Question</b>	<b>Response</b>
<b>Author Comments:</b>	
<b>Response to Reviewers:</b>	<p>Dear Editor,  the two reviewers and your own constructive comments have been carefully considered in order to improve the revised version of our manuscript. Please, find in the "ANSWERS TO EDITOR AND REVIEWERS".pdf file how and where the editor + reviewers comments have been incorporated in the manuscript. We hope that the manuscript now meets your approval for publication in European Journal of Mineralogy.</p> <p>With best regards,  Chiara Groppo and co-authors</p>

1 **Cover Page**

2

3 Title: **What's in the sandwich? New P-T constraints for the (U)HP nappe stack of southern Dora-**  
4 **Maira Massif (Western Alps)**

5

6

7 Running title

8 **Prograde P-T evolution of (U)HP units in the southern DMM**

9

10 **Detailed plan of the article:**

11 1. Introduction

12 2. Geological setting

13 3. Methods

14 3.1 Micro-X-ray fluorescence ( $\mu$ -XRF) maps

15 3.2 Mineral chemistry

16 3.3 Pseudosection modelling

17 3.4 Optimal thermobarometry

18 4. Petrography and mineral chemistry

19 4.1 Sample DM 1485 (PU)

20 4.2 Sample DM1667c (SCU)

21 4.3 Sample DM1281 (BIU)

22 4.4 Sample DM1504 (RSU)

23 4.5 Sample DM1565 (DSU)

24 5. Resulting P-T evolution

25 5.1 Sample DM1485 (PU)

26 5.2 Sample DM1667c (SCU)

27 5.3 Sample DM1281 (BIU)

28 5.4 Sample DM1504 (RSU)

29 5.5 Sample DM1565 (DSU)

30 6. Discussion

31 6.1 New constraints on the prograde evolution of the tectonic units in the southern DMM

32 6.1.1 Prograde evolution of the HP units bounding the UHP BIU

33 6.1.2 Prograde P-T path revised for the UHP BIU

34 6.2 Implications for the geodynamic interpretation of the southern DMM

35 Acknowledgements

36 References

37 Figure captions

38

39 **Corresponding author:**

40 Chiara Groppo

41 Dept. of Earth Sciences, University of Torino

42 Via Valperga Caluso, 35, 10125 Torino (Italy)

43 [chiara.groppo@unito.it](mailto:chiara.groppo@unito.it)

44 Tel. +39/0116705106

45 Fax: +39/0116705128

46 **Title Page**

47

48 **What's in the sandwich? New P-T constraints for the (U)HP nappe stack of southern Dora-**  
49 **Maira Massif (Western Alps)**

50

51

52

53

54 Chiara Groppo<sup>1,2,\*</sup>, Simona Ferrando<sup>1</sup>, Manuele Gilio<sup>1</sup>, Serena Botta<sup>1</sup>, Francesco Nosenzo<sup>1</sup>, Gianni  
55 Balestro<sup>1</sup>, Andrea Festa<sup>1</sup>, Franco Rolfo<sup>1,2</sup>

56

57

58 <sup>1</sup>Department of Earth Sciences, University of Torino, via Valperga Caluso 35, 10125 Torino, Italy

59 <sup>2</sup>CNR-IGG, via Valperga Caluso 35, 10125 Torino, Italy

60 \*Corresponding author: chiara.groppo@unito.it

61

62 **Abstract**

63 The Brossasco-Isasca Unit (BIU) of the southern Dora-Maira Massif (DMM), Western Alps, is one of the most  
64 studied ultra-high pressure (UHP) units in the world. However, the interpretation of UHP metamorphism in  
65 the BIU is still a highly debated and challenging issue. The structural and tectonometamorphic setting of the  
66 southern DMM is described in the literature as a tectonic “sandwich”, with the UHP unit in the middle,  
67 bounded by two high-pressure (HP) eclogitic units in the footwall (the San Chiaffredo Unit, SCU) and hanging  
68 wall (the Rocca Solei Unit, RSU), respectively. These three units are in turn sandwiched between two  
69 blueschist-facies units (the Pinerolo Unit, PU, at the bottom, and the Dronero-Sampeyre Unit, DSU, at the  
70 top). In contrast to the well-constrained P-T evolution of the BIU, peak P-T conditions for its bounding HP  
71 units are poorly constrained, most studies dating back to over 20 years ago and mostly relying on  
72 conventional thermobarometric methods. This study aims to update our knowledge about the P-T evolution  
73 experienced by the whole tectonometamorphic package of the southern DMM. For the first time, peak P-T  
74 conditions and prograde evolution for the five units (PU, SCU, BIU, RSU, DSU) forming the southern DMM  
75 tectonic “sandwich” are estimated using the same, internally consistent and therefore comparable, modern  
76 thermobarometric approaches. The study focuses on metapelites (*i.e.*, garnet-bearing phengitic micaschists)  
77 and combines multi-equilibrium thermobarometry (Average PT) with the P-T pseudosection approach. Our  
78 results demonstrate that most of the southern DMM nappe stack (*i.e.*, SCU, RSU and also the PU, that was  
79 originally considered as a blueschist-facies unit) experienced eclogite-facies metamorphism under similar  
80 peak P-T conditions (500-520°C, 20-24 kbar), and followed the same prograde path, suggesting similar burial  
81 mechanisms. The UHP BIU followed an early prograde evolution similar to that of the other eclogitic units of  
82 the southern DMM tectonic “sandwich”. The attainment of UHP peak conditions occurred through an earlier  
83 steep, almost isothermal increase in pressure and a later increase in temperature. The DSU is the only unit  
84 of the southern DMM nappe stack that did not experience eclogite-facies metamorphism (peak  
85 metamorphism at blueschist-facies conditions: 450-470 °C, 17-18 kbar) and it is separated from the eclogitic  
86 units by a shear zone (the Valmala Shear Zone), whose interpretation requires further studies. These new  
87 data represent the inescapable starting point for any conceptual model aiming for a deeper understanding  
88 of the subduction/exhumation processes of UHP continental units.

89  
90 **Key-words**

91 (U)HP metamorphism; southern Dora-Maira Massif; peak P-T conditions; prograde evolution; P-T  
92 pseudosections

93

## 94 **1. Introduction**

95 The first discovery, more than 30 years ago, of coesite in continental crustal rocks (Chopin, 1984; Smith,  
96 1984), demonstrated the possibility for continental crust to reach ultra-high pressure (UHP) conditions.  
97 However, the geodynamic processes responsible for the formation and exhumation of continental UHP units  
98 are still debated (*e.g.*, Schenker *et al.*, 2015; Reuber *et al.*, 2016; Solarino *et al.*, 2018). Conceptual and  
99 numerical models that try to explain how a continental crustal unit can reach (and can be exhumed from)  
100 UHP conditions are calibrated against geological and petrological data available from the tectonic nappe  
101 stack which includes the UHP unit itself (*e.g.*, Li *et al.*, 2010; Burov *et al.*, 2014; Schmalholz *et al.*, 2014;  
102 Gerya, 2015; Schenker *et al.*, 2015). Precise knowledge of peak pressure and temperature (P-T) conditions  
103 experienced by both the UHP unit and its adjacent, often high-P (HP) units is therefore the crucial starting  
104 point to test the validity of the models (*e.g.*, Manzotti *et al.*, 2015, 2018).

105 The Brossasco-Isasca Unit (BIU) of the southern Dora-Maira Massif (DMM) in Western Alps, is one of  
106 the most studied UHP units worldwide and has been widely used in the past as a natural laboratory to  
107 discover new UHP minerals and to investigate metamorphic processes occurring during subduction at  
108 extreme pressures (*e.g.*, Chopin & Ferraris, 2003; Schertl & O'Brien, 2013 and references therein). The models  
109 assuming subduction of continental crust to mantle depths (*e.g.*, Chemenda *et al.*, 1995; Chopin, 2003;  
110 Stöckhert & Gerya, 2005; Gerya & Stöckhert, 2006; Yamato *et al.*, 2008; Butler *et al.*, 2013) were proposed  
111 after the discovery of coesite in the BIU. Decades later, the alternative idea of tectonic overpressure  
112 explaining UHP tectonics arose again in the southern DMM (*e.g.*, Ford *et al.*, 2006; Schmalholz *et al.*, 2014;  
113 Schmalholz & Duretz, 2015; Schenker *et al.*, 2015). More than 30 years after its discovery, the interpretation  
114 of UHP metamorphism in the BIU still remains a challenge for many generations of geoscientists.

115 In the southern DMM, the UHP BIU is tectonically sandwiched between two quartz-eclogite facies  
116 units, the lower San Chiaffredo Unit (SCU) and the upper Rocca Solei Unit (RSU), which are in turn bounded  
117 by two blueschist-facies units, the Pinerolo Unit (PU) at the bottom and the Dronero-Sampeyre Unit (DSU) at  
118 the top of the tectonometamorphic package (Fig. 1). In contrast to the well-constrained P-T evolution of the  
119 BIU (*e.g.*, Ferrando *et al.*, 2017 and references therein), peak P-T conditions for its adjacent Units are poorly  
120 constrained, most studies dating back to over 20 years ago and mostly relying on conventional  
121 thermobarometric methods (*e.g.*, Chopin *et al.*, 1991; Michard *et al.*, 1993; Compagnoni *et al.*, 1995).  
122 Notably, many of these studies, which still represent milestones for all those interested in the interpretation  
123 of the tectonometamorphic evolution and architecture of the southern DMM, were carried out by Christian  
124 Chopin and co-workers. It is therefore a great pleasure for us to contribute to this Special Issue dedicated to  
125 Christian Chopin, with the aim of updating his legacy, taking advantage of the modern petrological methods  
126 and exploiting the great amount of data collected by our group over last decades.

127 With these premises in mind, this study constrains the prograde-to-peak evolution experienced by  
128 the HP units bounding the UHP BIU. For the first time, peak P-T conditions for all five units (PU, SCU, BIU,  
129 RSU, DSU) forming the southern DMM tectonic “sandwich” (Compagnoni & Rolfo, 2003) are estimated using  
130 the same, internally consistent and therefore comparable, modern thermobarometric approaches. The study  
131 focuses on metapelites (*i.e.*, garnet-bearing phengitic micaschists) because they are widely exposed in all the  
132 investigated units and preserve the (U)HP assemblages well. Thermobarometric estimates are obtained  
133 combining multi-equilibrium thermobarometry (Average PT) and/or the P-T pseudosection approach applied  
134 to five samples (one for each unit). Concerning the HP units bounding the UHP BIU, our results confirm peak-  
135 T already known from the literature, but indicate systematically higher peak-P. The prograde path of the BIU  
136 is also significantly revised, with possible implications for the interpretation of burial mechanisms in the  
137 whole southern DMM tectonic “sandwich”.

138 In our opinion, these new data represent the inescapable starting point for any model aimed at a  
139 deeper understanding of the processes responsible for the attainment and preservation of UHP conditions

140 in continental crust; however, further studies are needed in order to understand if (and how) the studied  
141 units shared part of their prograde evolution at HP to UHP conditions or if (and how) they were coupled  
142 during exhumation.

143

## 144 **2. Geological setting**

145 The Dora-Maira Massif (DMM) in the Western Alps, represents part of the subducted-exhumed European  
146 continental margin (*e.g.*, Michard *et al.*, 1996). It is now stacked in the Alpine orogenic wedge (Lardeaux *et al.*,  
147 2006), wherein it was overthrust by meta-ophiolite units of the Piedmont Zone (Balestro *et al.*, 2018, and  
148 references therein). The southern portion of the DMM is a pile of imbricated thrust sheets, resulting from  
149 Alpine tectonic juxtaposition and metamorphic reworking of slices of Variscan continental crust and of  
150 Permian igneous bodies (*e.g.*, Vialon, 1966; Henry, 1990; Chopin *et al.*, 1991; Michard *et al.*, 1993, 1995;  
151 Turello, 1993; Sandrone *et al.*, 1993; Balestro *et al.*, 1995; Compagnoni *et al.*, 1995, 2012; Compagnoni &  
152 Rolfo, 1999, 2003; Groppo, 2002; Compagnoni *et al.*, 2004, 2012; Botta, 2015; Nosenzo, 2018). Relics of both  
153 amphibolite-facies Variscan metamorphism and Permian contact metamorphism are locally still preserved  
154 (*e.g.*, Biino & Compagnoni, 1992; Compagnoni *et al.*, 1995; Compagnoni & Rolfo, 2003; Groppo *et al.*, 2006,  
155 2007b).

156 In the area between the Po Valley to the north and the Maira Valley to the south, the following  
157 tectonometamorphic units are distinguished from the lower to the upper structural position (Fig. 1): (i) the  
158 Pinerolo Unit (PU) is a monometamorphic unit that experienced Alpine epidote-blueschist facies  
159 metamorphism (*e.g.*, Chopin *et al.*, 1991; Avigad *et al.*, 2003); (ii) the San Chiaffredo Unit (SCU) is a portion  
160 of pre-Alpine continental crust (Variscan amphibolite-facies basement intruded by Permian granitoids) that  
161 reached quartz-eclogite facies peak during Alpine metamorphism (Compagnoni & Rolfo, 2003); (iii) the  
162 Brossasco-Isasca Unit (BIU) is lithologically similar to the SCU but experienced Alpine peak P-T conditions in  
163 the coesite-eclogite facies (diamond stability field; *e.g.*, Schertl *et al.*, 1991; Nowlan *et al.*, 2000; Rubatto &  
164 Hermann, 2001; Hermann, 2003; Ferraris *et al.*, 2005; Di Vincenzo *et al.*, 2006; Castelli *et al.*, 2007; Groppo  
165 *et al.*, 2007a; Ferrando *et al.*, 2009; Gauthiez-Putallaz *et al.*, 2016); (iv) the Rocca Solei Unit, lithologically  
166 similar to the BIU and the SCU, experienced Alpine peak P-T conditions at quartz-eclogite facies conditions  
167 (Chopin *et al.*, 1991; Matsumoto & Hirajima, 2000); (v) the Dronero-Sampeyre Unit (DSU) includes  
168 polymetamorphic schists (Henry, 1990; Chopin *et al.*, 1991) and a monometamorphic Permian volcano-  
169 detrital sequence (Vialon, 1966; Chopin *et al.*, 1991; Michard *et al.*, 1995), both of which experienced Alpine  
170 peak P-T conditions at epidote-blueschist facies (Chopin *et al.*, 1991). The DSU is separated from the  
171 structurally underlying RSU by a shear zone, hundreds of metres thick, consisting of the tectonic juxtaposition  
172 of meta-ophiolite and metasediment slices (Valmala Shear Zone; *i.e.*, the “ophiolitiferous band” of Henry *et al.*,  
173 1993). The term “tectonic sandwich” is hereafter used to indicate the whole package of juxtaposed  
174 tectonometamorphic units of southern DMM described above. All these units have been overprinted by a  
175 late-Alpine greenschist-facies recrystallization, which pervasively reworked and extensively obliterated the  
176 former (U)HP metamorphic mineral assemblages.

177 Sample locations are reported in Fig. 1 and additional details are given in the Supplementary material.

178

## 179 **3. Methods**

### 180 **3.1 Micro-X-ray fluorescence ( $\mu$ -XRF) maps**

181 Qualitative major element X-ray maps of the entire thin sections were acquired using a micro-XRF Eagle III-  
182 XPL spectrometer equipped with an EDS Si(Li) detector and with an EdaxVision32 microanalytical system at  
183 the Department of Earth Sciences, University of Torino. Operating conditions were: 100 ms counting time,  
184 40 kV accelerating voltage, and a probe current of 900  $\mu$ A. A spatial resolution of about 65  $\mu$ m in both x and

185 y directions was used. Quantitative modal amounts of each mineral phase were obtained by processing the  
186 maps with the software Petromod (Cossio *et al.*, 2002). For each sample, the processed X-ray maps are  
187 reported in Fig. 2. Additional microstructural details, at greater magnification, are given in Figs. 3-5. Mineral  
188 abbreviations are after Whitney & Evans (2010), except white mica (Wm) and phengite (Phe).  
189

### 190 **3.2 Mineral chemistry**

191 The rock-forming minerals were analyzed with a Jeol JSMT300LV Scanning Electron Microscope at the  
192 Department of Earth Sciences, University of Torino. The instrument was equipped with an energy dispersive  
193 spectrometry (EDS) Energy 200 system and an SDD X-Act3 detector (Oxford Inca Energy). Operating  
194 conditions were: 50 s counting time, 15 kV accelerating voltage, spot size 2  $\mu\text{m}$ . SEM-EDS quantitative data  
195 were acquired and processed using the Microanalysis Suite Issue 12, INCA Suite version 4.01; natural mineral  
196 standards were used to calibrate the raw data; the  $\phi\rho\rho Z$  correction (Pouchou & Pichoir, 1988) was applied.  
197 Tables SM1 and SM2-SM6, freely available online as Supplementary Material linked to this article on the GSW  
198 website of the journal, <https://pubs.geoscienceworld.org/eurljmin/>, summarize the compositional variations  
199 (Table SM1) and the representative chemical compositions for the main minerals in each sample; Figs. 6-7  
200 and SM1 show the composition of garnet and phengite. For practical purposes, the term phengite is used in  
201 the following to indicate phengitic white mica with Si > 3.20 a.p.f.u. (on the basis of 11 oxygens), whereas  
202 muscovite is used for phengitic white mica with Si < 3.20 a.p.f.u.  
203

### 204 **3.3 Pseudosection modelling**

205 The pseudosection modeling approach was applied to each metapelite sample, excluding DM1565. Bulk-rock  
206 composition of each sample (Table 1) was calculated by combining estimated mineral modes with mineral  
207 chemistry (see above). Determination of an effective bulk composition for sample DM1565 (DSU) was  
208 problematic because: (i) the fine-grained nature of Alpine Grt<sub>2</sub> hampered its correct quantification from  
209 micro-XRF maps; (ii) the presence of pre-Alpine garnet porphyroblasts (Grt<sub>1</sub>), that should be subtracted from  
210 the bulk-composition effectively reacting during Alpine metamorphism, makes the conventional bulk-rock  
211 analysis (*e.g.*, XRF or ICP-MS) not suitable.

212 For each considered sample, three P-T isochemical phase diagrams have been calculated (*i.e.*, a total  
213 of 12 pseudosections) considering the fractionation effects on the bulk-composition due to the growth of  
214 zoned garnet porphyroblasts. Each pseudosection was used to model: (i) P-T conditions for garnet core  
215 growth (measured bulk-composition: MBC), (ii) P-T conditions for garnet mantle growth (MBC minus garnet  
216 cores), and (iii) P-T conditions for garnet rim growth (MBC minus garnet cores + mantles) (Table 1).

217 The P-T isochemical phase diagrams were calculated in the system MnNKCFMASTOH (MnO-Na<sub>2</sub>O-  
218 K<sub>2</sub>O-CaO-FeO-MgO-Al<sub>2</sub>O<sub>3</sub>-SiO<sub>2</sub>-TiO<sub>2</sub>-Fe<sub>2</sub>O<sub>3</sub>-H<sub>2</sub>O), except for sample DM1281 (BIU), for which Fe<sup>3+</sup> was  
219 neglected, because Fe<sup>3+</sup>-rich oxides are absent and the amount of Fe<sup>3+</sup> in the analyzed minerals is very low.  
220 The pseudosections were calculated using Perplex 6.8.1 (version March 2018; Connolly, 1990, 2005, 2009),  
221 the internally consistent thermodynamic dataset of Holland & Powell (2011) (ds62) and the equation of state  
222 for H<sub>2</sub>O of Holland & Powell (1998). The following solution models were used: garnet, chlorite, chloritoid,  
223 staurolite, white mica, biotite and ilmenite (White *et al.*, 2014), omphacite (Green *et al.*, 2007), amphibole  
224 (Green *et al.*, 2016), carpholite (Smye *et al.*, 2010), feldspar (Fuhrman & Lindsley, 1988) and epidote (Holland  
225 & Powell, 2011). Quartz, lawsonite, kyanite, rutile and titanite were considered as pure phases. The fluid was  
226 usually considered as pure H<sub>2</sub>O ( $a_{\text{H}_2\text{O}}=1$ ), but a reduced  $a_{\text{H}_2\text{O}}=0.4$  was considered in the pseudosection that  
227 models the garnet rim growth in DM1281 (BIU) because experimental and fluid inclusions studies (Sharp *et al.*,  
228 1993; Hermann, 2003; Ferrando *et al.*, 2009) demonstrated that, at the UHP peak, the activity of H<sub>2</sub>O was  
229 strongly reduced by the abundance of dissolved species.



230

### 231 **3.4 Optimal thermobarometry**

232 The THERMOCALC “Average PT” (AvPT) method (*i.e.*, “Optimal thermobarometry”: Powell & Holland, 1994)  
233 was applied to all the samples. THERMOCALC v3.40 and the Holland & Powell (2011) dataset (ds62) were  
234 used. Activity-composition relationships were calculated using the software AX. The method was applied to  
235 the peak assemblage for all the samples, except sample DM1281 (BIU), for which it was applied to the late  
236 prograde assemblage (see Section 4.3). Used sets of mineral compositions and of independent reactions are  
237 given in Tables SM2-SM7. AvPT results are discussed in terms of weighted means (*i.e.*, values with smaller  
238 errors contribute more than values with larger errors) and are presented in Table 2.

239

## 240 **4. Petrography and mineral chemistry**

### 241 **4.1 Sample DM 1485 (PU)**

242 This medium- to coarse-grained micaschist consists of white mica (mostly phengite; 42%), garnet (20%),  
243 chlorite (19%), quartz (13%) and minor chloritoid (2%) (Fig. 2). Retrograde chlorite, plagioclase (3%) and  
244 minor biotite, as well as accessory magnetite, rutile and ilmenite also occur. The main foliation ( $S_m$ ) is defined  
245 by preferred orientation of phengite and chlorite, that form continuous pluri-mm -thick layers alternated  
246 with discontinuous pluri-mm -thick quartzitic layers (Fig. 2). An earlier schistosity ( $S_{m-1}$ ), defined by the  
247 preferred orientation of white mica and chlorite, is still preserved in microlithons.

248 Garnet porphyroblasts, up to several millimetres in size, are syn-kinematic with respect to  $S_m$  and  
249 show a snow-ball structure (Fig. 3a); the rotated internal foliation, continuous with the external  $S_m$ , is defined  
250 by inclusions of quartz, relict chloritoid, and minor white mica and chlorite (Fig. 3b). Quartz, phengite and  
251 chlorite occur in the pressure shadows of garnet. Garnet porphyroblasts are strongly zoned (Fig. 6a and Table  
252 SM1), with a reddish core and a pinkish rim.

253 Phengite defines the  $S_m$  and rarely occurs, in association with paragonite and relict chloritoid, in  
254 polymineralic inclusions within garnet core and mantle (Fig. 3b). A few retrograde muscovite flakes occur in  
255 matrix and in polymineralic inclusions within garnet. Paragonite is only observed in polymineralic inclusions  
256 in garnet, always associated with (or replacing) chloritoid; its prograde vs. retrograde nature is ambiguous.  
257 Bluish-greenish chloritoid is only preserved as inclusions in garnet porphyroblasts (Fig. 3a,b), but not in the  
258 matrix. Its composition changes according to the microstructural position within garnet (Table SM1). Chlorite  
259 is mostly in equilibrium with  $S_m$ , but a late chlorite generation replaces garnet along fractures. Chlorite rim is  
260 locally partially replaced by fine-grained biotite. Plagioclase (albite to oligoclase) occurs as large (pluri-mm)  
261 blasts overgrowing the  $S_m$  and it is thus interpreted as a retrograde phase.

262 Among the accessories, retrograde mm-sized magnetite exclusively occurs in the matrix (Fig. 2).  
263 Rutile and ilmenite within garnet core, mantle and rim appear in equilibrium, whereas in the matrix rutile is  
264 rimmed by ilmenite.

265

### 266 **4.2 Sample DM1667c (SCU)**

267 This garnet-bearing phengitic micaschist has a strongly heterogeneous grain size. It shows a mm-thick banded  
268 structure, with continuous medium- to coarse-grained phengite-rich layers alternating with fine- to medium-  
269 grained discontinuous quartz-rich layers (Fig. 2). It consists of white mica (mostly phengite: 42%), garnet  
270 (30%), quartz (18%) and minor chloritoid (1%). Retrograde chlorite (7%), epidote (1%), minor biotite, and  
271 accessory magnetite, rutile, ilmenite, tourmaline and apatite also occur. The main foliation ( $S_m$ ) is defined by  
272 the preferred orientation of white mica.

273 Garnet porphyroblasts are centimetres to pluri-cm in size in the coarse-grained layers, and  
274 millimetres to pluri-mm in the finer-grained layers (Fig. 2). Garnet is pre- to syn-kinematic with respect to the

275  $S_m$ , being mostly enveloped by the main schistosity, but with the rim that appears in equilibrium with it.  
276 Garnet porphyroblasts are microstructurally and chemically zoned (Fig. 6b). Garnet core and mantle are large,  
277 often asymmetric, and crowded with inclusions, whereas rim is thin and with few inclusions. Fine-grained  
278 inclusions in garnet core consist of epidote (Fig. 3d), chlorite and chloritoid; inclusions in garnet mantle are  
279 medium-grained and mostly consist of chloritoid (Fig. 3c) and white mica. Garnet rim includes few phengite  
280 flakes and box-shaped pseudomorphs after former lawsonite, consisting of a fine-grained aggregate of  
281 epidote, muscovite, paragonite and chlorite (Fig. 3e). A thin (100-300  $\mu\text{m}$ ) and discontinuous outer rim  
282 slightly enriched in Mn has been interpreted as due to local retrograde re-equilibration.

283 Phengite defines the  $S_m$  and is locally included in garnet. Less abundant retrograde muscovite  
284 overgrows the main foliation and replaces chloritoid inclusions within garnet. Paragonite only occurs as  
285 inclusion in garnet, associated with (or replacing) chloritoid, and as pseudomorphs after probable lawsonite;  
286 therefore, it has been interpreted as both prograde and retrograde phase. Chloritoid is mostly included in  
287 garnet mantle (Fig. 3c), rarely in core and rim, and it is absent from the matrix. It is locally partially to  
288 completely replaced by an aggregate of white mica (muscovite  $\pm$  phengite + paragonite) (Fig. 3c).

289 Epidote and chlorite occur in two different generations. Prograde epidote (often with an allanitic  
290 core) and chlorite are included in garnet core and mantle (Fig. 3d). Retrograde epidote occurs as few fine-  
291 grained idiomorphs in matrix and in pseudomorphs after lawsonite included in garnet rim, whereas late chlorite  
292 mostly replaces garnet porphyroblasts along fractures and rims. Late biotite partially replaces white mica and  
293 chlorite at their rims.

294 Among accessories, mm-sized retrograde magnetite only occurs in the matrix. Rutile and ilmenite  
295 occur as inclusions within garnet porphyroblasts; in the matrix rutile is rimmed by ilmenite. Apatite and  
296 tourmaline are included in garnet.

297

### 298 **4.3 Sample DM1281 (BIU)**

299 This sample consists of white mica (mostly phengite, 41%), quartz (24%), garnet (21%), kyanite (10%), jadeite  
300 (3%) and minor chloritoid, staurolite and chlorite (Fig. 2). Albite and pyrophyllite are retrograde phases,  
301 whereas rutile, tourmaline and apatite are the main accessory minerals. The grain size is markedly  
302 heterogeneous, with pluri-mm garnet and kyanite porphyroblasts set in a fine-grained matrix mostly  
303 consisting of phengite and quartz (Fig. 2). The main schistosity ( $S_m$ ) is defined by mm-thick, continuous  
304 phengitic layers, alternating with discontinuous quartzitic layers of similar thickness.

305 Garnet porphyroblasts are microstructurally and chemically zoned (Fig. 6c). Garnet core and mantle  
306 are large, often asymmetric, and crowded with inclusions, whereas rim is thin and with few inclusions (Fig.  
307 4a). Garnet rim appears in equilibrium with  $S_m$ . Inclusions in garnet core are fine-grained and polymineralic;  
308 garnet mantle includes both fine-grained polymineralic inclusions and medium-grained monocrystalline  
309 inclusions; garnet rim contains few medium-grained monocrystalline inclusions. Polymineralic inclusions in  
310 garnet core mostly consist of chloritoid, paragonite, chlorite, staurolite and rare muscovite, whereas those  
311 observed in garnet mantle contain also kyanite and does not contain potassic white mica (Fig. 4d,e).  
312 Monocrystalline inclusions in garnet mantle are represented by pseudomorphs after jadeite and glaucophane  
313 (Fig. 4f, g), kyanite and quartz, whereas those in garnet rim consist of kyanite, phengite and quartz.  
314 Polycrystalline aggregates of quartz surrounded by radial cracks, interpreted as deriving from inversion of  
315 coesite, are located at the transition between garnet mantle and rim (Fig. 4a).

316 Phengite defines the  $S_m$  and is locally included in garnet rim. Retrograde muscovite is scarce and its  
317 occurrence is limited to the pseudomorphs after jadeite and glaucophane. A few prograde muscovite flakes  
318 are preserved in the polymineralic inclusions within garnet core. Paragonite is common in the polymineralic  
319 inclusions hosted within garnet core and mantle (Fig. 4e), where it probably has a prograde nature.

320 At least three different generations of kyanite have been recognized: i) large (pluri-mm)  
321 porphyroblasts enveloped by the main foliation (Fig. 4b); ii) smaller idioblasts in equilibrium with the  $S_m$  (Fig.  
322 4b); iii) local very fine-grained acicular crystals rimming the large kyanite porphyroblasts. Jadeite and  
323 glaucophane are not preserved, but are pseudomorphically replaced by retrograde phases. Pseudomorphs  
324 after jadeite, occurring both in the matrix (Fig. 4c) and as inclusion in garnet mantle (Fig. 4g), consist of a very  
325 fine-grained aggregate of albite + pyrophyllite + muscovite. Lozenge-shaped pseudomorphs after  
326 glaucophane have been observed only as inclusions in garnet mantle (Fig. 4f) and consist of a very fine-  
327 grained aggregate of paragonite + muscovite + minor biotite.

328 Chloritoid, chlorite and staurolite only occur in the fine-grained polymineralic inclusions within garnet  
329 core and mantle (Fig. 4d,e). Chlorite is a prograde phase and the  $X_{Mg}$  of the chlorite included in garnet mantle  
330 is higher than that of the chlorite included in garnet core (Table SM1). Chloritoid is generally associated with  
331 paragonite and chlorite. Staurolite is only present as inclusion in both garnet core and mantle, where it mostly  
332 occurs in association with kyanite, paragonite and chlorite, more rarely with chloritoid. Microstructural  
333 relationships clearly show that staurolite grew at the expense of kyanite, often preserved as rounded relics  
334 partially rimmed by staurolite (Fig. 4e).

335 Accessory rutile, tourmaline and apatite occur in the matrix and as inclusion in garnet  
336

#### 337 4.4 Sample DM1504 (RSU)

338 This fine- to coarse-grained, garnet-bearing phengitic micaschist consists of white mica (mostly phengite, 49  
339 % and paragonite, 6%), quartz (20%), chloritoid (12%) and garnet (8%) (Fig. 2), with minor amounts of  
340 glaucophane and jadeite (almost completely replaced by retrograde phases). Retrograde chlorite (3%),  
341 epidote (1%) and biotite, and accessory rutile, ilmenite, magnetite and apatite also occur. The main foliation  
342 ( $S_m$ ) is defined by mm- to pluri-mm -thick, continuous, micaceous layers alternated with mm-thick,  
343 discontinuous, quartzitic layers. Relics of an earlier  $S_{m-1}$  schistosity are locally preserved in microlithons and  
344 are defined by the alignment of white mica.

345 Mm- to pluri-mm -sized garnet porphyroblasts are partially enveloped by the  $S_m$ , but their rim  
346 appears in equilibrium with  $S_m$  (*i.e.*, garnet is pre- to syn-kinematic with respect to  $S_m$ ). They include an  
347 internal rotated foliation mostly defined by quartz and chloritoid. Garnet core and mantle are large and rich  
348 of inclusions, whereas garnet rim is thin and with few inclusions (Fig. 5a-c). Inclusions in garnet are either  
349 polymineralic or monocrystalline. Polymineralic inclusions mostly consist of chloritoid + white micas  
350 (phengite ± paragonite ± muscovite) (Fig. 5b). Relics of glaucophane + jadeite, partially replaced by paragonite  
351 + albite ± muscovite, have been observed at the transition between garnet mantle and garnet rim (Fig. 5b).  
352 Garnet core and mantle locally include tabular-shaped aggregates of epidote + quartz + paragonite or  
353 phengite (Fig. 5c), possibly representing pseudomorphs after former lawsonite. Monocrystalline inclusions  
354 mostly consist of quartz, chloritoid and minor phengite.

355 Phengite defines the  $S_m$  and is locally included in garnet and chloritoid. Retrograde paragonite and  
356 muscovite occur both in the matrix and as inclusions in garnet. In the matrix, paragonite forms large flakes  
357 statically overgrowing the  $S_m$  (Fig. 2). When included in garnet, paragonite and muscovite generally replace  
358 other phases, such as glaucophane, jadeite or chloritoid. Chloritoid occurs both in the matrix and as inclusion  
359 in garnet (Fig. 5a). In the matrix, it forms medium-grained bluish-greenish nematoblasts aligned with the  $S_m$   
360 and it is slightly zoned. Rare glaucophane and jadeite relics are included in garnet mantle/rim (Fig. 5b).

361 Epidote, chlorite, albite and biotite are retrograde phases. Epidote within garnet occurs in tabular-  
362 shaped aggregates, in association with quartz and white micas, interpreted as deriving from former lawsonite  
363 (Fig. 5c). In the matrix, it forms few fine-grained idioblasts, often with an allanitic core. Aggregates of chlorite  
364 statically overgrows the  $S_m$  and replaces garnet along fractures and at the rim. Its rim is locally replaced by  
365 biotite. Albite occurs as replacement of jadeite and glaucophane.

366 Rutile mostly occurs as inclusion in garnet, whereas it is pervasively replaced by ilmenite in the  
367 matrix. Retrograde magnetite is fine-grained and widespread in the matrix, and it is strongly oxidized. Apatite  
368 occurs as relatively large grains both in the matrix and included in garnet.

369

#### 370 **4.5 Sample DM1565 (DSU)**

371 This garnet-bearing phengitic micaschist consists of white mica (mostly phengite, 54% and paragonite, 8%),  
372 quartz (26%), garnet (5%) and chloritoid (3%) (Fig. 2). Retrograde chlorite (3%) and biotite and accessory  
373 rutile, ilmenite and tourmaline also occur. The main schistosity ( $S_m$ ) is defined by pluri-mm thick, continuous,  
374 micaceous layers alternating with mm-thick quartzitic layers. Large (pluri-mm) garnet porphyroblasts are  
375 preferentially set in the fine-grained micaceous layers (Fig. 2).

376 In contrast to the other samples, this metapelite preserves mineralogical evidence of a  
377 polymetamorphic evolution. Two different garnet generations can be, in fact, recognized: (i) large  
378 porphyroblasts (Fig. 5d) enveloped by the  $S_m$ , interpreted as amphibolite-facies Variscan garnets ( $Grt_1$ ); (ii)  
379 small (ca. 100  $\mu m$ ) idioblasts in equilibrium with  $S_m$  and a thin and discontinuous corona around  
380 porphyroblastic  $Grt_1$  (Fig. 5e), both interpreted as Alpine garnets ( $Grt_2$ ). The strongly-fractured  $Grt_1$  is  
381 chemically zoned (Table SM1). Locally it is poikiloblastic and includes quartz, white mica, ilmenite and minor  
382 staurolite, now replaced by fine-grained pseudomorphic aggregates of white mica + chloritoid. The small  $Grt_2$   
383 idioblasts are also zoned and include very fine-grained quartz (Fig. 6e and Table SM1).

384 Phengite defines the  $S_m$  and it also occurs at the rim of the chloritoid-bearing pseudomorphs after  
385 former staurolite. Minor retrograde muscovite and paragonite occur in the matrix. Chloritoid mostly  
386 constitutes large (pluri-mm) fine-grained aggregates enveloped by the  $S_m$  and interpreted as pseudomorphs  
387 after pre-Alpine porphyroblastic staurolite (Fig. 5f) (see also Henry, 1990; Chopin *et al.*, 1991). These  
388 pseudomorphs also contain white mica (phengite + muscovite + paragonite), generally concentrated toward  
389 the rim. Chloritoid also forms minor idioblasts aligned with the  $S_m$  or partially overgrowing it.

390 Retrograde chlorite occurs as large flakes statically overgrowing the  $S_m$  and partially replacing garnet  
391 at the rim and along fractures. Biotite is limited to late and discontinuous shear bands crosscutting the main  
392 foliation. Accessory ilmenite is included in pre-Alpine garnet ( $Grt_1$ ) and is rimmed by rutile, if it communicates  
393 with the external matrix through fractures. In the matrix, rutile is rimmed by ilmenite.

394

#### 395 **5. Resulting P-T evolution**

396 The prograde-to-peak P-T evolution of the PU, SCU, BIU and RSU samples was constrained using the  
397 pseudosection approach and on the basis of the predicted stability fields of the observed mineral  
398 assemblages, combined with garnet, chloritoid and phengite compositional isopleths. The results of  
399 thermodynamic modelling show that the fractionation effects on the bulk-composition due to the growth of  
400 zoned garnet porphyroblasts are generally minor during the initial growth of garnet (*i.e.*, after the  
401 fractionation of garnet core). However, they become significant after the fractionation of both garnet core  
402 and mantle. The general topology of the calculated pseudosections for all samples is similar as far as the  
403 relationships between the main phases of interest is concerned, and is in line with previous studies related  
404 on phase equilibria modeling in the same system (*e.g.*, Guiraud *et al.*, 1990; Proyer, 2003; Wei & Powell,  
405 2004, 2006; Smye *et al.*, 2010; Manzotti *et al.*, 2015): (i) garnet is always stable over a large range of P-T  
406 conditions, whereas chlorite is limited to  $P < 18-25$  kbar; (ii) chloritoid is stable at  $T < 550-600^\circ C$ , and kyanite is  
407 instead stable at increasing temperature (see Smye *et al.*, 2010); (iii) paragonite, glaucophane and jadeite  
408 represent the Na-rich phases stable at lower, intermediate and higher pressure, respectively.

409 The Average PT approach of THERMOCALC was further applied to peak assemblages for the PU, SCU,  
410 RSU and DSU samples and to the late prograde assemblage for the BIU sample. In the following, the results  
411 of both approaches are summarized.

412

### 413 **5.1 Sample DM1485 (PU)**

414 The observed prograde and peak assemblage (Qz + Phe + Grt + Chl + Cld + Rt + Ilm) is not modeled in the P-T  
415 region of interest because chloritoid is always predicted to be stable with a Na-rich phase (either paragonite  
416 or glaucophane), which was not observed in the studied sample. However, the occurrence of large oligoclase  
417 porphyroblasts in the matrix statically overgrowing the main foliation suggests that one or more Na-rich  
418 phases (e.g. glaucophane, paragonite) was likely stable in the prograde and peak assemblages and it is not  
419 preserved. The glaucophane/paragonite-bearing assemblage (Qz + Phe + Grt + Chl + Cld + Gln/Pg + Rt + Ilm)  
420 is modeled in a wide range of P-T conditions (450-570°C, 10-25 kbar) (Fig. 8).

421 Prograde and peak P-T conditions are more tightly constrained by the intersection of compositional  
422 isopleths. Specifically: (i) early prograde P-T conditions are constrained at 480-495°C, 19-21 kbar using  
423 compositions of garnet core ( $Sps_5Prp_6Grs_8Alm_{80}$ ) and of its inclusions of chloritoid ( $X_{Mg}=0.11$ ) and phengite  
424 ( $Si=3.48$  a.p.f.u.) (Fig. 8a); (ii) late prograde P-T conditions are constrained at 490-505°C, 20-22 kbar using the  
425 compositions of garnet mantle ( $Sps_{2.5}Prp_8Grs_{7.5}Alm_{81}$ ) and of its inclusions of chloritoid ( $X_{Mg}=0.15$ ) and  
426 phengite ( $Si=3.44-3.45$  a.p.f.u.) (Fig. 8b); (iii) peak P-T conditions are estimated at 500-515°C, 20-23 kbar using  
427 the compositions of garnet rim ( $Sps_{0.5}Prp_{11}Grs_{11}Alm_{78}$ ), of its chloritoid inclusions ( $X_{Mg}=0.18$ ) and of matrix  
428 phengite ( $Si=3.38-3.51$  a.p.f.u.) (Fig. 8c).

429 The AvPT approach applied to four different sets of mineral compositions gives peak P-T conditions  
430 of  $496 \pm 7$  °C,  $19.0 \pm 0.7$  kbar (Table 2), consistent with the results of pseudosection modeling (Fig. 8c).

431

### 432 **5.2 Sample DM1667c (SCU)**

433 Although glaucophane was not observed in prograde and peak assemblages, the modeled pseudosections  
434 predict its stability over a large P-T interval. However, the predicted modal amount of glaucophane is so low  
435 (< 5 vol%) that its (former) occurrence could likely have been overlooked. Ignoring glaucophane, the observed  
436 early prograde (Qz + Phe + Grt<sub>C</sub> + Chl + Cld + Ep + Rt + Ilm) and late prograde (Qz + Phe + Grt<sub>M</sub> + Cld ± Chl ±  
437 Ep/Lws + Rt + Ilm) assemblages are modeled by large tri- and quadri-variant fields at 420-500°C, 12-17 kbar  
438 and 400-500°C, 14-25 kbar, respectively (Fig. 9). Garnet, chloritoid and phengite compositional isopleths  
439 allow to further constrain the prograde P-T conditions: (i) early prograde conditions are constrained at 460-  
440 470°C, 17-19 kbar using the compositions of garnet core ( $Sps_5Prp_{3.5}Grs_{26}Alm_{65}$ ) and its inclusions of phengite  
441 ( $Si=3.34-3.46$  a.p.f.u.) (Fig. 9a); (ii) late prograde P-T conditions are constrained at 480-490°C, 19-21 kbar  
442 using the compositions of garnet mantle ( $Sps_{2.5}Prp_5Grs_{24}Alm_{68}$ ) and of its inclusions of chloritoid ( $X_{Mg}=0.20$ )  
443 and phengite ( $Si=3.40-3.49$  a.p.f.u.) (Fig. 9b). Although garnet core includes epidote, its growth is predicted  
444 to occur within the lawsonite stability field, but close to the Ep-out boundary.

445 The observed peak assemblage (Qz + Phe + Grt<sub>R</sub> + Cld + Lws + Rt + Ilm) is modeled by a relatively small  
446 quadri-variant field at 450-520°, 22-27 kbar. The intersection of compositional isopleths for garnet rim  
447 ( $Sps_{0.8}Prp_{10}Grs_{18}Alm_{74}$ ) and its inclusions of chloritoid ( $X_{Mg}=0.20$ ) and phengite ( $Si=3.36-3.43$  a.p.f.u.) defines  
448 peak P-T conditions at 500-520°C, 21-24 kbar (Fig. 9c). The AvPT approach applied to four different sets of  
449 mineral compositions gives peak P-T conditions of  $512 \pm 8$  °C,  $21.9 \pm 0.9$  kbar (Table 2), consistent with the  
450 results of pseudosection modeling (Fig. 9c).

451

### 452 **5.3 Sample DM1281 (BIU)**

453 Garnet core and its inclusions define the early prograde assemblage (Qz + Phe + Grt<sub>C</sub> + Cld + Pg + Chl + Rt).  
454 Staurolite is not considered as part of this assemblage due to its supposed retrograde nature (see  
455 microstructural relationships presented in Section 4.3). This assemblage is modeled by a quadri-variant field  
456 at 450-570°C, 10-18 kbar. The best fit between observed and modeled garnet (Sps<sub>6.5</sub>Prp<sub>12</sub>Grs<sub>6</sub>Alm<sub>74</sub>),  
457 chloritoid (X<sub>Mg</sub>=0.25) and chlorite (X<sub>Mg</sub>=0.62) compositions constrains P-T conditions for the growth of garnet  
458 core at 520-540°C, 16-23 kbar (Fig. 10a), in the Qz + Phe + Grt + Cld + Pg ± Chl ± Gln + Rt fields. These P-T  
459 conditions are at significantly lower T and higher P than the predicted stability field of staurolite, further  
460 confirming that staurolite is not compatible with the early prograde assemblage (see Section 4.3).

461 The late prograde assemblage consists of garnet mantle and its inclusions (Qz/Coe + Phe + Grt<sub>M</sub> + Cld  
462 + Pg + Ky + Jd + Gln + Rt); once again staurolite is not considered as part of this assemblage. Pseudomorphs  
463 after coesite are hosted in the outermost mantle domain, at the transition between Grt<sub>M</sub> and Grt<sub>R</sub>, suggesting  
464 that garnet mantle already grew at UHP conditions. The coexistence of chloritoid + kyanite constrains the  
465 temperature to a very narrow range (540-560°C), whereas the coexistence of jadeite, glaucophane and  
466 paragonite in the same garnet domain limits the pressures to the interval 24-28 kbar, *i.e.*, close to the  
467 transition between paragonite-bearing and jadeite-bearing fields (Fig. 10b). The modeled garnet  
468 (Sps<sub>1.5</sub>Prp<sub>19</sub>Grs<sub>2</sub>Alm<sub>76</sub>) and chloritoid (X<sub>Mg</sub>=0.30) compositional isopleths intersect within these fields and  
469 tightly constrain the late prograde P-T conditions at 540-560°C, 25-30 kbar, *i.e.*, at the transition between the  
470 quartz and coesite stability fields (Fig. 10b). This is consistent with the observed occurrence of polycrystalline  
471 aggregates of quartz after coesite at the transition between garnet mantle and rim. The AvPT approach  
472 applied to four different sets of mineral compositions gives late prograde P-T conditions of 557 ± 5 °C, 27.4 ±  
473 0.4 kbar (Table 2), consistent with the pseudosection results (Fig. 10b).

474 The peak assemblage (Coe + Phe + Grt<sub>R</sub> + Ky + Jd + Rt) is modelled by a large penta-variant field at T  
475 > 530°C and P > 25 kbar. Although garnet (Sps<sub>1.7</sub>Prp<sub>26</sub>Grs<sub>3.5</sub>Alm<sub>68</sub>) compositional isopleths are far apart, their  
476 intersection with phengite (Si = 3.45-3.49 a.p.f.u.) isopleths allows constraining peak P-T conditions at 660-  
477 730°C and 38-43 kbar (Fig. 10c), consistent with the peak P-T conditions proposed in previous papers and  
478 based on other lithologies (*i.e.*, pyrope-bearing whiteschists, eclogites, marbles; see review in Ferrando *et al.*,  
479 2017). The AvPT approach applied on the peak assemblage did not converge to a result, because its  
480 variance is too high to define enough reactions.

481

#### 482 **5.4 Sample DM1504 (RSU)**

483 The observed prograde and peak assemblage (Qz + Phe + Grt + Cld + Gln + Jd + Lws? + Rt) is modelled by a  
484 large quadri-variant field at 450-540°C, 19-25 kbar. The modelled garnet, chloritoid and phengite  
485 compositional isopleths intersect within this field and constrain prograde and peak P-T conditions as follows:  
486 (i) early prograde conditions are constrained at 490-510°C, 20-23 kbar using the compositions of garnet core  
487 (Sps<sub>9</sub>Prp<sub>8.5</sub>Grs<sub>16</sub>Alm<sub>67</sub>), of its chloritoid inclusions (X<sub>Mg</sub>=0.20) and of phengite (Si=3.31-3.43 a.p.f.u.) (Fig. 11a);  
488 (ii) late prograde conditions are constrained at 500-520°C, 20-24 kbar using the compositions of garnet  
489 mantle (Sps<sub>6</sub>Prp<sub>9.5</sub>Grs<sub>20</sub>Alm<sub>64</sub>), of its chloritoid inclusions (X<sub>Mg</sub>=0.22) and of phengite (Si=3.31-3.43 a.p.f.u.)  
490 (Fig. 11b); (iii) peak conditions are estimated at 510-525°C, 20-23 kbar using the compositions of garnet rim  
491 (Sps<sub>4.5</sub>Prp<sub>9</sub>Grs<sub>18.5</sub>Alm<sub>68</sub>), its chloritoid inclusions (X<sub>Mg</sub>=0.24) and phengite (Si=3.31-3.43 a.p.f.u.) (Fig. 11c). The  
492 AvPT approach applied to four different sets of mineral compositions gives peak conditions of 495 ± 8 °C,  
493 20.3 ± 0.6 kbar (Table 2), consistent with pseudosection results (Fig. 11c).

494

#### 495 **5.5 Sample DM1565 (DSU)**

496 (Alpine) peak P-T conditions for this sample were estimated using the AvPT approach, applied to three  
497 different sets of mineral compositions. Although not observed in the sample, lawsonite was included in the  
498 peak assemblage, allowing to consider the reactions involving grossular, which are relevant because garnet

499 is relatively enriched in this component. This strategy is supported by the fact that other metapelites from  
500 the same unit show unambiguous evidence for the occurrence of lawsonite in the peak assemblage (Nosengo,  
501 2018). The AvPT results point to peak P-T conditions of  $452 \pm 8$  °C,  $17.2 \pm 0.4$  kbar (Table 2).

502

## 503 **6. Discussion**

504

### 505 **6.1 New constraints on the prograde evolution of the tectonic units in the southern DMM**

#### 506 *6.1.1 Prograde evolution of the HP units bounding the UHP BIU*

507 The prograde P-T evolution inferred for the four units bounding the UHP BIU is summarized below:

- 508 - The PU experienced a prograde evolution starting in the lawsonite-blueschist facies and reaching peak  
509 conditions in the eclogite-facies (500-515°C, 20-23 kbar; Fig. 12a). Peak-T conditions are similar to those  
510 estimated by Avigad *et al.* (2003) (*i.e.*, 530 °C) using multi-equilibrium thermobarometry applied on  
511 garnet-bearing metapelites from the same structural position. However, peak-P conditions are  
512 significantly higher than the 14-16 kbar estimated by the same authors (Fig. 12a).
- 513 - The P-T prograde path inferred for the SCU and RSU is remarkably similar to that constrained for the PU,  
514 with eclogite-facies peak P-T conditions at 500-520°C, 20-24 kbar (Fig. 12b, d). The estimated peak-P  
515 conditions are significantly higher than those (500-550°C, 15 kbar) constrained by Chopin *et al.* (1991)  
516 and Compagnoni & Rolfo (2003), whereas peak-T are in agreement with literature data (Fig. 12b, d).
- 517 - In contrast to the other units, the DSU did not experience eclogitic metamorphism. Estimated peak  
518 conditions (450-470 °C, 17-18 kbar) point to lawsonite-blueschist facies conditions (Fig. 12e); peak-T are  
519 similar to those reported by Chopin *et al.* (1991) (500°C, 10-12 kbar), but pressures are significantly higher  
520 (Fig. 12e).

521 Overall, our new data for the HP units bounding the UHP one substantially confirm peak-T already  
522 estimated more than 25 years ago, but point to a significant increase of peak-P estimates ( $\Delta P = 5-10$  kbar).  
523 This is the same trend already followed in the definition of peak P-T conditions for the UHP BIU, that were  
524 initially estimated to be at about 30 kbar (*e.g.*, Chopin *et al.*, 1991; Compagnoni *et al.*, 1995) and progressively  
525 increased (35 kbar: *e.g.*, Compagnoni & Rolfo, 2003) up to 40-43 kbar (*e.g.*, Hermann, 2003; Castelli *et al.*,  
526 2007; Groppo *et al.*, 2007a; Ferrando *et al.*, 2009, 2017), in parallel with the progressive improvement of  
527 thermodynamic modeling approaches that extended the limits of conventional thermobarometry.

528

#### 529 *6.1.2 A revised prograde P-T path for the UHP BIU*

530 Peak P-T conditions (730°C, 40-43 kbar) and retrograde evolution of the UHP BIU are now very well defined  
531 and were constrained in the last decades through detailed petrological studies on a great variety of  
532 lithologies, among them pyrope-bearing whiteschists (Schertl *et al.*, 1991; Hermann, 2003; Ferrando *et al.*,  
533 2009; Gauthiez-Putallaz *et al.*, 2016), eclogites (Nowlan *et al.*, 2000; Di Vincenzo *et al.*, 2006; Groppo *et al.*,  
534 2007a), marbles and calc-silicate rocks (Rubatto & Hermann, 2001; Ferraris *et al.*, 2005; Di Vincenzo *et al.*,  
535 2006; Castelli *et al.*, 2007). Garnet-bearing metapelites have never been used to constrain the BIU peak P-T  
536 conditions and have only been marginally used to constrain its retrograde evolution (Groppo *et al.*, 2006).  
537 This is due to the fact that the highly variant assemblage (*i.e.*, Coe + Phe + Grt + Ky + Jd) stable at UHP  
538 conditions is not suitable for application of conventional thermobarometry. Conversely, metapelites have  
539 been already used to constrain the early prograde evolution of the BIU, thanks to the preservation of  
540 abundant prograde inclusions in the core of porphyroblastic garnets. Chopin *et al.* (1991) and Michard *et al.*  
541 (1993) described a garnet-bearing phengitic micaschist (sample DM8412) very similar to our sample DM1281.  
542 Both their and our garnet porphyroblasts are, in turn, remarkably similar to the cores of the “superzoned”  
543 garnets described by Compagnoni & Hirajima (2001) (sample DM880). Chopin *et al.* (1991) and Compagnoni

544 & Hirajima (2001) interpreted the coexistence of chloritoid, kyanite, staurolite and chlorite in the  
545 polymineralic inclusions hosted within garnet cores as evidence that the BIU prograde trajectory passed close  
546 to the invariant point involving  $\text{Cld} + \text{Ky} + \text{St} + \text{Chl}$ , located around 600°C, 15 kbar. This was considered as a  
547 pinning point for the BIU prograde path for more than 25 years, resulting in a steep prograde trajectory  
548 located at temperatures significantly higher than the peak-T conditions estimated at that time for the  
549 adjacent units.

550 Our study unambiguously demonstrates that staurolite in the polymineralic inclusions hosted within  
551 garnet core and mantle has a retrograde nature, growing at the interface between garnet and kyanite, the  
552 latter mineral preserving a rounded/corroded shape (Fig. 4e). We suggest that staurolite grew during the  
553 retrograde evolution through a reaction that involved garnet, kyanite and chlorite as reactants. The aqueous  
554 fluid needed to trigger the reaction would not have been necessarily introduced from outside through  
555 fractures, but it could derive from the breakdown of chlorite associated with kyanite in the polymineralic  
556 inclusion (*i.e.*, internally-derived fluid). Reaction modelling by the least square method (freeware application  
557 available on demand; Godard, 2009) applied to the composition of garnet core/mantle, chlorite, kyanite and  
558 staurolite yielded balanced reactions of this type:  $\text{Chl} + \text{Ky} + \text{Grt} = \text{St}$  (details are given in Table SM8),  
559 accounting for the retrograde formation of staurolite in a closed system, *i.e.* the polymineralic inclusion. The  
560 above-mentioned reaction is predicted to occur in the KFMASH system at about 600-650 °C, 13-15 kbar  
561 (White *et al.*, 2014), and it would have been therefore intersected during the retrograde evolution of the BIU  
562 (Fig. 12c). It is worth noting that the growth of retrograde staurolite was already observed in the matrix of a  
563 garnet-bearing metapelite from the BIU, and was constrained exactly at these P-T conditions (Groppo *et al.*,  
564 2006).

565 The new interpretation of the nature of staurolite occurring in the polymineralic inclusions hosted in the  
566 BIU garnet porphyroblasts has important consequences for the definition of the BIU prograde P-T path. The  
567 results of thermodynamic modeling and AvPT tightly constrain the growth of garnet core at 520-540°C, 16-  
568 23 kbar, *i.e.*, at significantly lower T and higher P than previously estimated, and at P-T conditions close to  
569 the peak P-T conditions of the adjacent units. Moreover, the growth of garnet mantle is modeled at UHP  
570 conditions, consistent with the occurrence of pseudomorphs after coesite included in the mantle domain.  
571 The whole prograde evolution of the BIU is thus significantly different from that previously assumed; it does  
572 not follow a regularly steep P/T gradient, but it is rather characterized by: (i) an early prograde evolution  
573 along a moderately steep P/T gradient, similar to that followed by the adjacent HP units; (ii) an intermediate  
574 steep, almost isothermal, pressure increase, and (iii) a late prograde temperature increase along a  
575 moderately steep P/T gradient, still at increasing pressure.

576

## 577 **6.2 Implications for the geodynamic interpretation of the southern DMM**

578 An in-depth discussion of the geodynamic processes responsible for the architecture of the southern DMM  
579 is beyond the aim of this paper. However, the following conclusions are worth noting and could represent  
580 new constraints for future investigations:

581 (1) the PU experienced eclogite-facies metamorphism under peak P-T conditions very similar to those  
582 registered by the SCU and RSU (500-520°C, 20-24 kbar). Moreover, the PU, SCU and RSU units followed  
583 the same prograde path, along a medium T/P gradient of about 12°C kbar<sup>-1</sup>, suggesting similar burial  
584 mechanisms. The similarity of the peak P-T conditions experienced by the PU and SCU, combined with  
585 the fact that the PU sample was collected from an outcrop located very close to the contact with the BIU  
586 (Fig. 1), could potentially raise the doubt that the two samples actually belong to the same unit (*i.e.*, SCU).  
587 The contact between the PU and overlying units (either SCU or BIU) has been located thanks to the abrupt  
588 occurrence, moving downward in the DMM nappe stack, of abundant graphitic micaschists with quartzite  
589 intercalations (see Fig.1). These micaschists have never been described within the other units (either



590 SCU, BIU or RSU) and, in turn, have been considered diagnostic of the former PU (e.g., Vialon, 1966;  
591 Chopin *et al.*, 1991; Avigad *et al.*, 2003). Following this criterion, sample DM1485 has been attributed to  
592 the PU. Our results thus highlight that, in the investigated area, the PU does not correspond to a  
593 blueschist unit, as previously described (Avigad *et al.*, 2003), and therefore the actual occurrence of a  
594 blueschist unit stacked below an eclogitic ones has to be restricted to northernmost sectors of the DMM  
595 (*i.e.*, the Brianconnais-like tectonic window in the Pinerolo area; *e.g.*, Manzotti *et al.*, 2016).

596 (2) the UHP BIU seems to have followed an early prograde evolution similar to that of the other eclogitic  
597 units of the southern DMM tectonic “sandwich”. The attainment of UHP peak conditions occurred  
598 through an earlier almost isothermal increase in pressure ( $\Delta P=8-10$  kbar) along a significantly lower T/P  
599 gradient (ca.  $3^{\circ}\text{C kbar}^{-1}$ ) and a later increase in temperature ( $\Delta T=150-170$  °C) along a medium T/P gradient  
600 (ca.  $15^{\circ}\text{C kbar}^{-1}$ ). Our results suggest that UHP metamorphism was not the result of a single,  
601 homogeneous, process, but rather the product of a two-step process. Further geochronological studies  
602 are needed in order to test if the UHP BIU shared a synchronous prograde evolution with the adjacent  
603 eclogitic units.

604 (3) the DSU is the only unit of the southern DMM tectonic “sandwich” that, according to our results, did not  
605 experience eclogite-facies metamorphism. It is worth noting that, on the field, the DSU is separated from  
606 the eclogitic units by a hundreds of metres thick shear zone (tectonic *mélange sensu* Festa *et al.*, 2019),  
607 which includes slices of meta-ophiolite (Valmala Shear Zone: Nosenzo, 2018). The detailed description  
608 and interpretation of this shear zone is beyond the aim of this paper and further studies are necessary  
609 to understand its role in decoupling the southern DMM during subduction and/or in driving exhumation  
610 of related (U)HP units.

611

## 612 **Acknowledgements**

613 Roberto Compagnoni introduced most of us to the fascinating southern Dora-Maira Massif and to the beauty  
614 and challenges of metamorphic petrology. R. Compagnoni, R. Turello and T. Hirajima collected sample  
615 DM1281 studied in this paper. Two anonymous reviewers provided constructive comments which  
616 significantly improved the manuscript; the Guest Editor is warmly thanked for its several constructive  
617 remarks and its meticulous editorial handling. This research was funded by University of Torino, Ricerca  
618 Locale, ex-60% 2016, 2017 funds: FERS\_RILO\_17\_01 (SF), FESA\_RILO\_17\_01 (AF), GROC\_RILO\_17\_01 (CG),  
619 ROLF\_RILO\_16\_01 (FR), and by the Italian Ministry of University and Research, PRIN 2015: 2015EC9PJ5 (GB).

620

621 **References**

622

- 623 Avigad, D., Chopin, C., Le Bayon R. (2003): Thrusting and extension in the southern Dora-Maira ultra-high  
624 pressure massif (Western Alps): view from below the coesite-bearing unit. *J. Geol.*, **111**, 57–70.
- 625 Balestro, G., Cadoppi, P., Di Martino, L., Sacchi, R. (1995): Il settore meridionale del Massiccio Dora-Maira  
626 (Valli Maira e Varaita): inquadramento, carta geologica e guida a un'escursione. Rapporti Alpi-Appennino  
627 e guida alle escursioni. *Accademia Nazionale delle Scienze*, **14**, 501–529.
- 628 Balestro, G., Festa, A., Borghi, A., Castelli, D., Gattiglio, M., Tartarotti, P. (2018): Role of Late Jurassic intra-  
629 oceanic structural inheritance in the Alpine tectonic evolution of the Monviso meta-ophiolite Complex  
630 (Western Alps). *Geol. Magaz.*, **155** (2), 233–249.
- 631 Biino, G. & Compagnoni R. (1992): Very high pressure metamorphism of the Brossasco coronite metagranite,  
632 southern Dora-Maira Massif, Western Alps. *Schweiz. Mineral. Petrogr. Mitt.*, **72**, 347–363.
- 633 Botta, S. (2015): Studio geologico-petrografico dell'Unità di Rocca Solei, Massiccio Dora-Maira meridionale  
634 (Alpi Occidentali). Unpublished MSc Thesis, Univ. Torino, Italy, 245 pp.
- 635 Burov, E., Francois, T., Yamato, P., Wolf, S. (2014): Mechanisms of continental subduction and exhumation  
636 of HP and UHP rocks. *Gondw. Res.*, **25**, 464–493.
- 637 Butler, J.P., Beaumont, C., Jamieson, R.A. (2013): The Alps 1: a working geodynamic model for burial and  
638 exhumation of (ultra)high-pressure rocks in Alpine-type orogens. *Earth Planet. Sci. Lett.*, **377–378**, 114–  
639 131.
- 640 Castelli, D., Rolfo, F., Groppo, C., Compagnoni, R. (2007): Impure marbles from the UHP Brossasco-Isasca Unit  
641 (Dora-Maira Massif, Western Alps): evidence for Alpine equilibration in the diamond stability field and  
642 evaluation of the X(CO<sub>2</sub>) fluid evolution. *J. metamorphic Geol.*, **25**, 587–603.
- 643 Chemenda, A.I., Mattauer, M., Mattavieille, J., Bokun, A.N. (1995): A mechanism for syn-collisional rock  
644 exhumation and associated normal faulting: results from physical modelling. *Earth Planet. Sci. Lett.* **132**,  
645 225–232.
- 646 Chopin, C. (1984): Coesite and pure pyrope in high-grade blueschists of the Western Alps: a first record and  
647 some consequences. *Contrib. Mineral. Petrol.*, **86**, 107–118.
- 648 — (2003): Ultrahigh-pressure metamorphism: tracing continental crust into the mantle. *Earth Planet. Sci.*  
649 *Lett.*, **212**, 1–14.
- 650 Chopin, C., Henry, C. Michard, A. (1991): Geology and petrology of the coesite-bearing terrain, Dora Maira  
651 Massif, Western Alps. *Eur. J. Mineral.*, **3**, 263–291.
- 652 Compagnoni, R. & Hirajima, T. (2001): Superzoned garnets in the coesite-bearing Brossasco-Isasca Unit, Dora-  
653 Maira massif, western Alps, and the origin of the whiteschists. *Lithos*, **57**, 219–236.
- 654 Compagnoni, R. & Rolfo, F. (1999): Characteristics of UHP pelites, gneisses and other unusual rocks.  
655 *International Geology Review*, **41**, 552–570.
- 656 —, — (2003): Ultrahigh-pressure units in the Western Alps. *in*: “Ultrahigh-pressure metamorphism”, D.A.  
657 Carswell & R. Compagnoni, eds, *EMU Notes in Mineralogy*, **5**, 13–49.
- 658 Compagnoni, R., Hirajima, T., Chopin, C. (1995): Ultra-high pressure metamorphic rocks in the Western Alps.  
659 *in*: “Ultrahigh Pressure Metamorphism”, R.G. Coleman & X. Wang, eds., Cambridge University Press, 206–  
660 243.
- 661 Compagnoni, R., Rolfo, F., Groppo, C., Hirajima, T., Turello R. (2004): Mapping of Alpine rocks characterized  
662 by “HP” to “UHP” metamorphic overprint in the southern Dora-Maira Massif (Western Alps). *in*: “Mapping  
663 Geology in Italy”, G. Pasquare & C. Venturini, eds., APAT, Dipartimento Difesa del Suolo, Servizio Geologico  
664 d'Italia, Roma 2004 (2006), **Map 34**, 287–294, Printed by S.EL.CA., Firenze.
- 665 Compagnoni, R., Rolfo, F., Groppo, C., Hirajima, T., Turello R. (2012): Geologic map of the UHP Brossasco-  
666 Isasca Unit (Western Alps). *J. Maps*, **8/4**, 465–472.

- 667 Connolly (1990): Multivariable phase diagrams: an algorithm based on generalized thermodynamics. *Am. J.*  
668 *Sci.*, **290**, 666–718.
- 669 — (2005): Computation of phase equilibria by linear programming: A tool for geodynamic modeling and its  
670 application to subduction zone decarbonation. *Earth Planet. Sci. Lett.*, **236**, 524–541.
- 671 — (2009): The geodynamic equation of state: what and how. *Geochem. Geophys. Geosyst.*, **10**, Q10014.
- 672 Cossio, R., Borghi, A., Ruffini, R. (2002): Quantitative modal determination of geological samples based on X-  
673 ray multielemental map acquisition. *Microsc. Microanal.*, **8**, 139–149.
- 674 Di Vincenzo, G., Tonarini, S., Lombardo, B., Castelli, D., Ottolini, L. (2006): Comparison of <sup>40</sup>Ar–<sup>39</sup>Ar and Rb–Sr  
675 data on phengites from the UHP Brossasco-Isasca Unit (Dora Maira Massif, Italy): Implications for dating  
676 white mica. *J. Petrol.*, **47**, 1439–1465.
- 677 Ferrando, S., Frezzotti, M.L., Petrelli, M., Compagnoni, R. (2009): Metasomatism of continental crust during  
678 subduction: the UHP white schists from the southern Dora-Maira Massif (Italian Western Alps). *J.*  
679 *metamorphic Geol.*, **27**, 739–756.
- 680 Ferrando, S., Groppo, C., Frezzotti, M.L., Castelli, D., Proyer, A. (2017): Dissolving dolomite in a stable UHP  
681 mineral assemblage: evidence from Cal-Dol marbles of the Dora-Maira Massif (Italian Western Alps). *Am.*  
682 *Mineral.*, **102**, 42–60.
- 683 Ferraris, C., Castelli, D., Lombardo, B. (2005): SEM/TEM-AEM characterization of micro- and nano-scale  
684 zonation in phengite from a UHP Dora-Maira marble: Petrologic significance of armoured Si-rich domains.  
685 *Eur. J. Mineral.*, **17**, 453–464.
- 686 Festa, A., Pini, G.A., Ogata, K., Dilek, Y. (2019): Diagnostic features and field-criteria in recognition of tectonic,  
687 sedimentary and diapiric mélanges in orogenic belts and exhumed subduction-accretion complexes.  
688 *Gondw. Res.*, **online version**, <https://doi.org/10.1016/j.gr.2019.01.003>.
- 689 Ford, M., Duchéne, S., Gasquet, D., Vanderhaeghe, O. (2006): Two-phase orogenic convergence in the  
690 external and internal SW Alps. *J. Geol. Soc.*, **163**, 815–826.
- 691 Fuhrman, M.L. & Lindsley, D.H. (1988): Ternary-Feldspar Modeling and Thermometry. *Am. Mineral.*, **73**, 201–  
692 215.
- 693 Gauthiez-Putallaz, L., Rubatto, D., Hermann, J. (2016): Dating prograde fluid pulses during subduction by in  
694 situ U–Pb and oxygen isotope analysis. *Contrib. Mineral. Petrol.*, **171**, article 15, 20 pp.
- 695 Gerya, T. (2015): Tectonic overpressure and underpressure in lithospheric tectonics and metamorphism. *J.*  
696 *metamorphic Geol.*, **33**, 785–800.
- 697 Gerya, T. & Stöckhert, B. (2006): Two-dimensional numerical modeling of tectonic and metamorphic histories  
698 at active continental margins. *Int. J. Earth Sci. (Geol. Rundsch.)*, **95**, 250–274.
- 699 Godard, G. (2009): Two orogenic cycles in eclogite-facies gneisses of the Southern Armorican Massif (France).  
700 *Eur. J. Mineral.*, **21**, 1173–1190.
- 701 Green, E.C.R., Holland, T.J.B., Powell, R. (2007): An order–disorder model for omphacitic pyroxenes in the  
702 system jadeite–diopside–hedenbergite–acmite, with applications to eclogite rocks. *Am. Mineral.*, **92**,  
703 1181–1189.
- 704 Green, E.C.R., White, R.W., Diener, J.F.A., Powell, R., Holland, T.J.B., Palin, R.M. (2016): Activity–composition  
705 relations for the calculation of partial melting equilibria in metabasic rocks. *J. metamorphic Geol.*, **34**, 845–  
706 869.
- 707 Groppo, C. (2002): Studio geologico-petrografico della terminazione nord-occidentale dell’Unita Brossasco-  
708 Isasca in facies eclogitica a coesite, Massiccio Dora-Maira (Alpi Occidentali). Unpublished M.Sc. Thesis,  
709 Univ. Torino, Italy, 175 pp.
- 710 Groppo, C., Castelli, D., Compagnoni, R. (2006): Late chloritoid-staurolite assemblage in a garnet-kyanite  
711 bearing metapelite from the UHP Brossasco-Isasca Unit (Dora-Maira Massif, Western Alps): new  
712 petrological constraints for a portion of the P-T decompressional path. *in*: “Ultrahigh-pressure

713 metamorphism: Deep continental subduction”, B.H. Hacker, W.C. McClelland & J.G. Liou J.G., eds., GSA  
714 Special Paper, **403**, 127–138.

715 Groppo, C., Castelli, D., Rolfo, F. (2007b): HT, Pre-Alpine relics in a spinel-bearing dolomite marble from the  
716 UHP Brossasco-Isasca Unit (Dora-Maira Massif, western Alps). *Per. Mineral.*, **76**, 155–168.

717 Groppo, C., Lombardo, B., Castelli, D., Compagnoni, R. (2007a): Exhumation history of the UHPM Brossasco-  
718 Isasca Unit, Dora-Maira Massif, as inferred from a phengite-amphibole eclogite. *Int. Geol. Rev.*, **49**, 142–  
719 168.

720 Guiraud, M., Holland, T.J.B., Powell R. (1990): Calculated mineral equilibria in the greenschist-blueschist-  
721 eclogite facies in Na<sub>2</sub>O-FeO-MgO-Al<sub>2</sub>O<sub>3</sub>-SiO<sub>2</sub>-H<sub>2</sub>O: methods, results and geological applications. *Contrib.*  
722 *Mineral. Petrol.*, **104**, 85–98.

723 Henry, C. (1990): L’unité à coesite du massif Dora-Maira dans son cadre pétrologique et structurale (Alpes  
724 Occidentales, Italie). Thèse Doctorat., Université Paris 6, 149 pp.

725 Henry, C., Michard, A., Chopin, C. (1993) : Geometry and structural evolution of ultra-high pressure and high  
726 pressure rocks from the Dora-Maira massif, western Alps, Italy. *J. Struct. Geol.*, **15**, 965–981.

727 Hermann, J. (2003): Experimental evidence for diamond-facies metamorphism in the Dora-Maira massif.  
728 *Lithos*, **70**, 163–182.

729 Holland, T.J.B. & Powell, R. (1998): An internally consistent thermodynamic dataset for phases of petrological  
730 interest. *J. metamorphic Geol.*, **16**, 309–343.

731 —, — (2011): An improved and extended internally consistent thermodynamic dataset for phases of  
732 petrological interest, involving a new equation of state for solids. *J. metamorphic Geol.*, **29**, 333–383.

733 Lardeaux, J., Schwartz, S., Tricart, P., Paul, A., Guillot, S., Béthoux, N., Masson, F. (2006): A crustal-scale cross-  
734 section of the south-western Alps combining geophysical and geological imagery. *Terra Nova*, **18** (6), 412–  
735 422.

736 Li, Z., Gerya, T.V., Burg, J.P. (2010). Influence of tectonic overpressure on P-T paths of HP–UHP rocks in  
737 continental collision zones: thermomechanical modelling. *J. metamorphic Geol.*, **28**, 227–247.

738 Liou, J.G. & Zhang, R.Y. (2002): Ultrahigh-pressure metamorphic rocks. Ency Phys Sci Tech (Third Edition). 17,  
739 Academia Press, 227–244.

740 Manzotti, P., Pitra, P., Langlade, J., Ballèvre, M. (2015): Constraining P-T conditions during thrusting of a  
741 higher pressure unit over a lower pressure one (Gran Paradiso, Western Alps). *J. metamorphic Geol.*, **33**,  
742 981–1002.

743 Manzotti, P., Ballèvre, M., Poujol, M. (2016): Detrital zircon geochronology in the Dora Maira and Zone  
744 Houillère: A record of sediment travel paths in the Carboniferous. *Terra Nova*, **28**, 279–288.

745 Matsumoto, N. & Hirajima, T. (2000): Garnet in pelitic schists from a quartz-eclogite unit of the southern  
746 Dora-Maira massif, Western Alps. *Schweiz. Mineral. Petrol. Mitt.*, **80**, 53–62.

747 Manzotti, P., Bosse, V., Pitra, P., Robyr, M., Schiavi, F., Ballèvre, M. (2018): Exhumation rates in the Gran  
748 Paradiso (Western Alps) constrained by in situ U-Th-Pb dating of accessory phases (monazite, allanite and  
749 xenotime). *Contrib. Mineral. Petrol.*, **173**, 24.

750 Michard, A., Chopin, C., Henry, C. (1993): Compression versus extension in the exhumation of the Dora-Maira  
751 coesite-bearing unit, Western Alps. *Tectonophysics*, **221**, 173–193.

752 Michard, A., Henry, C., Chopin, C. (1995): Structures in UHPM rocks: a case study from the Alps. in: “Ultrahigh  
753 Pressure Metamorphism”, R.G. Coleman & X. Wang, eds., Cambridge University Press, 132-158.

754 Michard, A., Goffe, B., Chopin, C., Henry, C. (1996): Did the Western Alps develop through an Oman-type  
755 stage? The geotectonic setting of high-pressure metamorphism in two contrasting Tethyan transects. *Ecl.*  
756 *Geol. Helv.*, **89**, 43– 80.

757 Nosenzo (2018): Studio geologico-strutturale e metamorfico del massiccio Dora-Maira meridionale in  
758 Valmala (Valle Varaita, Alpi Occidentali). Unpublished M.Sc. Thesis, Univ. Torino, Italy, 187 pp.

- 759 Nowlan, E.U., Schertl, H.P., Schreyer, W. (2000): Garnet–omphacite–phengite thermobarometry of eclogites  
760 from the coesite-bearing unit of the southern Dora-Maira Massif, Western Alps. *Lithos*, **52**, 197–214.
- 761 Pouchou, J.L. & Pichoir, F. (1988): Determination of mass absorption coefficients for soft X-rays by use of the  
762 electron microprobe. Microbeam Analysis. San Francisco Press, San Francisco, 319–324 p.
- 763 Powell, R. & Holland, T.J.B. (1994): Optimal geothermometry and geobarometry. *Am. Mineral.*, **79**, 120–133.
- 764 Proyer, A. (2003): Metamorphism of pelites in NKFMAH - a new petrogenetic grid with implications for the  
765 preservation of high pressure mineral assemblages during exhumation. *J. metamorphic Geol.*, **21**, 493–  
766 509.
- 767 Reuber, G., Kaus, B.J.P., Schmalholz, S.M., White, R.W. (2016): Nonlithostatic pressure during subduction and  
768 collision and the formation of (ultra)high-pressure rocks. *Geology*, **44**, 343–346.
- 769 Rubatto, D. & Hermann, J. (2001): Exhumation as fast as subduction? *Geology*, **29**, 3–6.
- 770 Sandrone R., Cadoppi P., Sacchi R., Vialon P. (1993): The Dora-Maira Massif. in: “Pre-Mesozoic Geology in the  
771 Alps”, J.F. von Raumer & F. Neubauer, eds., Springer-Verlag, 317–325.
- 772 Schenker, F.L., Schmalholz, S.M., Moulas, E., Pleuger, J., Baumgartner, L.P., Podladchikov, Y., Vrijmoed, J.,  
773 Buchs, N., Müntener O. (2015): Current challenges for explaining (ultra)high-pressure tectonism in the  
774 Pennine domain of the Central and Western Alps. *J. metamorphic Geol.*, **33**, 869–886.
- 775 Schertl, H.P. & O’Brien, P.J. (2013): Continental Crust at Mantle Depths: Key Minerals and Microstructures.  
776 *Elements*, **9**, 261–266.
- 777 Schertl, H.P., Schreyer, W., Chopin, C. (1991): The pyrope-coesite rocks and their country rocks at Parigi, Dora  
778 Maira Massif, Western Alps: detailed petrography, mineral chemistry and P-T path. *Contrib. Mineral.  
779 Petrol.*, **108**, 1–21.
- 780 Schmalholz, S.M. & Duretz, T. (2015): Shear zone and nappe formation by thermal softening, related stress  
781 and temperature evolution, and application to the Alps *J. metamorphic Geol.*, **33**, 887–908.
- 782 Schmalholz, S.M., Duretz, T., Schenker, F.L., Podladchikov, Y.Y. (2014): Kinematics and dynamics of tectonic  
783 nappes: 2-D numerical modelling and implications for high and ultrahigh pressure tectonism in the  
784 Western Alps. *Tectonophysics*, **631**, 160–175.
- 785 Sharp, Z.D., Essene, E.J., Hunziker, J.C. (1993): Stable isotope geochemistry and phase equilibria of coesite-  
786 bearing whiteschists, Dora Maira Massif, western Alps. *Contrib. Mineral. Petrol.*, **114**, 1–12.
- 787 Smith, D.C. (1984): Coesite in clinopyroxene in the Caledonides and its implications for geodynamics. *Nature*,  
788 **310**, 641–644.
- 789 Smye, A.J., Greenwood, L.V., Holland, T.J.B. (2010): Garnet–chloritoid–kyanite assemblages: eclogite facies  
790 indicators of subduction constraints in orogenic belts. *J. metamorphic Geol.*, **28**, 753–768.
- 791 Solarino, S., Malusà, M.G., Eva, E., Guillot, S., Paul, A., Schwartz, S., Zhao, L., Aubert, C., Dumont, T., Pondrelli,  
792 S., Salimbeni, S., Wang, Q., Xu, X., Zheng, T., Zhu, R. (2018): Mantle wedge exhumation beneath the Dora-  
793 Maira (U)HP dome unravelled by local earthquake tomography (Western Alps). *Lithos*, **296–299**, 623–636.
- 794 Stöckhert, B. & Gerya, T.V. (2005): Pre-collisional high pressure metamorphism and nappe tectonics at active  
795 continental margins: a numerical simulation. *Terra Nova*, **17**, 102–110.
- 796 Turello, R. (1993): Studio geologico e petrografico dell’area tra Martiniana (Valle Po) e Brossasco (Valle  
797 Varaita) - Massiccio Dora-Maira meridionale. Unpublished M.Sc. Thesis, Univ. Torino, Italy, 238 pp.
- 798 Vialon, P. (1966): Etude géologique du Massif Cristallin Dora-Maira, Alpes Cottiennes internes, Italie. PhD  
799 Tesis, Univ. Grenoble, Travaux du Lab. Géol. Fac. Sci. Grenoble, Memoir 4, 193 pp
- 800 Wei, C.J. & Powell, R. (2004): Calculated phase relations in high-pressure metapelites in the system NKFMAH  
801 (Na<sub>2</sub>O-K<sub>2</sub>O-FeO-MgO-Al<sub>2</sub>O<sub>3</sub>-SiO<sub>2</sub>-H<sub>2</sub>O). *J. Petrol.*, **45**, 183–202.
- 802 —, — (2006): Calculated phase relations in the system NCKFMASH (Na<sub>2</sub>O-CaO-K<sub>2</sub>O-FeO-MgO-Al<sub>2</sub>O<sub>3</sub>-SiO<sub>2</sub>-H<sub>2</sub>O)  
803 for high-pressure metapelites. *J. Petrol.*, **47**, 385–408.

804 White, R.W., Powell, R., Holland, T.J.B., Johnson, T.E., Green, E.C.R. (2014): New mineral activity–composition  
805 relations for thermodynamic calculations in metapelitic systems. *J. metamorphic Geol.*, **32**, 261–286.  
806 Whitney, D.L. & Evans, B.W. (2010): Abbreviations for names of rock-forming minerals. *Am. Mineral.*, **95**,  
807 185–187.  
808 Yamato, P., Burov, E., Agard, P., Le Pourhiet, L., Jolivet, L. (2008): HP-UHP exhumation during slow continental  
809 subduction: self-consistent thermodynamically and thermomechanically coupled model with application  
810 to the Western Alps. *Earth Planet. Sci. Lett.*, **271**, 63–74.  
811

812 **Figure captions**

813 **Fig. 1** – Simplified geological map (a) of the southern Dora-Maira Massif around the UHP Brossasco-Isasca  
814 Unit (modified from Compagnoni *et al.*, 2012, and with unpublished data from Botta, 2015, and Nosenzo,  
815 2018). Sample locations are shown by black stars both in the map and cross sections. The Polymetamorphic  
816 and Monometamorphic Complexes in the SCU, BIU, RSU and DSU refer to a Variscan amphibolite-facies  
817 metamorphic basement and to Permian igneous bodies, respectively, each of which reworked during Alpine  
818 metamorphism. The insets (b, c) show the location of the southern DMM in north-west Italy (b) and within a  
819 simplified tectonic sketch-map of the Western Alps (c).

820

821 **Fig. 2** – Processed micro-XRF maps of the studied metapelites. For sample DM1565 (DSU), Grt<sub>c</sub> and Grt<sub>M</sub> refer  
822 to pre-Alpine Grt<sub>1</sub> porphyroblasts, whereas Alpine Grt<sub>2</sub> idioblasts in the matrix are reported as Grt<sub>R</sub>. Dark-  
823 grey to black domains are holes in the thin sections (*i.e.*, pixels not assigned to mineral phases).

824

825 **Fig. 3** – Representative microstructures of samples DM1485 (a, b) and DM1667c (c-e) from the PU and SCU,  
826 respectively. Sample DM1485: (a) Garnet porphyroblast with a snow-ball structure including quartz and  
827 chloritoid. The plagioclase porphyroblasts in the matrix are related to retrogression. (b) Detail of chloritoid +  
828 phengite + paragonite polymineralic inclusion in garnet mantle. Sample DM1667c: (c) Detail of chloritoid  
829 included in garnet mantle, partially replaced by white mica. (d) Fine-grained epidote included in garnet  
830 mantle. (e) Box-shaped pseudomorph after lawsonite included in garnet rim, consisting of epidote + phengite  
831 + paragonite + chlorite. (a, b, c: Plane Polarized Light, PPL; d, e and insets in a, b; Crossed Polarized Light,  
832 XPL).

833

834 **Fig. 4** – Representative microstructures of sample DM1281 from the BIU. (a) Zoned garnet porphyroblast,  
835 with a large core and mantle crowded with fine-grained inclusions, and a thin rim with few inclusions. The  
836 main foliation is defined by phengite. The inset shows a pseudomorph after coesite, consisting of  
837 polycrystalline quartz, included in garnet mantle. (b) Detail of a pluri-mm kyanite porphyroblast (Ky<sub>1</sub>)  
838 enveloped by the main foliation. Small idioblasts of Ky<sub>2</sub> are in equilibrium with the S<sub>m</sub>. (c) Pseudomorph after  
839 jadeite, consisting of a fine-grained aggregate of albite, pyrophyllite and paragonite. (d) Fine-grained  
840 polymineralic inclusions in garnet mantle. The inset shows a polymineralic inclusion in garnet core: note the  
841 equilibrium relations among chloritoid, chlorite and paragonite. (e) Details of polymineralic inclusions in  
842 garnet mantle, consisting of kyanite, staurolite, paragonite and chlorite. Staurolite systematically separates  
843 corroded/rounded kyanite grains from garnet, suggesting that its growth is related to a reaction between  
844 garnet and kyanite. (f, g) Pseudomorphs after glaucophane (f) and jadeite (g) included in garnet mantle,  
845 consisting of fine-grained aggregates of paragonite + muscovite ± biotite and albite + pyrophyllite +  
846 paragonite, respectively. (a, b, c, f, g: XPL; c, d: PPL; e and inset in d: Back Scattered Electron image, BSE).

847

848 **Fig. 5** – Representative microstructures of samples DM1504 (a-c) and DM1565 (d-f) from the RSU and DSU,  
849 respectively. Sample DM1504: (a) Garnet porphyroblast with quartz and chloritoid inclusions, partially  
850 enveloped by the main foliation, defined by phengite and chloritoid. (b) Detail of the chloritoid inclusions in  
851 garnet core and mantle. The inset shows a very fine-grained polymineralic inclusion in garnet mantle,  
852 consisting of glaucophane and jadeite, partially replaced by albite, pyrophyllite and paragonite. (c) Tabular-  
853 shaped inclusion in garnet mantle, consisting of an aggregate of epidote + paragonite + quartz, possibly  
854 deriving from former lawsonite. Sample DM1565: (d) Large pre-Alpine garnet porphyroblasts (Grt<sub>1</sub>)  
855 enveloped by the main foliation. (e) Top: small Alpine garnet idioblasts (Grt<sub>2</sub>) in equilibrium with the main  
856 foliation defined by phengite; bottom: Grt<sub>2</sub> forming a discontinuous rim around Grt<sub>1</sub>. (f) Large aggregate of

857 fine-grained chloritoid enveloped by the  $S_m$  and interpreted as a pseudomorph after pre-Alpine staurolite.  
858 (a, b, c, d, e: PPL; f and insets in a, d: XPL; inset in b: BSE).

859

860 **Fig. 6** – Garnet compositions plotted in the Prp-Alm-(Grs+Sps) diagram. The zoning trend for each sample is  
861 highlighted by the arrow. Samples are grouped according to their bulk-composition (*i.e.*, Ca-poor vs. Ca-rich  
862 metapelites). For sample DM1565, only compositions of Alpine Grt<sub>2</sub> are plotted.

863

864 **Fig. 7** – Potassic white mica compositions plotted in the Si vs. Fe<sup>2+</sup> + Mg (a.p.f.u.) diagram. Compositions of  
865 micas defining the  $S_m$  are distinguished from those included in garnet and from the late flakes overgrowing  
866 the  $S_m$ . Samples are grouped according to their bulk-composition (*i.e.*, oxidized vs. not oxidized). The dashed  
867 line represents the ideal celadonic substitution. Note that point analyses for samples DM1485 (PU),  
868 DM1667c (SCU) and DM1504 (RSU) plot slightly above the line of ideal celadonite substitution, thus  
869 suggesting that these white micas contain some Fe<sup>3+</sup>.

870

871 **Fig. 8** – P-T pseudosections modeled for sample DM1485 (PU) using the measured bulk-composition (a), and  
872 the effective bulk-compositions after fractionation of garnet core (b) and of garnet core + mantle (c). Dotted  
873 lines are Rt and Ilm -in/out curves; dashed line is the Qz/Coe transition. The black ellipses show the P-T  
874 conditions constrained for the growth of garnet core (a), mantle (b) and rim (c), based on the intersection of  
875 compositional isopleths, as indicated in each legend. Dark grey squares with dotted ellipses in (c) represent  
876 peak P-T conditions (with 1 $\sigma$  error) as defined by AvPT applied on four different sets of mineral compositions  
877 (see Table 2).

878

879 **Fig. 9** – P-T pseudosections modeled for sample DM1667c (SCU). (a), (b), (c) and all the symbols as in Fig. 8.

880

881 **Fig. 10** – P-T pseudosections modeled for sample DM1281 (BIU). (a), (b), (c) and all the symbols as in Fig. 8;  
882 the inset in (b) clarifies the mineral assemblages stable in the narrow fields modelled in the central part of  
883 the pseudosection. Note that the scale is different from that in Fig. 8, 9 and 11, that pseudosection in (c) has  
884 been calculated at  $a_{H_2O}=0.4$ , and that AvPT data in (b) refer to late prograde P-T conditions.

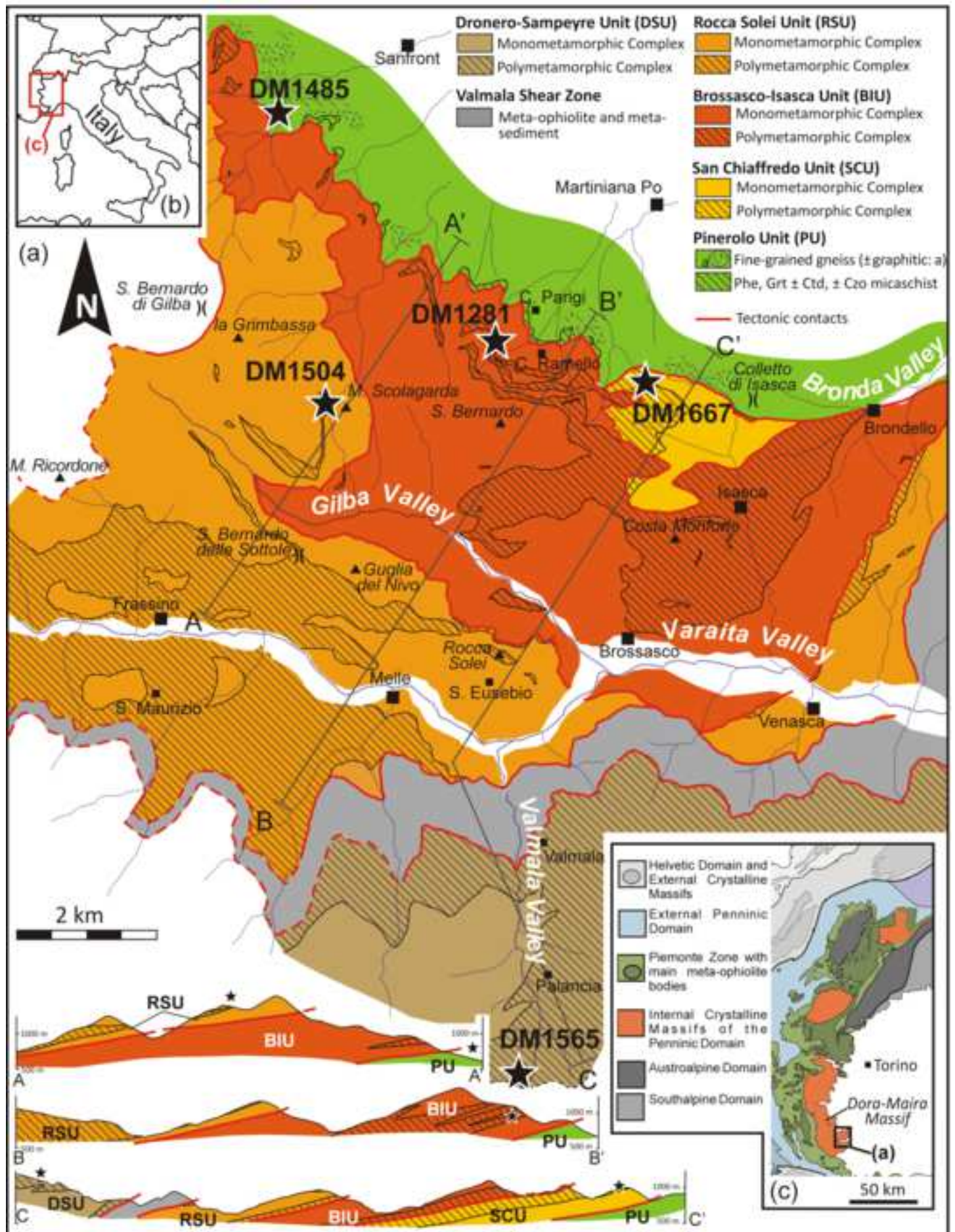
885

886 **Fig. 11** – P-T pseudosections modeled for sample DM1504 (RSU). (a), (b), (c) and all the symbols as in Fig. 8.

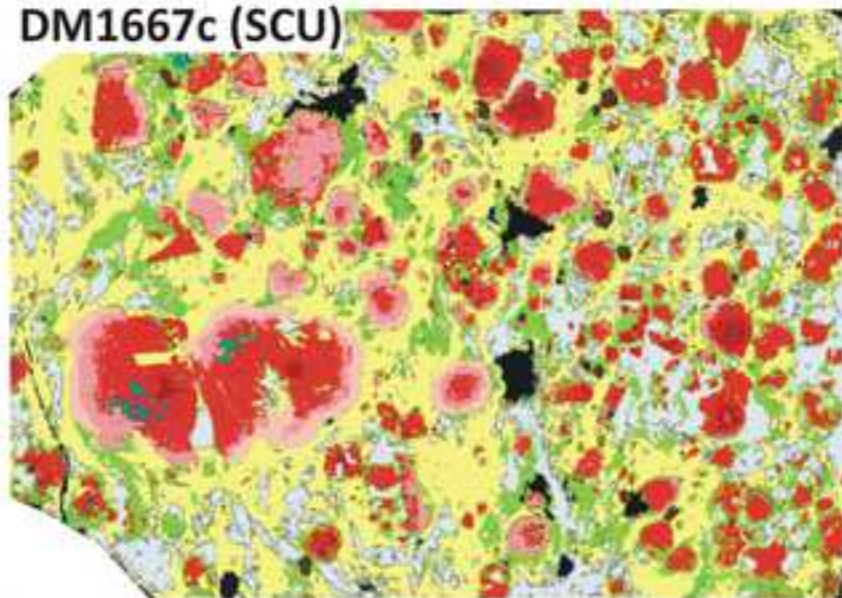
887

888 **Fig. 12** – (a-e) P-T grids showing the prograde trajectories for the Pinerolo Unit (a), San Chiaffredo Unit (b),  
889 Brossasco-Isasca Unit (c), Rocca Solei Unit (d) and Dronero-Sampeyre Unit (e) as inferred in this study,  
890 compared to peak P-T conditions derived from the literature (PU: Avigad *et al.*, 2003; SCU: Compagnoni &  
891 Rolfo, 2003; BIU: Ferrando *et al.*, 2017 and references therein; RSU: Chopin *et al.*, 1991; Matsumoto &  
892 Hirajima, 2000; DSU: Chopin *et al.*, 1991). For the BIU, the prograde and retrograde P-T path inferred from  
893 the literature is also reported. KFMASH reactions relevant for the discussion are reported in (c) (from White  
894 *et al.*, 2014). Note that the BIU retrograde trajectory crosses the Grt + Ky + Chl = St reaction (see Section 6.1.2  
895 for further discussion). (f) Comparison of the prograde P-T trajectories inferred for all the studied units: note  
896 that the early prograde path of the BIU is similar to the P-T trajectory of the other units. Metamorphic facies  
897 are from Liou & Zhang, 2002. The chloritoid stability field, as derived from pseudosections of Fig. 8-11, is  
898 reported in greenish-blue.

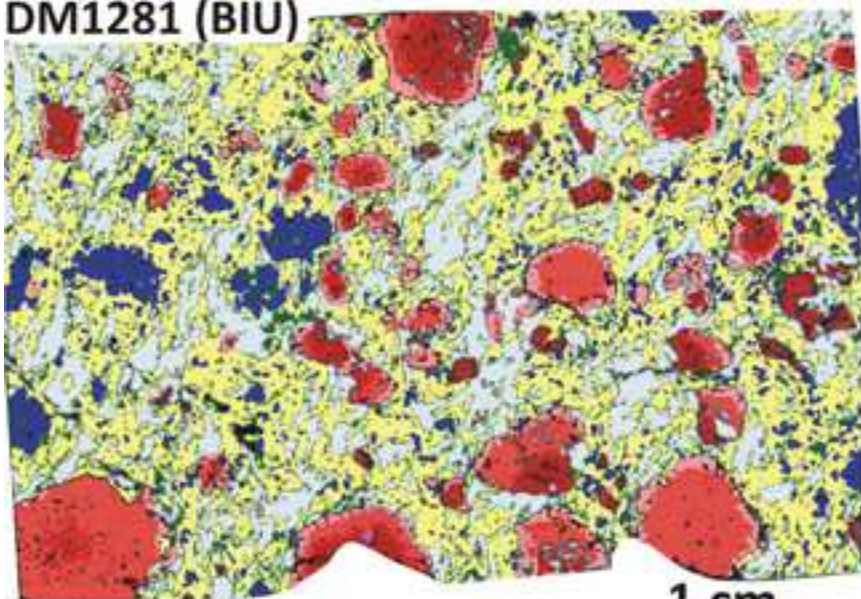




DM1667c (SCU)

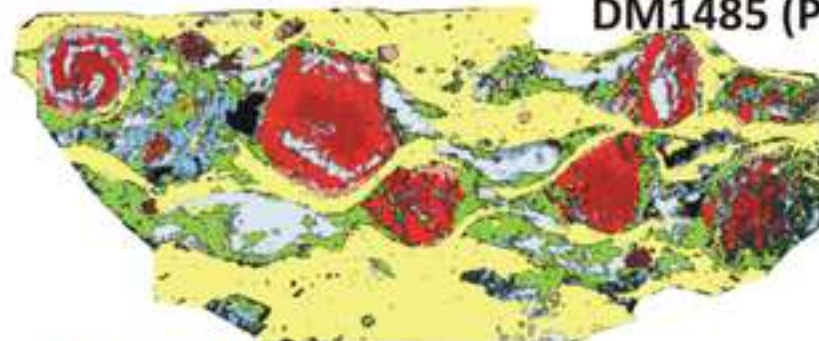


DM1281 (BIU)

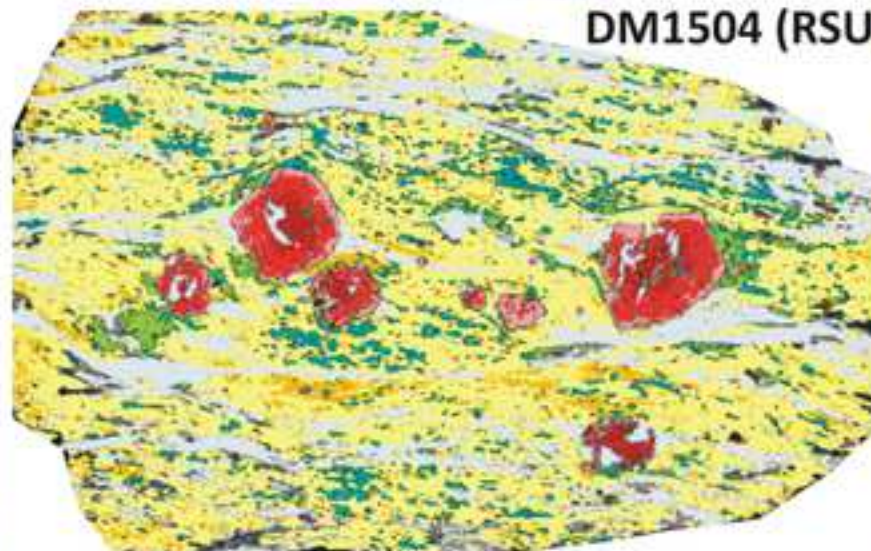


1 cm

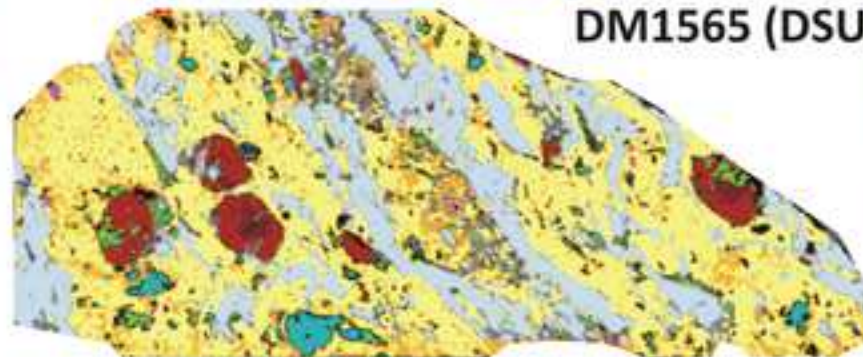
DM1485 (PU)



DM1504 (RSU)



DM1565 (DSU)



Qz

GrtC

GrtM

GrtR

Wm

Cld

Ky

Pg

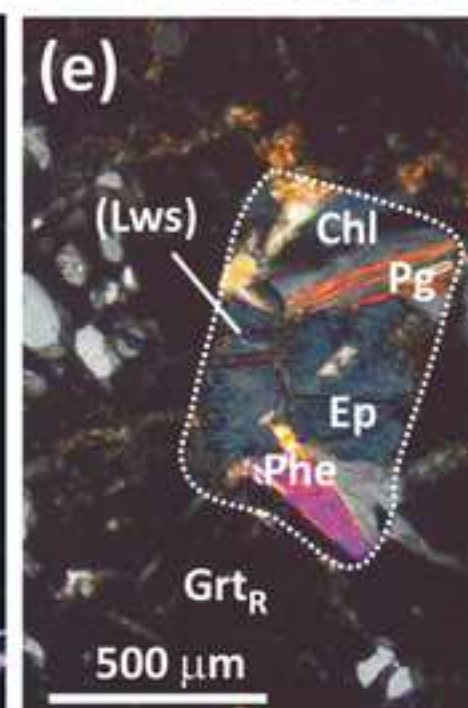
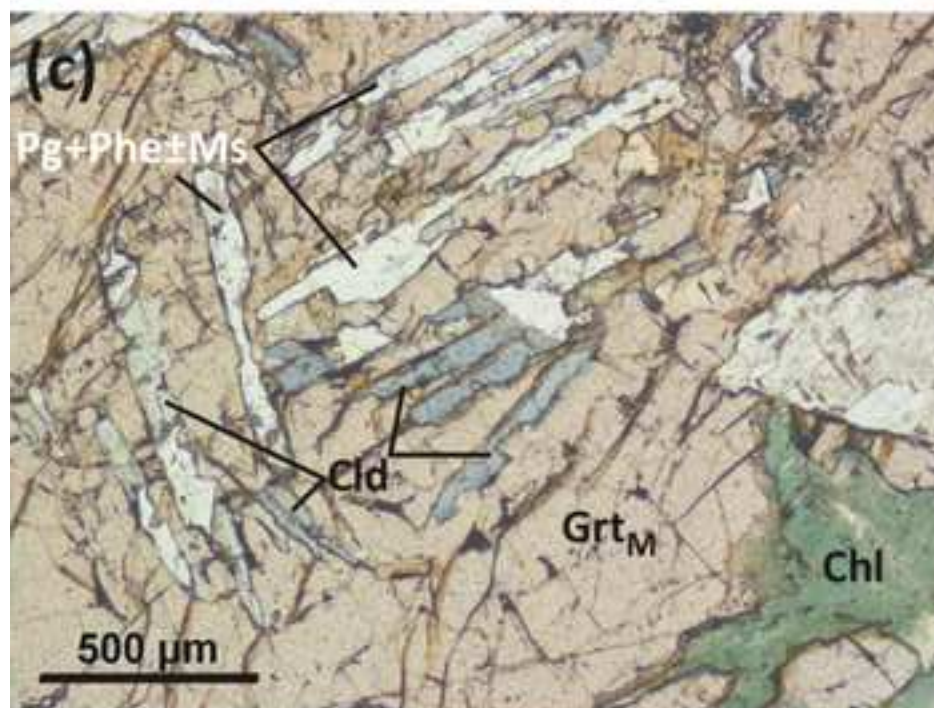
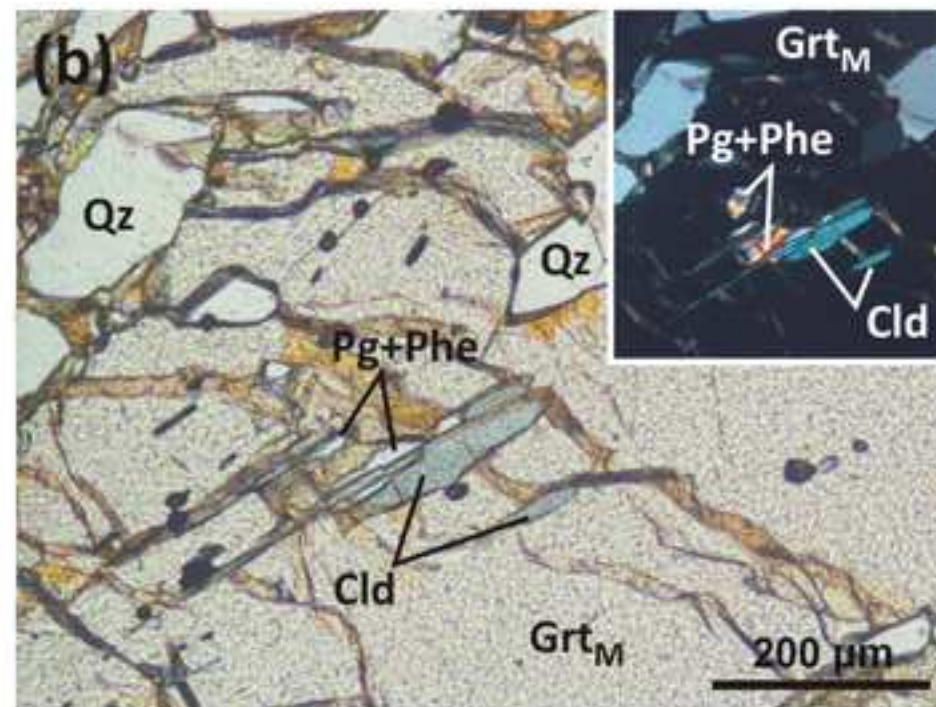
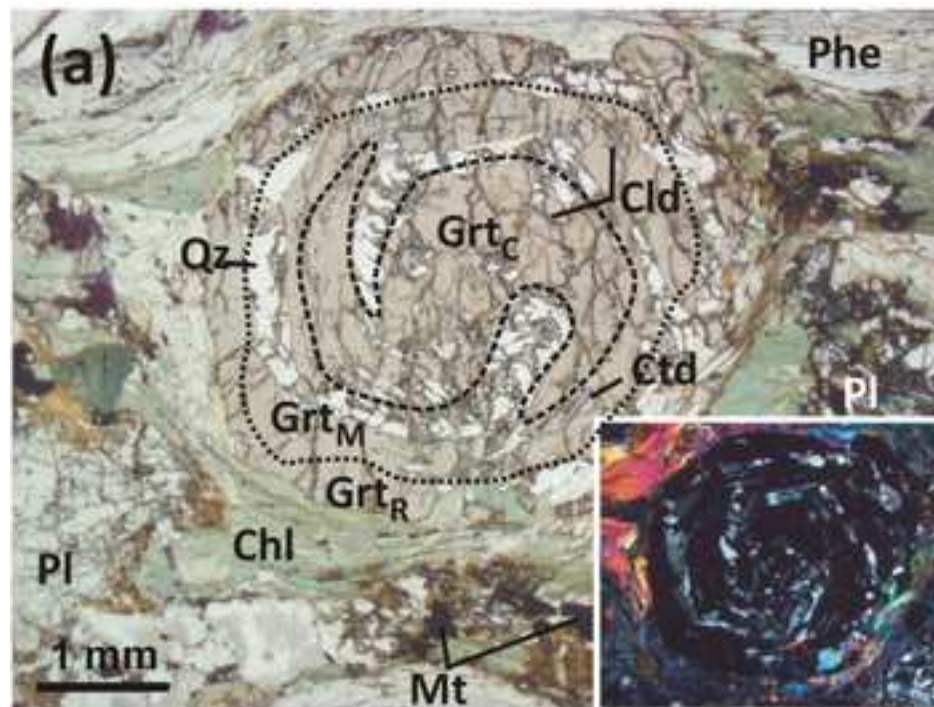
(Jd)

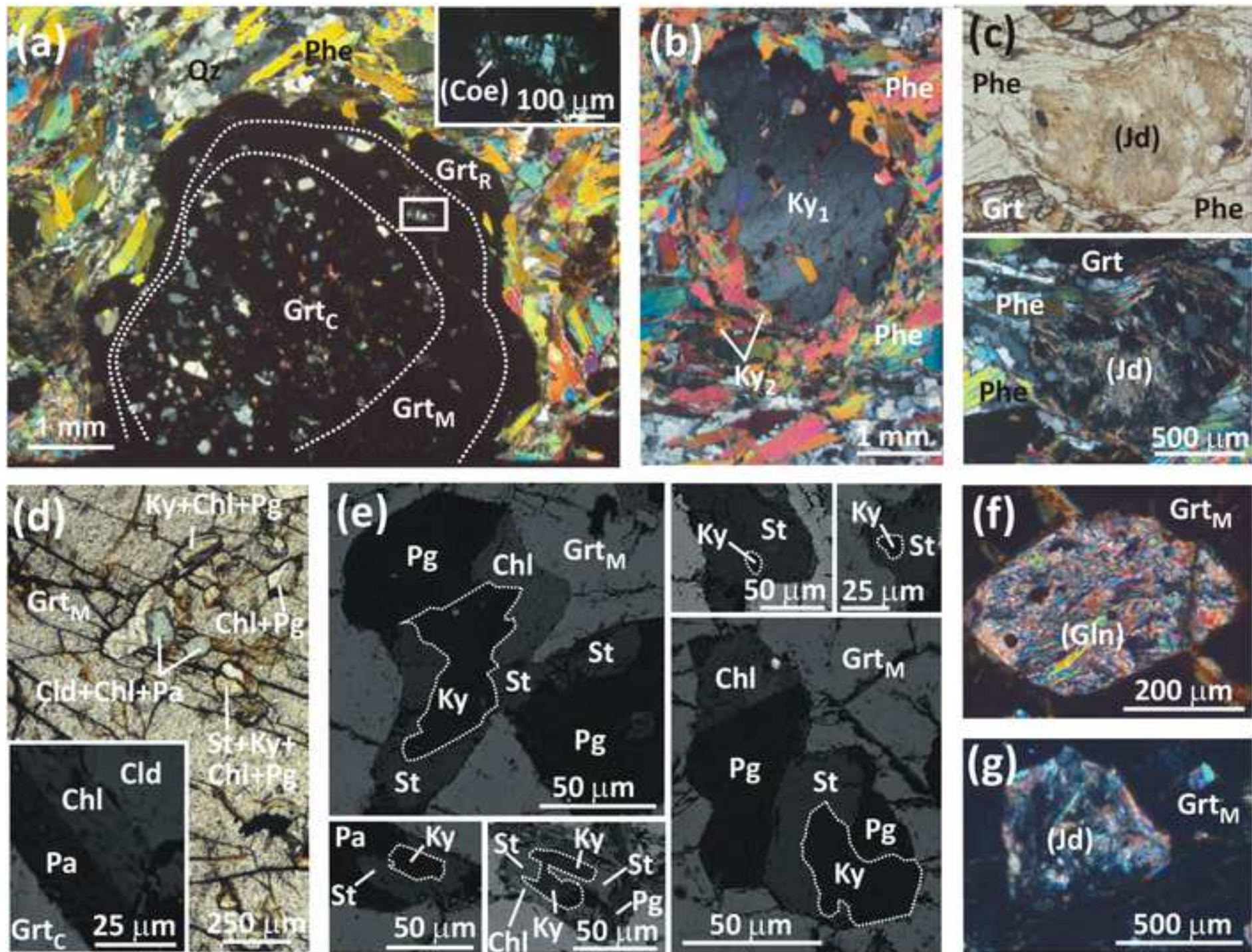
Chl

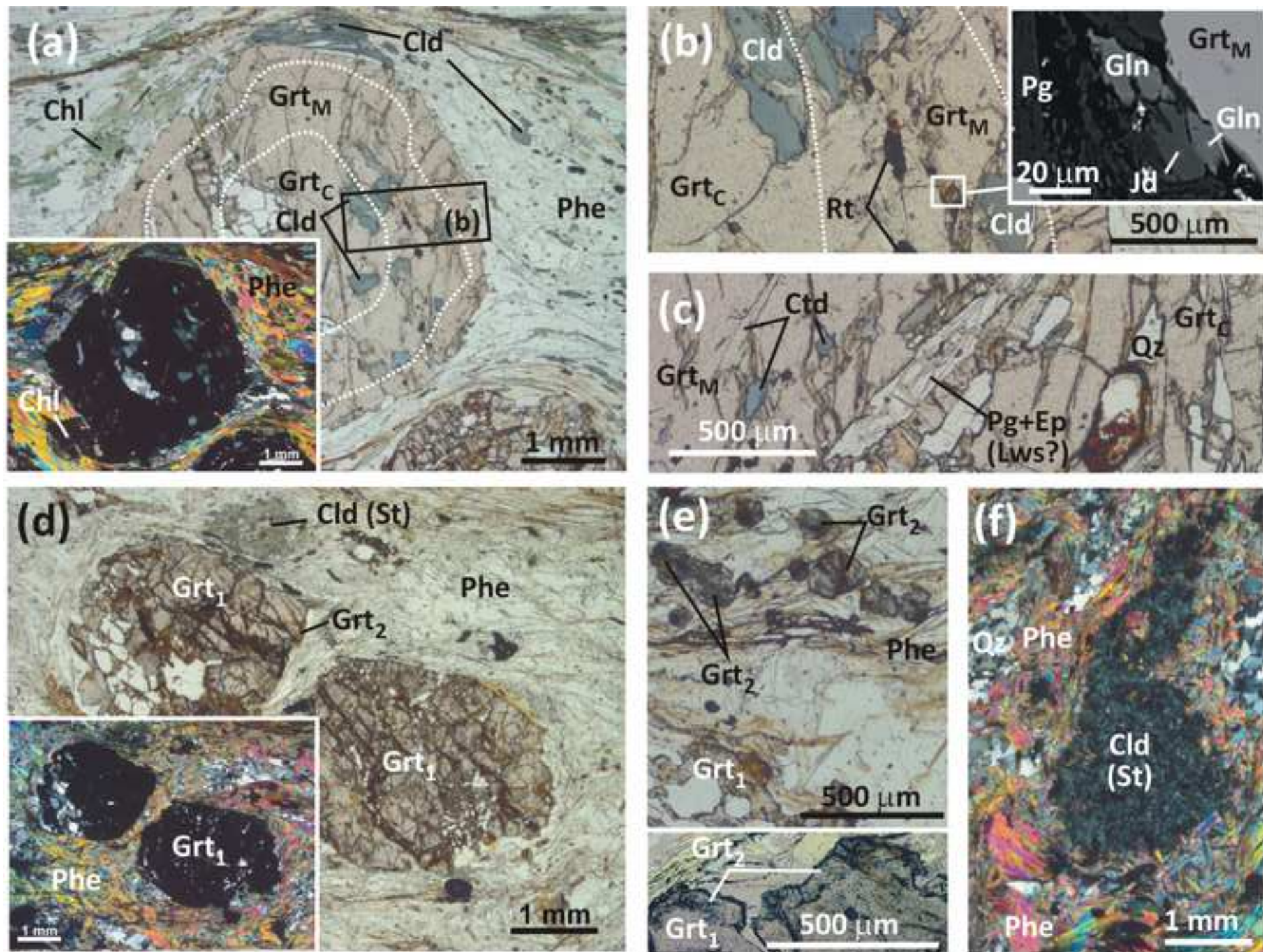
Pl

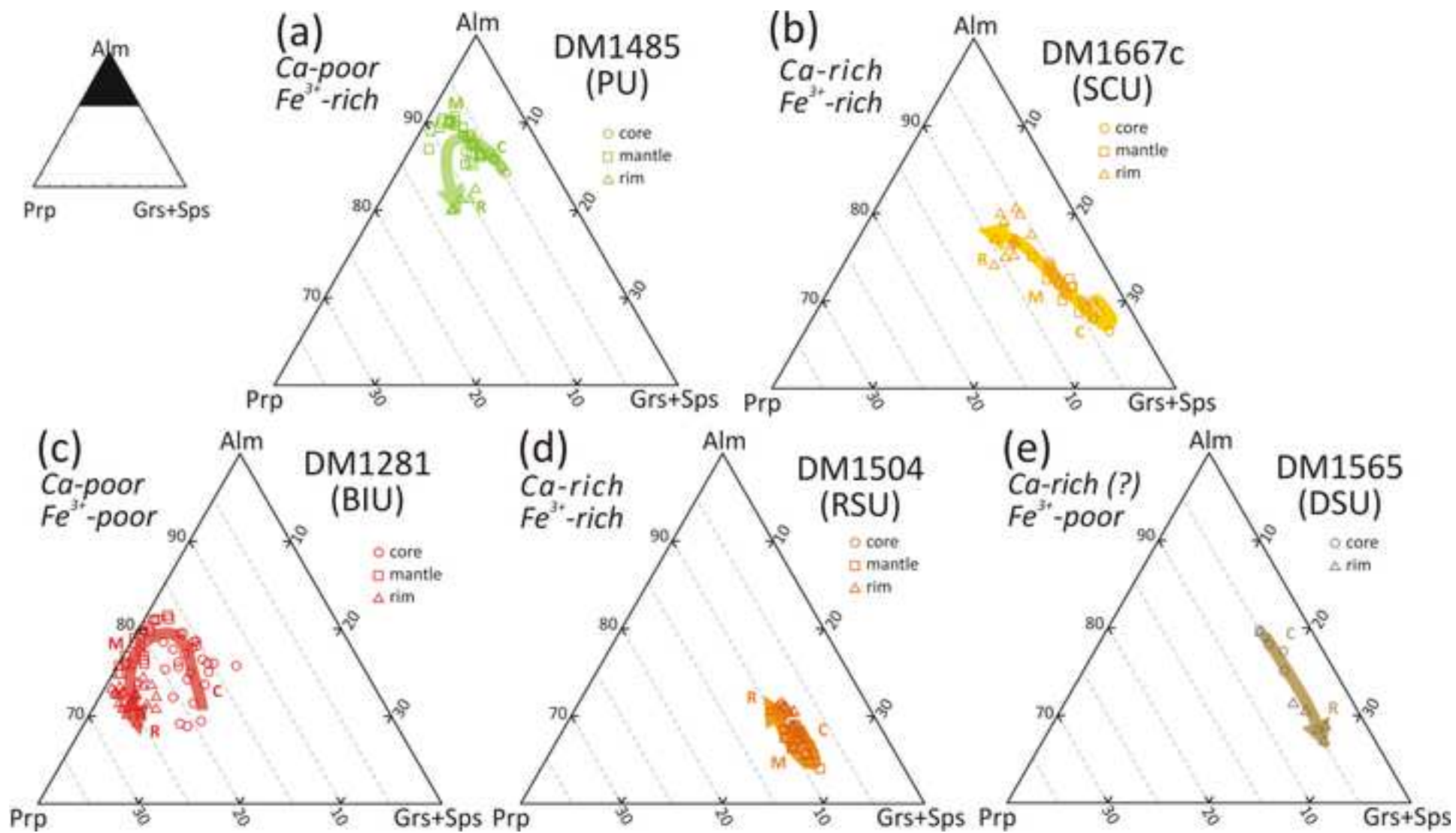
Mt

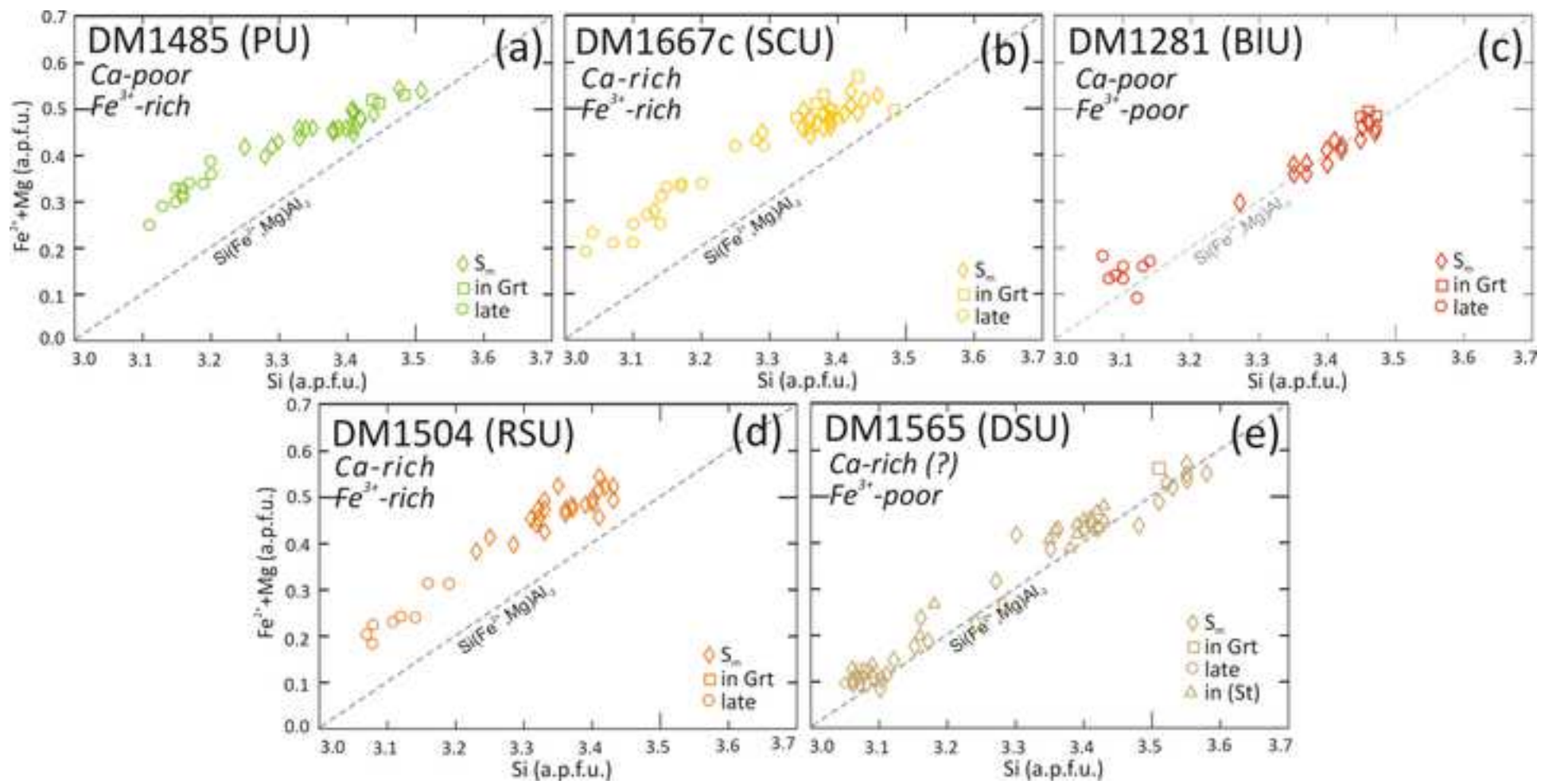
Ap



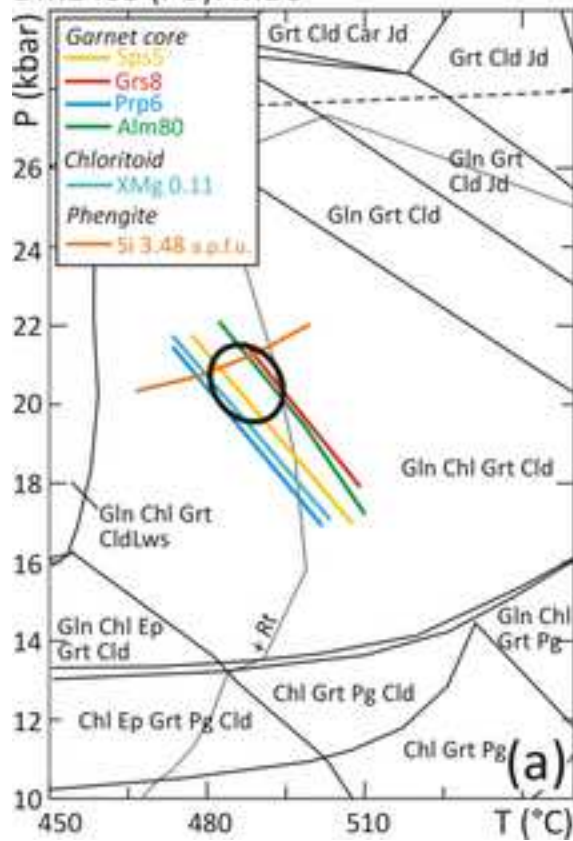
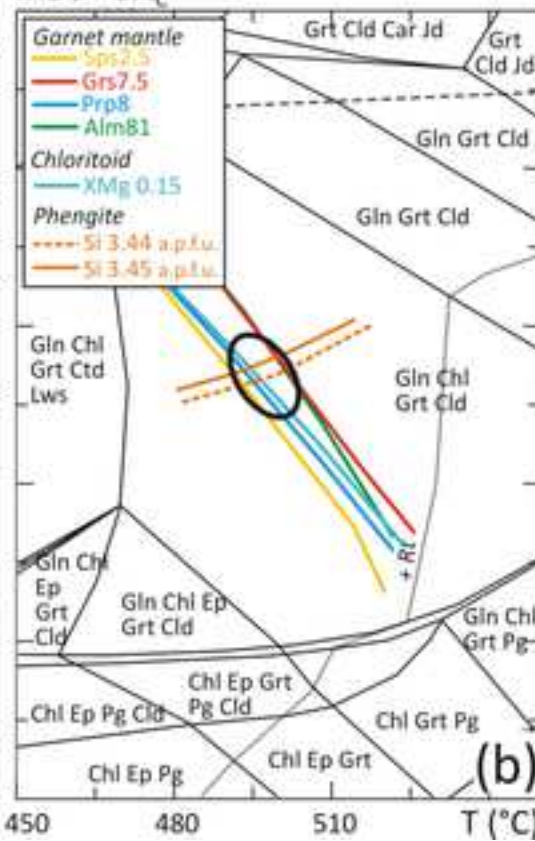
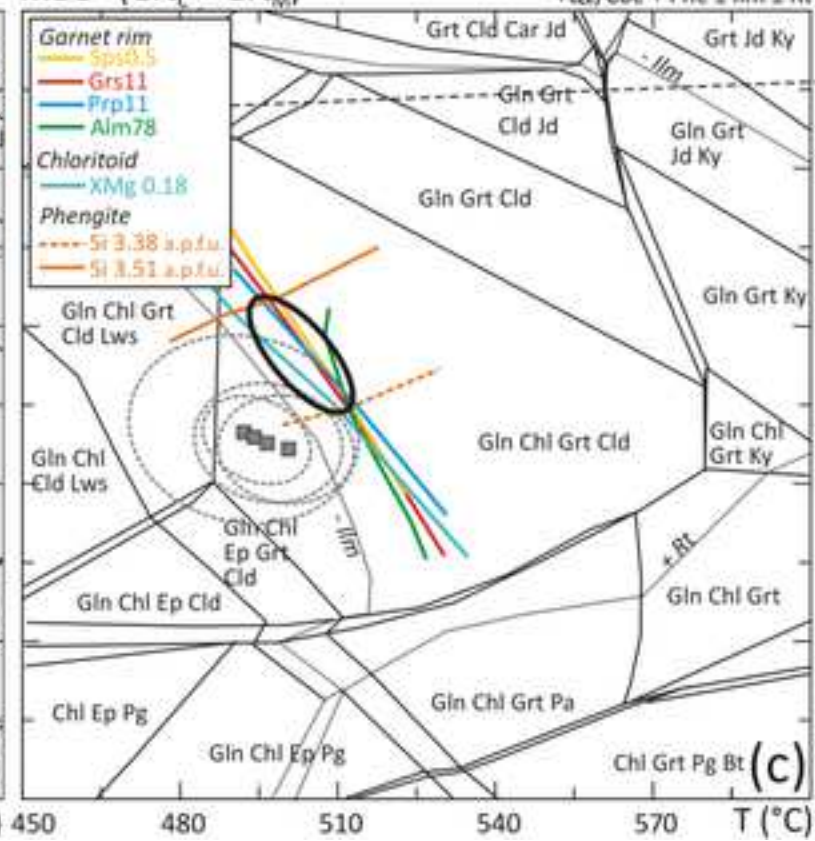






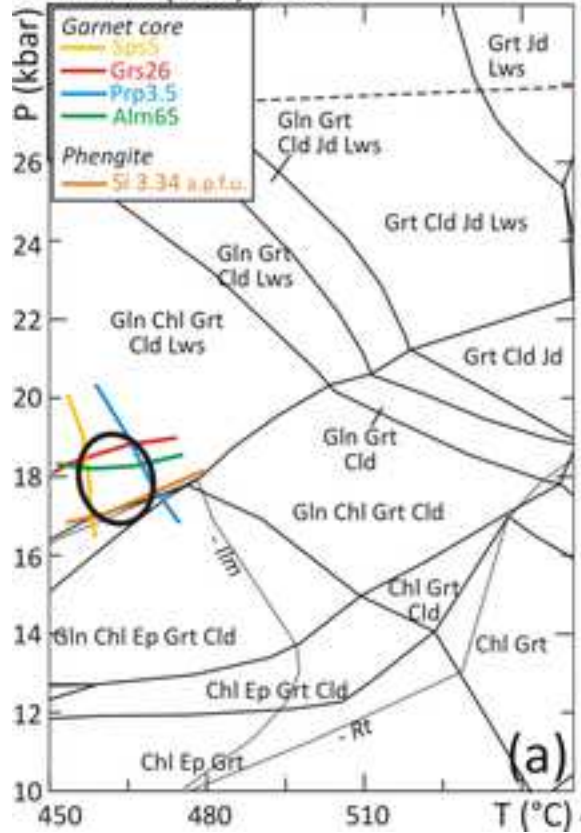


## DM1485 (PU): MBC

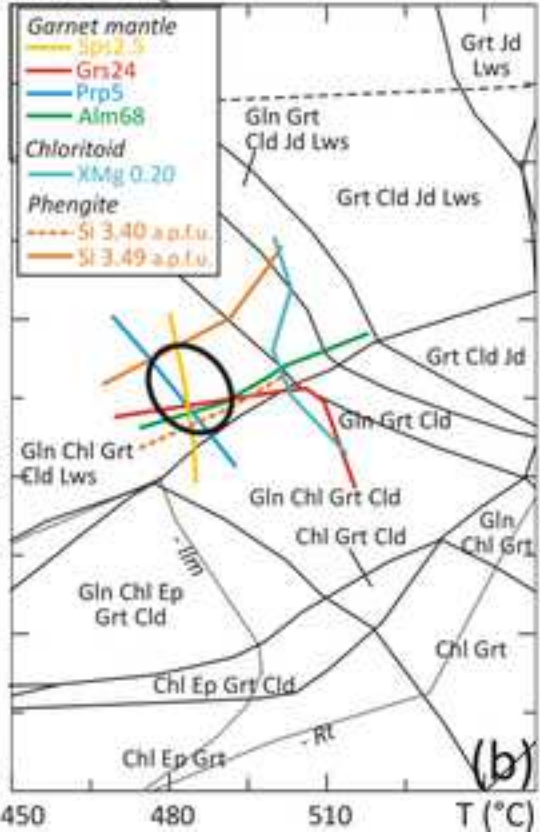
MBC - Grt<sub>C</sub>MBC - (Grt<sub>C</sub> + Grt<sub>M</sub>)



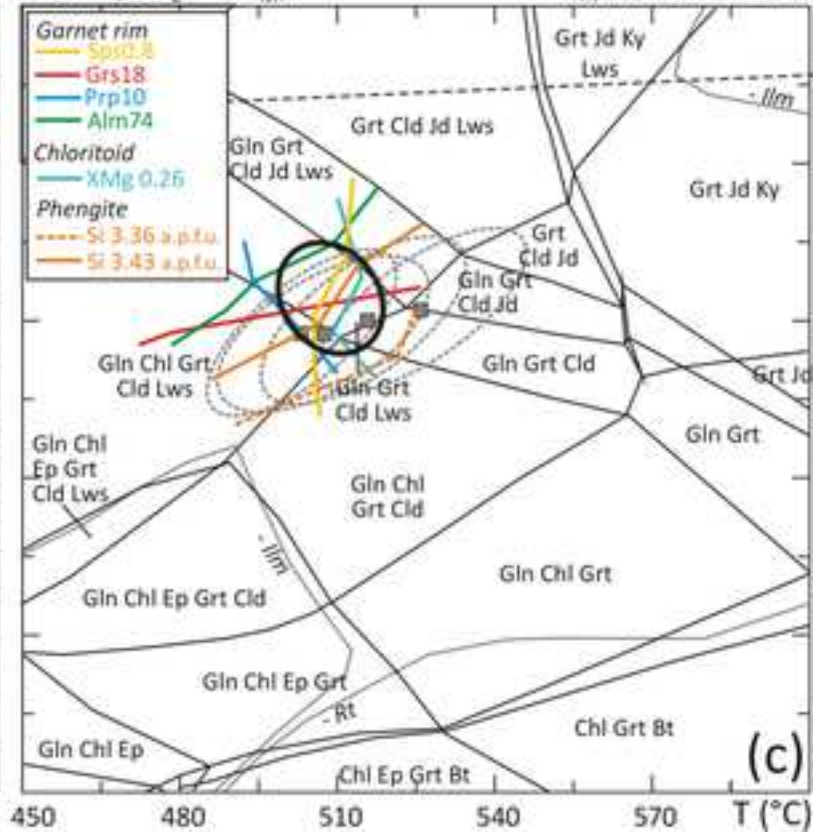
DM1667c (SCU): MBC

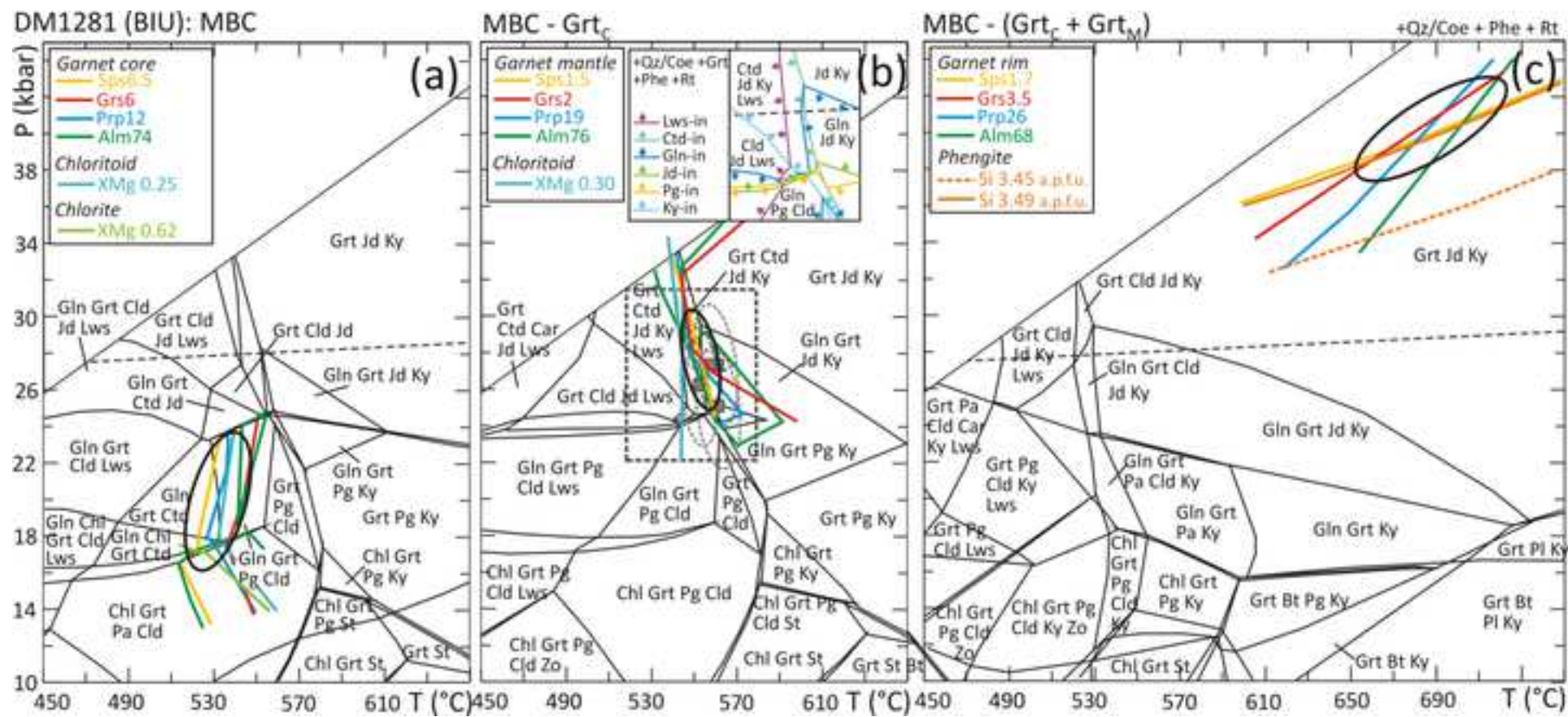


MBC - Grt<sub>c</sub>

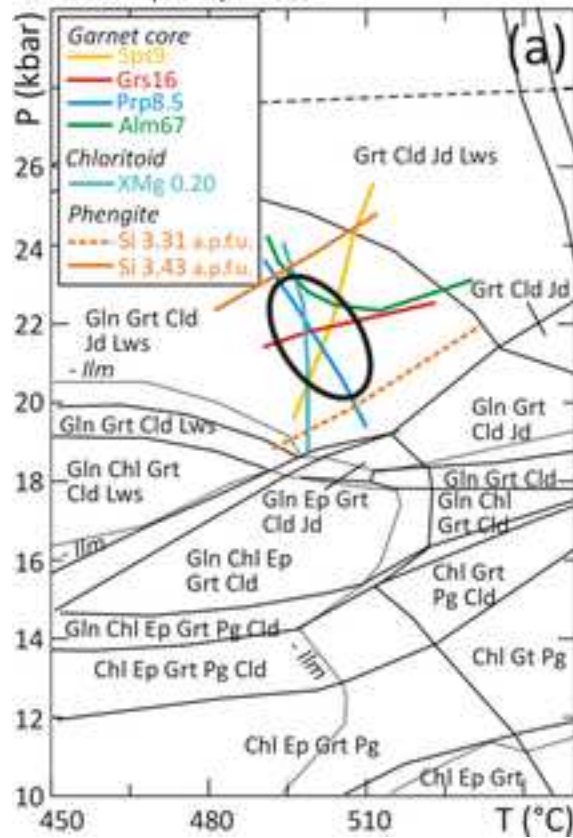
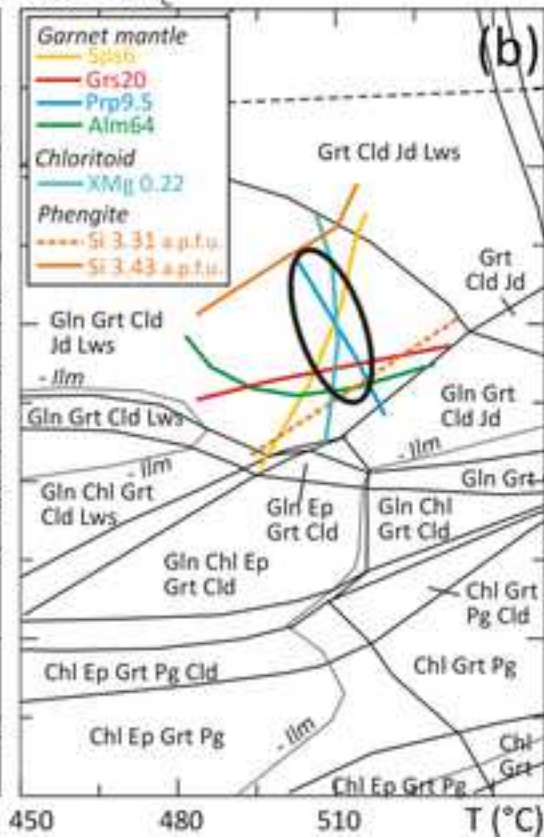
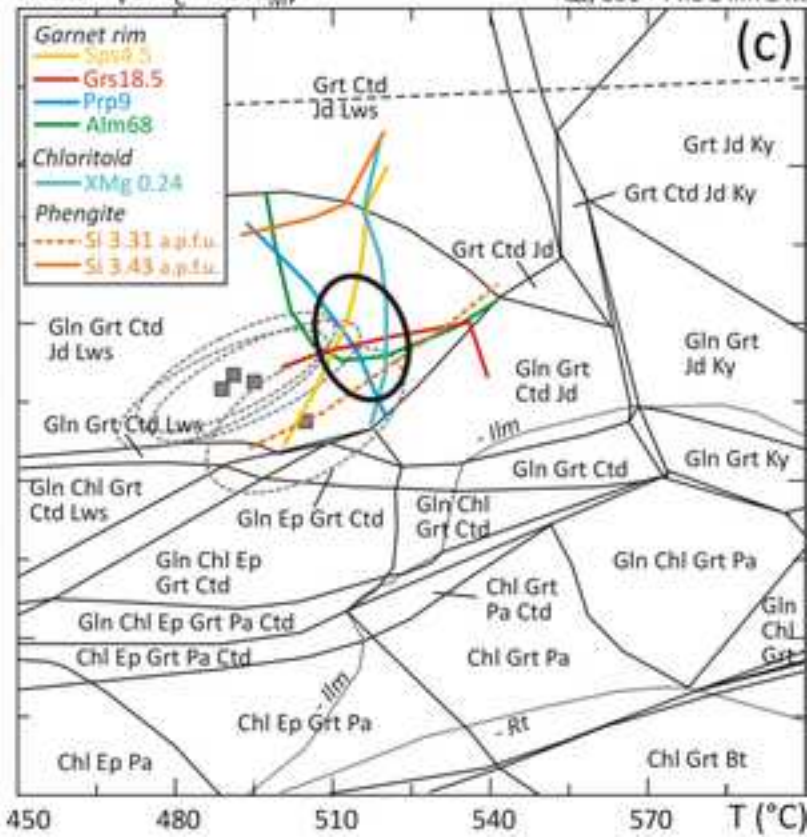


MBC - (Grt<sub>c</sub> + Grt<sub>M</sub>)





DM1504 (RSU): MBC

MBC - Grt<sub>C</sub>MBC - (Grt<sub>C</sub> + Grt<sub>M</sub>)

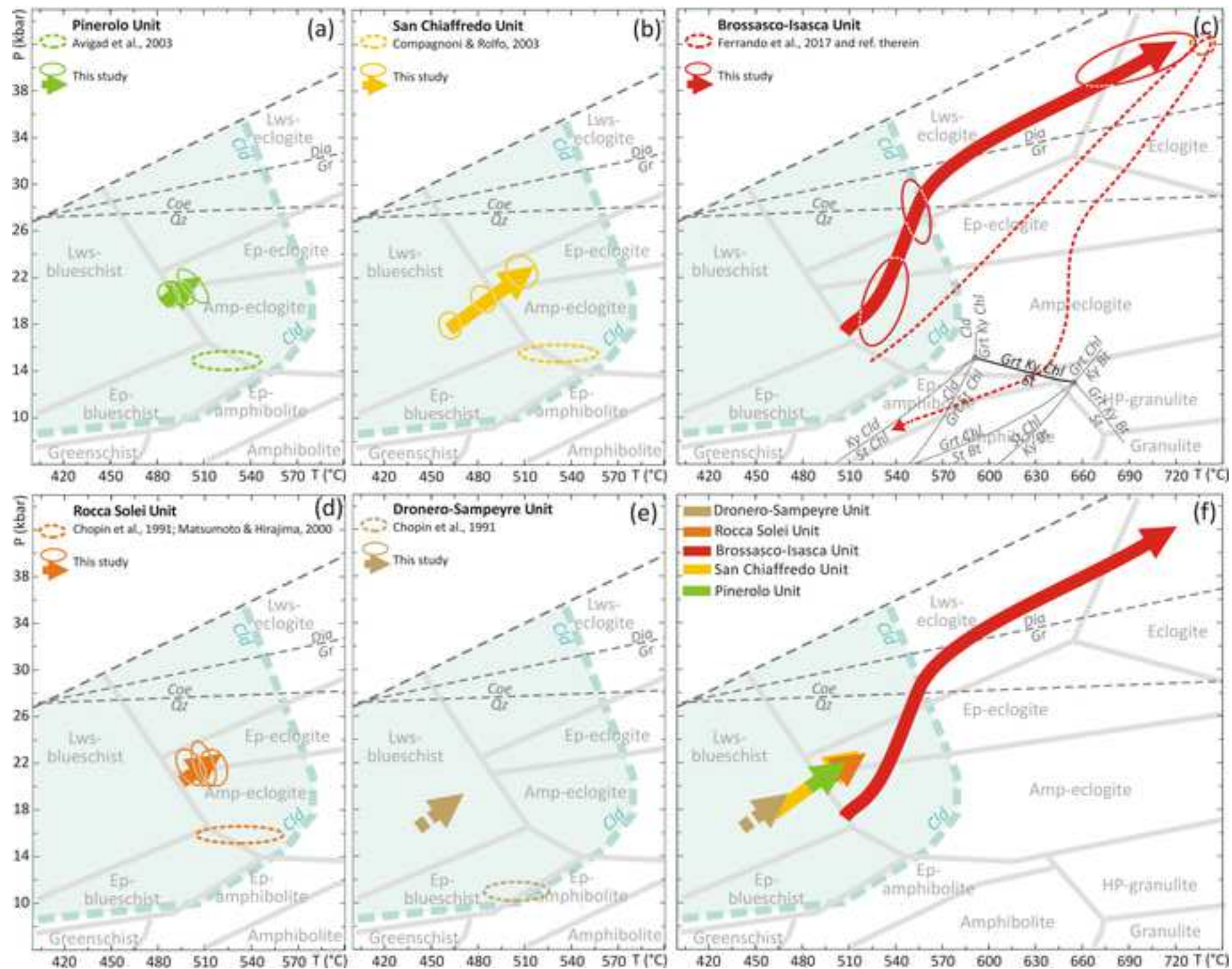


Table 1. Effective bulk-compositions (mol%) of the studied metapelites

Sample	DM1485 (PU)			DM1667c (SCU)			DM1281 (BIU)			DM1504 (RSU)		
	MBC	MBC-Grt <sub>c</sub>	MBC-(Grt <sub>c</sub> +Grt <sub>R</sub> )	MBC	MBC-Grt <sub>c</sub>	MBC-(Grt <sub>c</sub> +Grt <sub>R</sub> )	MBC	MBC-Grt <sub>c</sub>	MBC-(Grt <sub>c</sub> +Grt <sub>R</sub> )	MBC	MBC-Grt <sub>c</sub>	MBC-(Grt <sub>c</sub> +Grt <sub>R</sub> )
SiO <sub>2</sub>	55.61	57.29	59.45	58.38	58.81	64.62	64.40	67.37	71.83	62.46	62.40	63.89
TiO <sub>2</sub>	0.21	0.24	0.27	0.23	0.24	0.32	0.59	0.67	0.79	0.70	0.71	0.76
Al <sub>2</sub> O <sub>3</sub>	14.99	15.11	15.27	14.20	14.16	14.10	16.57	16.89	17.36	17.24	17.19	17.41
Fe <sub>2</sub> O <sub>3</sub>	1.07	0.92	0.73	0.94	0.92	0.61	0.00	0.00	0.00	0.53	0.51	0.43
FeO	16.67	14.50	11.42	14.74	14.45	9.60	9.84	6.71	2.01	7.84	8.07	6.78
MnO	0.38	0.12	0.02	0.33	0.27	0.06	0.29	0.09	0.02	0.28	0.23	0.05
MgO	6.99	7.54	8.12	4.03	4.09	4.80	4.23	3.93	3.00	4.20	4.19	4.21
CaO	0.76	0.56	0.46	4.27	4.09	1.84	0.49	0.26	0.15	1.68	1.60	0.98
Na <sub>2</sub> O	0.68	0.77	0.88	0.32	0.33	0.45	0.75	0.85	1.00	0.90	0.91	0.98
K <sub>2</sub> O	2.64	2.96	3.38	2.57	2.64	3.59	2.84	3.23	3.82	4.15	4.19	4.50

MBC = measured bulk-composition; MBC-Grt<sub>c</sub> = effective bulk-composition after fractionation of Grt<sub>c</sub>; MBC-(Grt<sub>c</sub>+Grt<sub>M</sub>) = effective bulk-composition after fractionation of Grt<sub>c</sub> and Grt<sub>M</sub>.

Table 2. Average P-T estimates for the peak (DM1485, DM1667c, DM1504, DM1565) and late prograde (DM1281) assemblages of the studied samples

Sample	Assemblage (+Qz/Coe* + H <sub>2</sub> O)	Phe a.p.f.u.	Si XMg	Grt XMg	Ctd XMg	Chl XMg	average T (°C)	error ( $\sigma$ ) T (°C)	average P (kbar)	error ( $\sigma$ ) P (kbar)	$\sigma$ fit	N° of reactions
DM1485 (PU)	Phe(6.1)-Grt(1.22)-Ctd(1.49)-Chl(4.7)	3.51	0.12	0.17	0.40	496	15	19	1.5	1.32	4	
	Phe(2.31)-Grt(1.2)-Ctd(1.48)-Chl(4.8)	3.48	0.10	0.16	0.40	494	11	19.1	1.1	0.81	4	
	Phe(6.11)-Grt(1.21)-Ctd(2.29)-Chl(4.9)	3.44	0.12	0.16	0.40	500	14	18.8	1.4	1.30	5	
	Phe(6.6)-Grt(1.23)-Ctd(1.33)-Chl(3.7)	3.42	0.15	0.16	0.44	492	24	19.3	2.5	2.27	5	
	<i>weighted mean**</i>					496	7	19.0	0.7			
DM1667c (SCU)	Phe(7.17)-Grt(2.24)-Ctd(1.5)-Lws	3.46	0.08	0.28		526	16	22.3	1.7	0.78	4	
	Phe(10.1)-Grt(9.22)-Ctd(2.52)-Lws	3.44	0.09	0.23		503	15	21.7	1.7	0.27	4	
	Phe(10.9)-Grt(2.25)-Ctd(2.49)-Lws	3.44	0.10	0.23		515	16	22.0	1.8	0.76	3	
	Phe(1.18)-Grt(9.1)-Ctd(2.40)-Lws	3.43	0.08	0.22		507	16	21.7	1.7	0.25	3	
	<i>weighted mean**</i>					512	8	21.9	0.9			
DM1281 (BIU)	Phe(12.2)-Grt(6.3)-Ctd(5.7)-Ky	3.47	0.24	0.31		560	9	27.5	2.9	1.03	3	
	Phe(12.1)-Grt(6b.1)-Ctd(6.49)-Ky	3.45	0.25	0.30		552	9	26.3	2.7	0.43	3	
	Phe(6.88)-Grt(6.32)-Ctd(6.36)-Ky	3.45	0.24	0.31		561	10	25.2	3.1	1.09	3	
	Phe(8.3)-Grt(10.13)-Ctd(6.33)-Ky	3.46	0.24	0.29		557	9	27.5	0.4	0.83	4	
	<i>weighted mean**</i>					557	5	27.4	0.4			
DM1504 (RSU)	Phe(2.34)-Grt(2.2)-Ctd(2.35)-Gln(2.52)-Jd(2.44)-Lws	3.42	0.09	0.22		491	15	20.7	1.2	1.24	7	
	Phe(6.21)-Grt(2.26)-Ctd(4.4)-Gln(2.52)-Jd(2.44)-Lws	3.43	0.10	0.23		505	16	19.5	1.6	1.22	5	
	Phe(6.16)-Grt(1.19)-Ctd(6.8)-Gln(2.52)-Jd(2.44)-Lws	3.41	0.09	0.23		489	16	20.3	1.2	1.30	6	
	Phe(6.3)-Grt(2.1)-Ctd(2.32)-Gln(2.52)-Jd(2.44)-Lws	3.43	0.09	0.23		495	16	20.5	1.2	1.31	7	
	<i>weighted mean**</i>					495	8	20.3	0.6			
DM1565 (DSU)	Phe(5.12)-Grt(3.15)-Ctd(2.3)-Lws	3.55	0.06	0.17		466	14	18.8	1.5	0.15	3	
	Phe(5.6)-Grt(3.11)-Ctd(2.32)-Lws	3.55	0.05	0.18		446	14	16.4	1.3	0.29	3	
	Phe(3.6)-Grt(7.1)-Ctd(2.25)-Lws	3.58	0.05	0.15		444	14	16.8	1.3	0.55	3	
	<i>weighted mean**</i>					452	8	17.2	0.8			

\*Coe for sample DM1281

\*\*Weighted mean (with error) implies that values with smaller errors weight more than values with bigger errors.

## What's in the sandwich? New P-T constraints for the (U)HP nappe stack of southern Dora-Maira Massif (Western Alps)

submitted to *European Journal of Mineralogy* (Ref: ejm190006) by

Chiara Groppo, Simona Ferrando, Manuele Gilio, Serena Botta, Francesco Nosenzo, Gianni Balestro, Andrea Festa, Franco Rolfo

### SUPPLEMENTARY MATERIAL

#### Sample locations

The five metapelite samples studied in this paper are part of the rich collection of thin sections from the southern DMM hosted at the Department of Earth Sciences of the University of Torino (Italy). Sample locations are reported in Fig. 1 and additional details are given below.

- **Sample DM1485 (PU)** was collected from a small (few metres) outcrop of garnet-bearing micaschists exposed at Case dei Canaveis, in the Comba Albetta valley (right tributary of the Po river, west of Sanfront).
- **Sample DM1667c (SCU)** was collected at Piano Pramalano, at the head of Isasca Valley (few tens of metres below the ridge separating the Isasca Valley from the Po Valley). Outcrop exposure is very poor and the sample was collected from the debris along the road; however, because the debris is totally composed of similar micaschists, we suppose that this is the dominant lithology of the area.
- **Sample DM1281 (BIU)** was collected from an outcrop located east of Piano la Ruota, at the head of the Rio Lavesio Valley (a right tributary of the Po river, south-west of Martiniana Po; the same small valley where there is the well-known locality of Case Parigi). The outcrop consists of a ten of metres thick level of metapelites hosted within augen-gneiss. A sample from the same outcrop was described by Compagnoni *et al.* (1994) in the guidebook for the field excursion organized for the 16<sup>th</sup> meeting of IMA.
- **Sample DM1504 (RSU)** was collected from a 20-50 m -thick layer of metapelites exposed on the ridge separating the Gilba Valley from the Po Valley, west of M. Scolagarda.
- **Sample DM1565 (DSU)** was collected close to the Santuario di Valmala at the head of the Valmala Valley, few hundred metres below the ridge between the Varaita and Maira Valleys. Henry (1990) described similar micaschists exposed south of Meira Palancia as “micaschistes amigdalaires” and reported the occurrence of relics of pre-Alpine staurolite only partially replaced by a fine-grained aggregate of chloritoid.

Compagnoni, R., Messiga, B., Castelli, D. (1994): High pressure metamorphism in the Western Alps. *in*: “Guidebook to the field excursion B1”, 16th General Meeting of the International Mineralogical Association, Pisa, Italy, 148 pp.

Henry, C. (1990): L'unité à coesite du massif Dora-Maira dans son cadre pétrologique et structurale (Alpes Occidentales, Italie). Thèse Doctorat., Université Paris 6, 149 pp.

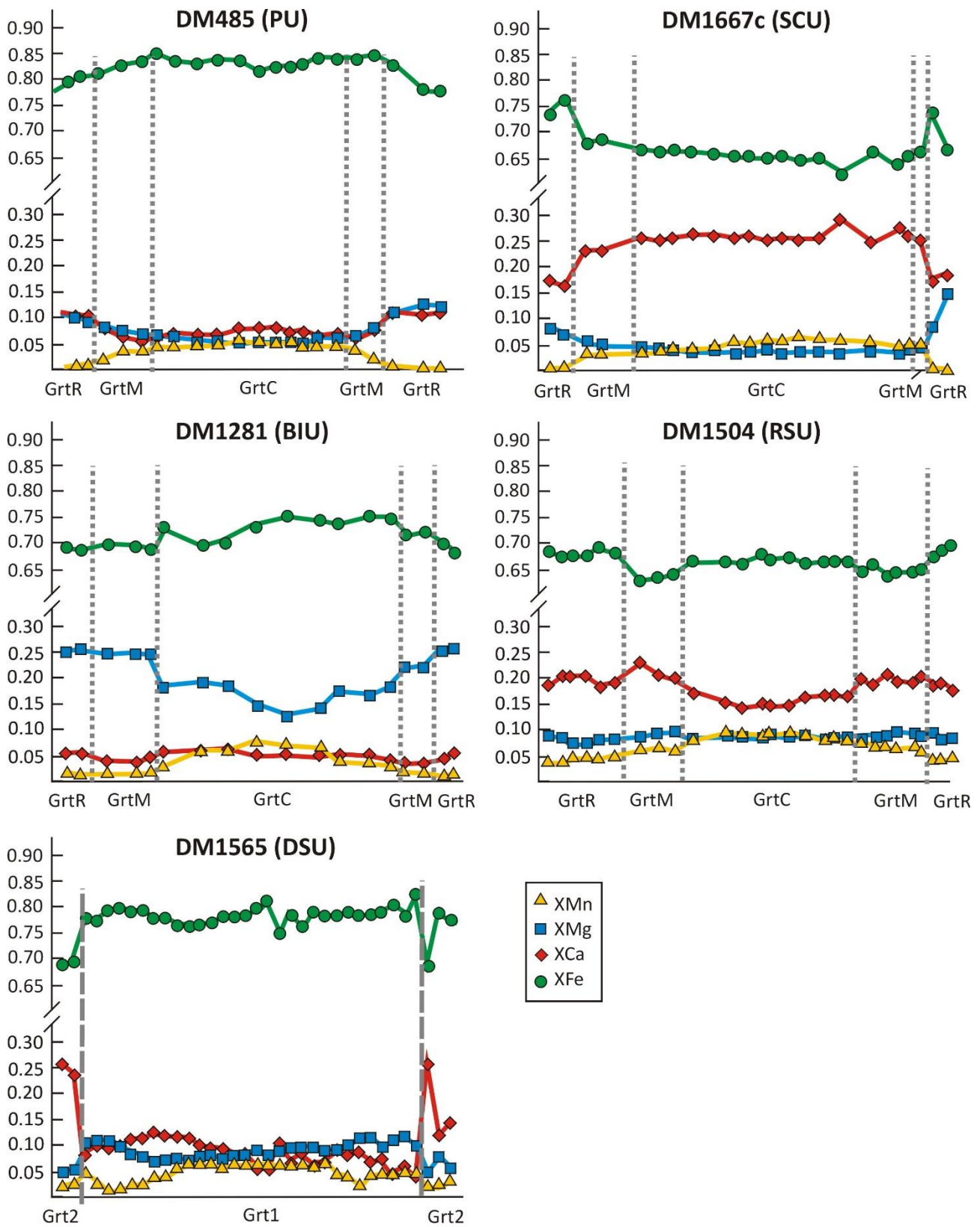


**Fig. SM1** – Compositional profiles of garnet porphyroblasts from the investigated samples.



**Table SM1a - Compositional variations of the main minerals in samples DM1485 (PU), DM1667c (SCU) and DM1281 (BIU)**

<b>DM1485 (PU)</b>					<b>DM1667c (SCU)</b>					<b>DM1281 (BIU)</b>				
<b>Garnet</b>					<b>Garnet</b>					<b>Garnet</b>				
	Sps	Prp	Grs	Alm		Sps	Prp	Grs	Alm		Sps	Prp	Grs	Alm
GrtC	4-6	5-7	7-9	80-83	GrtC	4-7	3-4	25-27	64-66	GrtC	3-8	12-16	5-6	73-77
GrtM	2-3	7-9	7-8	81-84	GrtM	2-3	4-6	18-19	73-75	GrtM	0.5-2	17-21	1-3	74-79
GrtR	0.3-1	9-12	10-11	77-81	GrtR	0.5-1	7-10	16-20	72-76	GrtR	1-2	22-26	3-5	68-72
<b>Phengite</b>					<b>Phengite</b>					<b>Phengite</b>				
	Si (a.p.f.u.)					Si (a.p.f.u.)					Si (a.p.f.u.)			
Sm	3.38-3.51				Sm	3.35-3.46				Sm	3.35-3.49			
in GrtC	3.48				in GrtC	3.34				in GrtR	3.45-3.47			
in GrtM	3.44-3.45				in GrtM	3.40-3.49				<b>Chloritoid</b>				
<b>Chloritoid</b>					<b>Chloritoid</b>					<b>Chloritoid</b>				
	XMg					XMg					XMg			
in GrtC	0.10-0.12				in GrtC/M	0.20-0.28				in GrtC/M	0.25-0.31			
in GrtM	0.13-0.16				in GrtR	0.25-0.28				<b>Chlorite</b>				
in GrtR	0.17-0.18				<b>Chlorite</b>					<b>Chlorite</b>				
<b>Chlorite</b>					<b>Chlorite</b>					<b>Chlorite</b>				
	XMg					XMg					XMg			
Sm	0.40-0.44				in GrtC/M	0.20-0.26				in GrtM	0.59-0.66			
late	0.37-0.38				late	0.37-0.42				in GrtC	0.33-0.50			
<b>Biotite</b>					<b>Biotite</b>					<b>Staurolite</b>				
	XMg					XPs					XMg			
late	0.38-0.40				in GrtC/M	0.50-0.84				in GrtC/M	0.15-0.25			
<b>Biotite</b>					<b>Biotite</b>					<b>Biotite</b>				
	XMg					XMg				<b>Biotite</b>				
late	0.35-0.42				late	0.32-0.46				<b>Biotite</b>				
<b>Biotite</b>					<b>Biotite</b>					<b>Biotite</b>				
	XMg					XMg				<b>Biotite</b>				
late	0.35-0.42				<b>Biotite</b>					<b>Biotite</b>				

**Table SM1b - Compositional variations of the main minerals in samples DM1504 (RSU) and DM1565 (DSU)**

<b>DM1504 (RSU)</b>					<b>DM1565 (DSU)</b>				
<b>Garnet</b>	Sps	Prp	Grs	Alm	<b>Garnet 1</b>	Sps	Prp	Grs	Alm
GrtC	7-10	8-9	14-18	66-69	GrtC	3-7	6-9	5-10	75-80
GrtM	5-7	9-10	19-21	63-65	GrtM	1-2	9.11	9-12	78-80
GrtR	4-5	8-10	17-20	66-70	GrtR	2-5	10-12	4-9	78-82
<b>Phengite</b>	Si (a.p.f.u.)				<b>Garnet 2</b>	Sps	Prp	Grs	Alm
Sm	3.31-3.43				GrtC	2-4	4-5	14-16	75-78
<b>Chloritoid</b>	XMg				GrtR	2-3	5-6	21-26	67-72
Sm CtdC	0.19-0.21				<b>Phengite</b>	Si (a.p.f.u.)			
Sm CtdR	0.22-0.24				Sm	3.48-3.58			
in GrtC	0.19-0.21				<b>Chloritoid</b>	XMg			
in GrtM	0.21-0.23				Sm; after St	0.13-0.18			
in GrtR	0.22-0.24				<b>Chlorite</b>	XMg			
<b>Glaucophane</b>	XMg	XNa			late	0.40-0.44			
in GrtM/R	0.38-0.42	0.91-0.94							
<b>Jadeite</b>	XJd	XAeg							
in GrtM/R	0.66-0.74	0.26-0.34							
<b>Epidote</b>	XPs								
late (in Grt)	0.53-0.63								
late (matrix)	0.55-0.71								
<b>Chlorite</b>	XMg								
late	0.42-0.47								

**Table SM2a - Representative analyses of the main minerals in sample DM1485 (PU)**

Analysis	White mica								Garnet					
	1.39 Phe	1.35 Phe	6.1 Phe*	2.31 Phe*	6.11 Phe*	6.6 Phe*	4.6 Ms	1.43 Pg	1.12 Grt	1.19 Grt	1.22 Grt*	1.2 Grt*	1.21 Grt*	1.23 Grt*
Site	In Grt <sub>c</sub>	In Grt <sub>M</sub>	// S <sub>m</sub>	// S <sub>m</sub>	// S <sub>m</sub>	// S <sub>m</sub>	late	In Grt <sub>M</sub>	Core	Mantle	Rim	Rim	Rim	Rim
SiO <sub>2</sub>	52.86	52.32	53.71	53.42	52.51	52.01	47.63	47.30	36.55	36.41	36.79	36.77	37.04	37.53
TiO <sub>2</sub>	0.00	0.00	0.00	0.00	0.00	0.00	0.00	0.00	0.00	0.00	0.00	0.00	0.00	0.00
Al <sub>2</sub> O <sub>3</sub>	26.37	27.19	26.21	26.76	27.49	27.84	32.96	39.85	20.36	20.27	20.77	20.65	20.96	21.01
FeO	4.65	4.75	2.96	2.86	3.26	2.55	3.88	0.96	36.66	36.95	35.00	35.54	35.21	31.73
MnO	0.00	0.00	0.00	0.00	0.00	0.00	0.00	0.00	2.17	0.99	0.07	0.36	0.08	0.11
MgO	2.74	2.69	3.93	3.88	3.20	3.50	1.16	0.00	1.18	1.85	2.91	2.42	3.03	3.69
CaO	0.00	0.00	0.00	0.00	0.00	0.00	0.00	0.00	2.68	2.49	3.71	3.48	3.47	5.78
Na <sub>2</sub> O	0.66	0.70	0.00	0.00	0.61	0.85	1.32	8.07	0.00	0.00	0.00	0.00	0.00	0.00
K <sub>2</sub> O	9.15	9.18	9.90	9.98	9.54	9.39	9.16	0.00	0.00	0.00	0.00	0.00	0.00	0.00
Total	96.43	96.83	96.72	96.89	96.61	96.15	96.11	96.21	99.67	99.06	99.36	99.29	99.88	99.95
Si	3.48	3.44	3.51	3.48	3.44	3.42	3.16	2.99	2.99	2.99	2.98	2.99	2.98	2.98
Ti	0.00	0.00	0.00	0.00	0.00	0.00	0.00	0.00	0.00	0.00	0.00	0.00	0.00	0.00
Al	2.05	2.11	2.02	2.06	2.12	2.16	2.58	2.97	1.97	1.96	1.98	1.98	1.99	1.97
Fe <sup>+3</sup>	0.00	0.00	0.00	0.00	0.00	0.00	0.00	0.02	0.04	0.06	0.07	0.05	0.06	0.06
Fe <sup>+2</sup>	0.26	0.26	0.16	0.16	0.18	0.14	0.22	0.03	2.47	2.47	2.30	2.37	2.31	2.05
Mn	0.00	0.00	0.00	0.00	0.00	0.00	0.00	0.00	0.15	0.07	0.00	0.02	0.01	0.01
Mg	0.27	0.26	0.38	0.38	0.31	0.34	0.11	0.00	0.14	0.23	0.35	0.29	0.36	0.44
Ca	0.00	0.00	0.00	0.00	0.00	0.00	0.00	0.00	0.23	0.22	0.32	0.30	0.30	0.49
Na	0.08	0.09	0.00	0.00	0.08	0.11	0.17	0.99	0.00	0.00	0.00	0.00	0.00	0.00
K	0.00	0.00	0.83	0.83	0.80	0.79	0.78	0.00	0.00	0.00	0.00	0.00	0.00	0.00
XMg	0.51	0.50	0.70	0.71	0.64	0.71	0.35	0.00	0.05	0.08	0.12	0.10	0.12	0.15
XFe									0.82	0.83	0.77	0.79	0.78	0.69
XCa									0.08	0.07	0.11	0.10	0.10	0.17
XMn									0.05	0.02	0.00	0.01	0.00	0.00

\* Analysis used for AvPT calculations (see Table 2)

Structural formulae have been calculated on the basis of 11 oxygens for white mica and 12 oxygens for garnet.

Fe<sup>3+</sup> has been calculated by stoichiometry

**Table SM2b - Representative analyses of the main minerals in sample DM1485 (PU)**

Analysis Site	Chloritoid						Chlorite			
	1.28 Cl <sub>d</sub> In Grt <sub>c</sub>	1.46 Cl <sub>d</sub> In Grt <sub>M</sub>	1.49 Cl <sub>d</sub> * In Grt <sub>R</sub>	1.48 Cl <sub>d</sub> * In Grt <sub>R</sub>	2.29 Cl <sub>d</sub> * In Grt <sub>R</sub>	1.33 Cl <sub>d</sub> * In Grt <sub>R</sub>	4.7 Chl* // S <sub>m</sub>	4.8 Chl* // S <sub>m</sub>	4.9 Chl* // S <sub>m</sub>	3.7 Chl* // S <sub>m</sub>
SiO <sub>2</sub>	24.60	24.60	24.59	25.10	24.63	24.91	24.60	25.05	24.62	25.45
TiO <sub>2</sub>	0.00	0.00	0.00	0.00	0.00	0.00	0.00	0.00	0.00	0.00
Al <sub>2</sub> O <sub>3</sub>	39.72	39.51	39.61	40.40	40.21	40.08	22.03	21.78	21.81	21.82
FeO	27.10	26.47	25.87	25.42	25.40	25.82	30.44	30.65	30.38	28.90
MnO	0.00	0.00	0.00	0.00	0.00	0.00	0.00	0.00	0.00	0.00
MgO	1.77	2.38	2.91	2.80	2.79	2.72	11.27	11.39	11.47	12.50
CaO	0.00	0.00	0.00	0.00	0.00	0.00	0.00	0.00	0.00	0.00
Na <sub>2</sub> O	0.00	0.00	0.00	0.00	0.00	0.00	0.00	0.00	0.00	0.00
K <sub>2</sub> O	0.00	0.00	0.00	0.00	0.00	0.00	0.00	0.00	0.00	0.00
Total	93.28	93.1	93.17	93.77	93.13	93.63	88.34	88.87	88.28	88.68
Si	2.04	2.03	2.02	2.05	2.02	2.04	2.65	2.68	2.65	2.71
Ti	0.00	0.00	0.00	0.00	0.00	0.00	0.00	0.00	0.00	0.00
Al	3.87	3.85	3.84	3.88	3.89	3.86	2.80	2.75	2.77	2.74
Fe <sup>+3</sup>	0.06	0.09	0.11	0.03	0.06	0.06	0.00	0.00	0.00	0.00
Fe <sup>+2</sup>	1.82	1.74	1.67	1.71	1.68	1.71	2.74	2.75	2.74	2.57
Mn	0.00	0.00	0.00	0.00	0.00	0.00	0.00	0.00	0.00	0.00
Mg	0.22	0.29	0.36	0.34	0.34	0.33	1.81	1.82	1.84	1.98
Ca	0.00	0.00	0.00	0.00	0.00	0.00	0.00	0.00	0.00	0.00
Na	0.00	0.00	0.00	0.00	0.00	0.00	0.00	0.00	0.00	0.00
K	0.00	0.00	0.00	0.00	0.00	0.00	0.00	0.00	0.00	0.00
XMg	0.11	0.14	0.18	0.17	0.17	0.16	0.40	0.40	0.40	0.44

\* Analysis used for AvPT calculations (see Table 2)

Structural formulae have been calculated on the basis of 14 oxygens for chloritoid and 18 oxygens for chlorite.

Fe<sup>3+</sup> has been calculated by stoichiometry

**Table SM3a - Representative analyses of the main minerals in sample DM1667c (SCU)**

Analysis	White mica								Garnet					
	9.28 Phe	9.29 Phe	7.19 Phe	7.17 Phe*	10.1 Phe*	10.9 Phe*	1.18 Phe*	2.27 Pa	9.11 Grt	9.4 Grt	2.24 Grt*	9.22 Grt*	2.25 Grt*	9.1 Grt*
Site	In Grt <sub>c</sub>	In Grt <sub>M</sub>	In Grt <sub>R</sub>	// S <sub>m</sub>	// S <sub>m</sub>	// S <sub>m</sub>	// S <sub>m</sub>	In Grt <sub>M</sub>	Core	Mantle	Rim	Rim	Rim	Rim
SiO <sub>2</sub>	50.42	53.00	51.56	52.25	52.44	52.22	52.28	47.14	36.70	36.79	37.01	36.82	36.55	37.04
TiO <sub>2</sub>	0.45	0.00	0.38	0.00	0.00	0.00	0.00	0.00	0.00	0.00	0.00	0.00	0.00	0.00
Al <sub>2</sub> O <sub>3</sub>	28.68	26.56	26.26	26.59	27.00	27.25	27.66	40.04	20.15	20.50	20.73	20.69	20.24	20.57
FeO	3.36	3.52	4.36	3.55	3.41	3.88	3.35	0.63	30.67	31.54	33.16	33.87	32.36	33.46
MnO	0.00	0.00	0.00	0.00	0.00	0.00	0.00	0.00	2.35	1.48	0.49	0.32	0.82	0.34
MgO	2.90	3.15	3.36	3.32	3.40	3.18	3.19	0.00	0.88	1.23	1.95	2.12	2.36	2.07
CaO	0.00	0.00	0.00	0.00	0.00	0.00	0.00	0.32	8.81	7.97	6.18	5.80	6.52	5.97
Na <sub>2</sub> O	0.91	0.87	0.56	0.62	0.57	0.00	0.58	7.72	0.00	0.00	0.00	0.00	0.00	0.00
K <sub>2</sub> O	9.47	9.00	9.76	9.78	9.98	10.18	9.86	0.21	0.00	0.00	0.00	0.00	0.00	0.00
Total	96.19	96.10	96.24	96.11	96.80	96.71	96.92	96.06	99.55	99.52	99.53	99.62	98.85	99.46
Si	3.34	3.49	3.43	3.46	3.44	3.44	3.43	2.99	2.970	2.974	2.987	2.970	2.964	2.992
Ti	0.02	0.00	0.02	0.00	0.00	0.00	0.00	0.00	0.00	0.00	0.00	0.00	0.00	0.00
Al	2.24	2.06	2.06	2.07	2.09	2.11	2.14	2.99	1.923	1.953	1.972	1.967	1.934	1.959
Fe <sup>+3</sup>	0.00	0.00	0.00	0.00	0.00	0.00	0.00	0.00	0.137	0.099	0.054	0.094	0.139	0.057
Fe <sup>+2</sup>	0.19	0.19	0.24	0.20	0.19	0.21	0.18	0.03	1.940	2.034	2.184	2.192	2.056	2.203
Mn	0.00	0.00	0.00	0.00	0.00	0.00	0.00	0.00	0.161	0.102	0.034	0.022	0.056	0.023
Mg	0.29	0.31	0.33	0.33	0.33	0.31	0.31	0.00	0.106	0.149	0.235	0.255	0.285	0.249
Ca	0.00	0.00	0.00	0.00	0.00	0.00	0.00	0.02	0.764	0.690	0.535	0.501	0.567	0.517
Na	0.12	0.11	0.07	0.08	0.07	0.00	0.07	0.95	0.00	0.00	0.00	0.00	0.00	0.00
K	0.80	0.76	0.83	0.83	0.84	0.85	0.82	0.02	0.00	0.00	0.00	0.00	0.00	0.00
XMg	0.606	0.615	0.579	0.625	0.64	0.594	0.629	0.00	0.04	0.05	0.08	0.09	0.10	0.08
XFe									0.65	0.68	0.73	0.74	0.69	0.74
XCa									0.26	0.23	0.18	0.17	0.19	0.17
XMn									0.05	0.03	0.01	0.01	0.02	0.01

\* Analysis used for AvPT calculations (see Table 2)

Structural formulae have been calculated on the basis of 11 oxygens for white mica and 12 oxygens for garnet.

Fe<sup>3+</sup> has been calculated by stoichiometry

**Table SM3b - Representative analyses of the main minerals in sample DM1667c (SCU)**

Analysis Site	Chloritoid				Epidote		Chlorite	
	1.5 Cld* In Grt <sub>R</sub>	2.52 Cld* In Grt <sub>M</sub>	2.49 Cld* In Grt <sub>M</sub>	2.40 Cld* In Grt <sub>M</sub>	11.12 Ep In Grt <sub>C</sub>	9.27 Ep In (Lws)	1.22 Chl In Grt <sub>C</sub>	3.1 Chl late
SiO <sub>2</sub>	25.13	25.35	25.13	25.01	38.47	38.63	23.59	24.66
TiO <sub>2</sub>	0.00	0.00	0.00	0.00	0.00	0.00	0.00	0.00
Al <sub>2</sub> O <sub>3</sub>	40.92	40.67	40.86	40.67	25.47	29.15	20.32	21.54
FeO	22.61	23.72	23.15	23.55	10.63	6.15	37.03	31.18
MnO	4.82	4.03	3.92	3.74	0.00	0.00	0.55	0.00
MgO	0.00	0.00	0.00	0.00	0.00	0.00	7.01	11.43
CaO	0.00	0.00	0.00	0.00	22.15	23.56	0.00	0.00
Na <sub>2</sub> O	0.00	0.00	0.00	0.00	0.00	0.00	0.00	0.00
K <sub>2</sub> O	0.00	0.00	0.00	0.00	0.00	0.00	0.00	0.00
Total	93.48	93.77	93.05	92.97	96.72	97.49	88.50	88.82
Si	2.02	2.05	2.04	2.04	3.02	2.99	2.64	2.65
Ti	0.00	0.00	0.00	0.00	0.00	0.00	0.00	0.00
Al	3.88	3.87	3.91	3.91	2.36	2.65	2.68	2.72
Fe <sup>+3</sup>	0.08	0.04	0.01	0.02	0.70	0.40	0.04	0.00
Fe <sup>+2</sup>	1.44	1.56	1.57	1.58	0.00	0.00	3.42	2.80
Mn	0.00	0.00	0.00	0.00	0.00	0.00	0.05	0.00
Mg	0.58	0.49	0.47	0.45	0.00	0.00	1.17	1.83
Ca	0.00	0.00	0.00	0.00	1.86	1.95	0.00	0.00
Na	0.00	0.00	0.00	0.00	0.00	0.00	0.00	0.00
K	0.00	0.00	0.00	0.00	0.00	0.00	0.00	0.00
XMg	0.28	0.23	0.23	0.22			0.25	0.40
XPs					0.64	0.36		

\* Analysis used for AvPT calculations (see Table 2)

Structural formulae have been calculated on the basis of 14 oxygens for chloritoid, 12 oxygens for epidote and 18 oxygens for chlorite.

Fe<sup>3+</sup> has been calculated by stoichiometry

**Table SM4a - Representative analyses of the main minerals in sample DM1281 (BIU)**

Analysis Site	White mica							Garnet					
	12.2Phe* // S <sub>m</sub>	12.1 Phe* // S <sub>m</sub>	6.88 Phe* // S <sub>m</sub>	8.3 Phe* // S <sub>m</sub>	9.23 Phe In Grt <sub>R</sub>	10.20 Ms In Grt <sub>C</sub>	6.51 Pa In Grt <sub>C</sub>	Grt 11.10 Core	6.3 Grt* Mantle	6b.1 Grt* Mantle	6.32 Grt* Mantle	10.13Grt* Mantle	6.1 Grt Rim
SiO <sub>2</sub>	53.17	52.77	52.96	53.02	53.11	47.77	47.39	37.07	37.28	37.86	37.43	37.71	37.85
TiO <sub>2</sub>	0.40	0.47	0.00	0.00	0.00	0.00	0.00	0.00	0.00	0.00	0.00	0.00	0.00
Al <sub>2</sub> O <sub>3</sub>	27.15	27.20	28.20	27.27	27.23	36.21	40.38	21.08	21.33	21.40	21.22	21.37	21.67
FeO	1.65	1.72	1.48	1.77	1.81	1.48	0.00	33.55	33.98	31.76	33.77	33.72	32.23
MnO	0.00	0.00	0.00	0.00	0.00	0.00	0.00	3.21	0.08	0.64	0.23	0.20	0.53
MgO	3.77	3.82	3.64	3.81	3.92	0.81	0.60	3.09	5.93	6.23	6.12	6.07	6.57
CaO	0.00	0.00	0.00	0.00	0.00	0.00	0.00	1.79	0.43	1.63	0.31	0.59	0.98
Na <sub>2</sub> O	0.00	0.00	0.00	0.51	0.66	2.11	7.35	0.00	0.00	0.00	0.00	0.00	0.00
K <sub>2</sub> O	10.34	10.52	10.32	10.38	9.42	8.20	0.40	0.00	0.00	0.00	0.00	0.00	0.00
Total	96.48	96.50	96.60	96.75	96.16	96.58	96.13	99.79	99.03	99.52	99.07	99.66	99.82
Si	3.47	3.45	3.45	3.46	3.47	3.10	3.01	2.99	2.977	2.992	2.985	2.988	2.980
Ti	0.02	0.02	0.00	0.00	0.00	0.00	0.00	0.00	0.00	0.00	0.00	0.00	0.00
Al	2.09	2.10	2.16	2.10	2.10	2.77	3.02	2.00	2.007	1.993	1.995	1.9957	2.010
Fe <sup>+3</sup>	0.00	0.00	0.00	0.00	0.00	0.00	0.00	0.02	0.040	0.022	0.036	0.0282	0.031
Fe <sup>+2</sup>	0.09	0.09	0.08	0.10	0.10	0.08	0.03	2.24	2.229	2.078	2.216	2.2069	2.092
Mn	0.00	0.00	0.00	0.00	0.00	0.00	0.00	0.22	0.006	0.043	0.016	0.0137	0.035
Mg	0.37	0.37	0.35	0.37	0.38	0.08	0.00	0.37	0.706	0.733	0.727	0.7172	0.770
Ca	0.00	0.00	0.00	0.00	0.00	0.00	0.00	0.15	0.037	0.138	0.026	0.0503	0.083
Na	0.00	0.00	0.00	0.06	0.08	0.27	0.91	0.00	0.00	0.00	0.00	0.00	0.00
K	0.86	0.88	0.86	0.86	0.79	0.68	0.03	0.00	0.00	0.00	0.00	0.00	0.00
XMg	0.80	0.80	0.82	0.79	0.79	0.49	0.00	0.12	0.24	0.25	0.24	0.24	0.26
XFe								0.75	0.75	0.69	0.74	0.74	0.70
XCa								0.05	0.01	0.05	0.01	0.02	0.03
XMn								0.07	0.00	0.01	0.01	0.01	0.01

\* Analysis used for AvPT calculations (see Table 2)

Structural formulae have been calculated on the basis of 11 oxygens for white mica and 12 oxygens for garnet.

Fe<sup>3+</sup> has been calculated by stoichiometry

**Table SM4b - Representative analyses of the main minerals in sample DM1281 (BIU)**

Analysis Site	Chloritoid				Chlorite		Staurolite	
	5.7 Cld*	6.49 Cld*	6.36 Cld*	6.33 Cld*	6.52 Chl	10.24 Chl	6b.5 St	11.26 St
	In Grt <sub>M</sub>	In Grt <sub>M</sub>	In Grt <sub>M</sub>	In Grt <sub>M</sub>	In Grt <sub>c</sub>	late	In Grt <sub>c</sub>	In Grt <sub>c</sub>
SiO <sub>2</sub>	25.88	25.58	25.75	25.54	27.56	24.03	30.70	29.57
TiO <sub>2</sub>	0.00	0.00	0.00	0.00	0.00	0.00	0.00	0.35
Al <sub>2</sub> O <sub>3</sub>	41.99	41.84	41.94	41.35	22.34	22.89	57.68	55.21
FeO	20.36	21.29	20.79	21.25	18.58	32.13	9.36	10.64
MnO	0.00	0.00	0.00	0.00	0.00	0.00	0.00	0.00
MgO	5.24	5.07	5.12	4.89	20.06	9.64	1.11	1.75
CaO	0.00	0.00	0.00	0.00	0.00	0.00	0.00	0.00
Na <sub>2</sub> O	0.00	0.00	0.00	0.00	0.00	0.00	0.00	0.00
K <sub>2</sub> O	0.00	0.00	0.00	0.00	0.00	0.00	0.00	0.00
Total	93.47	93.78	93.60	93.02	88.54	88.70	98.85	97.52
Si	2.07	2.04	2.06	2.06	2.77	2.61	4.26	4.17
Ti	0.00	0.00	0.00	0.00	0.00	0.00	0.00	0.04
Al	3.95	3.94	3.95	3.92	2.65	2.92	9.43	9.17
Fe <sup>+3</sup>	0.00	0.00	0.00	0.00	0.00	0.00	0.00	0.00
Fe <sup>+2</sup>	1.36	1.42	1.39	1.43	1.56	2.91	1.09	1.25
Mn	0.00	0.00	0.00	0.00	0.00	0.00	0.00	0.00
Mg	0.62	0.60	0.61	0.59	3.01	1.56	0.23	0.37
Ca	0.00	0.00	0.00	0.00	0.00	0.00	0.00	0.00
Na	0.00	0.00	0.00	0.00	0.00	0.00	0.00	0.00
K	0.00	0.00	0.00	0.00	0.00	0.00	0.00	0.00
XMg	0.31	0.30	0.31	0.29	0.66	0.35	0.18	0.23

\* Analysis used for AvPT calculations (see Table 2)

Structural formulae have been calculated on the basis of 14 oxygens for chloritoid, 18 oxygens for chlorite and 12 oxygens for staurolite.

Fe<sup>3+</sup> has been calculated by stoichiometry



**Table SM5a - Representative analyses of the main minerals in sample DM1504 (RSU)**

Analysis	White mica						Garnet					
	2.34 Phe*	6.21 Phe*	6.16 Phe*	6.3 Phe*	7.20 Ms	6.15 Pa	2.16 Grt	2.8 Grt	2.2 Grt*	2.26 Grt*	1.19 Grt*	2.1 Grt*
Site	In Grt <sub>R</sub>	// S <sub>m</sub>	// S <sub>m</sub>	In Cl <sub>d</sub>	late	⊥ S <sub>m</sub>	Core	Mantle	Rim	Rim	Rim	Rim
SiO <sub>2</sub>	51.86	52.08	51.42	52.38	47.24	48.40	37.09	37.09	37.47	36.88	37.19	37.21
TiO <sub>2</sub>	0.00	0.00	0.00	0.00	0.00	0.00	0.00	0.00	0.00	0.00	0.00	0.00
Al <sub>2</sub> O <sub>3</sub>	27.60	27.64	27.34	27.47	35.02	39.39	20.78	20.52	20.39	20.48	20.87	20.40
FeO	3.79	3.66	4.31	3.85	2.85	0.65	30.05	29.49	30.70	31.04	29.44	31.13
MnO	0.00	0.00	0.00	0.00	0.00	0.00	3.99	2.91	1.66	1.83	2.79	1.72
MgO	3.01	3.01	3.05	3.19	0.67	0.00	2.09	2.30	2.14	2.37	2.35	2.21
CaO	0.00	0.00	0.00	0.00	0.00	0.00	5.63	7.15	7.13	6.39	7.19	6.54
Na <sub>2</sub> O	0.58	0.00	0.78	0.72	1.92	7.68	0.00	0.00	0.00	0.00	0.00	0.00
K <sub>2</sub> O	9.75	10.35	9.46	9.32	8.33	0.24	0.00	0.00	0.00	0.00	0.00	0.00
Total	96.59	96.74	96.36	96.93	96.02	96.37	99.63	99.46	99.50	98.99	99.83	99.22
Si	3.42	3.43	3.41	3.43	3.11	3.06	2.99	2.98	3.02	2.98	2.98	3.01
Ti	0.00	0.00	0.00	0.00	0.00	0.00	0.00	0.00	0.00	0.00	0.00	0.00
Al	2.14	2.14	2.13	2.12	2.72	2.94	1.97	1.94	1.93	1.95	1.97	1.94
Fe <sup>+3</sup>	0.00	0.00	0.00	0.00	0.00	0.00	0.05	0.09	0.04	0.08	0.08	0.05
Fe <sup>+2</sup>	0.21	0.20	0.24	0.21	0.16	0.03	1.98	1.89	2.03	2.02	1.89	2.05
Mn	0.00	0.00	0.00	0.00	0.00	0.00	0.27	0.20	0.11	0.13	0.19	0.12
Mg	0.30	0.29	0.30	0.31	0.07	0.00	0.25	0.28	0.26	0.29	0.28	0.27
Ca	0.00	0.00	0.00	0.00	0.00	0.00	0.49	0.62	0.62	0.55	0.62	0.57
Na	0.07	0.00	0.10	0.09	0.25	0.94	0.00	0.00	0.00	0.00	0.00	0.00
K	0.82	0.87	0.80	0.78	0.70	0.02						
XMg	0.59	0.59	0.56	0.60	0.295	0.00	0.08	0.09	0.09	0.10	0.09	0.09
XFe							0.66	0.64	0.67	0.68	0.64	0.68
XCa							0.16	0.21	0.20	0.19	0.21	0.19
XMn							0.09	0.07	0.04	0.04	0.06	0.04

\* Analysis used for AvPT calculations (see Table 2)

Structural formulae have been calculated on the basis of 11 oxygens for white mica and 12 oxygens for garnet.

Fe<sup>3+</sup> has been calculated by stoichiometry

**Table SM5b - Representative analyses of the main minerals in sample DM1504 (RSU)**

Analysis	Chloritoid							Jadeite	Glaucoephane
	7.9 Cl <sub>d</sub>	1.22 Cl <sub>d</sub>	1.20 Cl <sub>d</sub>	6.8 Cl <sub>d</sub> *	2.35 Cl <sub>d</sub> *	4.4 Cl <sub>d</sub> *	2.32 Cl <sub>d</sub> *	2.44 J <sub>d</sub> *	2.52 G <sub>ln</sub> *
Site	Core	In Grt <sub>c</sub>	In Grt <sub>M</sub>	Rim	In Grt <sub>R</sub>	In Grt <sub>R</sub>	In Grt <sub>R</sub>	In Grt <sub>R</sub>	In Grt <sub>R</sub>
SiO <sub>2</sub>	25.22	25.22	25.11	25.18	25.14	24.77	24.58	56.79	55.54
TiO <sub>2</sub>	0.00	0.00	0.00	0.00	0.00	0.00	0.00	0.00	0.00
Al <sub>2</sub> O <sub>3</sub>	40.44	40.63	40.61	40.21	40.66	40.29	39.98	17.49	9.58
FeO	24.17	23.91	23.74	23.86	23.60	23.61	23.43	8.69	18.07
MnO	0.54	0.00	0.46	0.00	0.00	0.42	0.42	0.00	0.00
MgO	3.25	3.61	3.80	4.07	3.69	3.84	3.81	0.00	7.34
CaO	0.00	0.00	0.00	0.00	0.00	0.00	0.00	0.47	0.76
Na <sub>2</sub> O	0.00	0.00	0.00	0.00	0.00	0.00	0.00	14.62	6.53
K <sub>2</sub> O	0.00	0.00	0.00	0.00	0.00	0.00	0.00	0.00	0.00
Total	93.62	93.38	93.72	93.32	93.09	92.93	92.22	98.06	97.83
Si	2.05	2.05	2.03	2.04	2.05	2.02	2.05	2.00	7.83
Ti	0.00	0.00	0.00	0.00	0.00	0.00	0.00	0.00	0.00
Al	3.87	3.89	3.87	3.85	3.90	3.87	3.87	0.73	1.59
Fe <sup>+3</sup>	0.02	0.01	0.06	0.07	0.01	0.09	0.04	0.26	0.53
Fe <sup>+2</sup>	1.62	1.61	1.54	1.55	1.60	1.52	1.56	0.00	1.60
Mn	0.04	0.00	0.03	0.00	0.00	0.03	0.03	0.00	0.00
Mg	0.39	0.44	0.46	0.49	0.45	0.47	0.46	0.00	1.54
Ca	0.00	0.00	0.00	0.00	0.00	0.00	0.00	0.02	0.11
Na	0.00	0.00	0.00	0.00	0.00	0.00	0.00	1.00	1.79
K	0.00	0.00	0.00	0.00	0.00	0.00	0.00	0.00	0.00
XMg	0.20	0.21	0.23	0.23	0.22	0.23	0.23	0.00	0.48
XNa								0.98	0.94

\* Analysis used for AvPT calculations (see Table 2)

Structural formulae have been calculated on the basis of 14 oxygens for chloritoid, 6 oxygens for jadeite and 24 oxygens for glaucophane.

Fe<sup>3+</sup> has been calculated by stoichiometry

**Table SM6a - Representative analyses of the main minerals in sample DM1565 (DSU)**

Analysis	White mica						Pre-Alpine Garnet (Grt <sub>1</sub> )			Alpine Garnet (Grt <sub>2</sub> )			
	5.12 Phe*	5.6 Phe*	3.6 Phe*	2.27 Phe	8.18 Ms	5.3 Pa	1.16 Grt	t 1.6 Grt	1.30 Grt	3.13 Grt	3.15 Grt*	3.11 Grt*	7.1 Grt*
Site	// S <sub>m</sub>	// S <sub>m</sub>	// S <sub>m</sub>	ln (St)	Late	Late	Core	Mantle	Rim	Core	Rim	Rim	Rim
SiO <sub>2</sub>	54.76	54.59	55.21	51.93	47.53	47.68	36.89	36.86	36.61	37.28	37.58	37.53	37.37
TiO <sub>2</sub>	0.00	0.00	0.00	0.00	0.69	0.00	0.00	0.00	0.00	0.00	0.00	0.00	0.00
Al <sub>2</sub> O <sub>3</sub>	25.84	25.43	25.42	28.58	37.05	40.10	21.05	20.54	20.64	20.98	21.08	20.93	21.39
FeO	2.57	2.20	2.72	2.77	0.94	0.00	34.38	35.62	35.81	34.17	31.62	29.92	30.68
MnO	0.00	0.00	0.00	0.00	0.00	0.00	2.68	0.65	1.92	1.07	0.75	0.81	0.78
MgO	4.20	4.34	4.17	3.02	0.55	0.00	1.94	2.33	2.66	0.95	1.37	1.11	1.13
CaO	0.00	0.00	0.00	0.00	0.00	0.00	2.77	3.24	1.46	5.30	7.09	9.11	8.59
Na <sub>2</sub> O	0.00	0.50	0.00	0.59	2.33	8.40	0.00	0.00	0.00	0.00	0.00	0.00	0.00
K <sub>2</sub> O	9.41	9.78	9.19	9.53	7.76	0.00	0.00	0.00	0.00	0.00	0.00	0.00	0.00
Total	96.78	96.85	96.71	96.42	96.84	96.18	99.71	99.24	99.10	99.75	99.48	99.42	99.93
Si	3.55	3.55	3.58	3.40	3.07	3.01	2.99	3.00	2.99	3.03	3.03	3.02	3.00
Ti	0.00	0.00	0.00	0.00	0.03	0.00	0.00	0.00	0.00	0.00	0.00	0.00	0.00
Al	1.97	1.95	1.94	2.21	2.82	2.98	2.01	1.97	1.99	2.01	2.00	1.99	2.02
Fe <sup>+3</sup>	0.00	0.00	0.00	0.00	0.00	0.00	0.00	0.03	0.04	0.00	0.00	0.00	0.00
Fe <sup>+2</sup>	0.14	0.12	0.15	0.15	0.05	0.00	2.33	2.39	2.40	2.32	2.13	2.02	2.06
Mn	0.00	0.00	0.00	0.00	0.00	0.00	0.18	0.05	0.13	0.07	0.05	0.06	0.05
Mg	0.41	0.42	0.40	0.30	0.05	0.00	0.23	0.28	0.32	0.11	0.16	0.13	0.13
Ca	0.00	0.00	0.00	0.00	0.00	0.00	0.24	0.28	0.13	0.46	0.61	0.79	0.74
Na	0.00	0.06	0.00	0.07	0.29	1.03	0.00	0.00	0.00	0.00	0.00	0.00	0.00
K	0.78	0.81	0.76	0.80	0.64	0.00	0.00	0.00	0.00	0.00	0.00	0.00	0.00
XMg	0.744	0.778	0.732	0.66	0.511	0.00	0.08	0.09	0.11	0.04	0.06	0.05	0.05
XFe							0.78	0.80	0.80	0.78	0.72	0.67	0.69
XCa							0.08	0.09	0.04	0.16	0.21	0.26	0.25
XMn							0.06	0.02	0.04	0.03	0.02	0.02	0.02

\* Analysis used for AvPT calculations (see Table 2)

Structural formulae have been calculated on the basis of 11 oxygens for white mica and 12 oxygens for garnet.

Fe<sup>3+</sup> has been calculated by stoichiometry

**Table SM6b - Representative analyses of the main minerals in sample DM1565 (DSU)**

Analysis	Chloritoid			Chlorite
	2.3 Cl <sub>d</sub> *	2.32 Cl <sub>d</sub> **	2.25 Cl <sub>d</sub>	8.14 Chl
Site	ln (St)	ln (St)	ln (St)	Late
SiO <sub>2</sub>	25.07	24.94	25.16	24.97
TiO <sub>2</sub>	0.00	0.00	0.00	0.00
Al <sub>2</sub> O <sub>3</sub>	41.12	41.39	40.95	21.77
FeO	24.15	24.13	25.23	29.31
MnO	0.00	0.00	0.00	0.00
MgO	2.80	2.89	2.52	11.99
CaO	0.00	0.00	0.00	0.00
Na <sub>2</sub> O	0.00	0.00	0.00	0.00
K <sub>2</sub> O	0.00	0.00	0.00	0.00
Total	93.14	93.35	93.87	88.04
Si	2.049	2.032	2.048	2.685
Ti	0.00	0.00	0.00	0.00
Al	3.959	3.974	3.928	2.758
Fe <sup>+3</sup>	0.00	0.00	0.00	0.00
Fe <sup>+2</sup>	1.650	1.644	1.718	2.636
Mn	0.00	0.00	0.00	0.00
Mg	0.342	0.350	0.306	1.922
Ca	0.00	0.00	0.00	0.00
Na	0.00	0.00	0.00	0.00
K	0.00	0.00	0.00	0.00
XMg	0.17	0.18	0.15	0.42

\* Analysis used for AvPT calculations (see Table 2)

Structural formulae have been calculated on the basis of 14 oxygens for chloritoid and 18 oxygens for chlorite.

Fe<sup>3+</sup> has been calculated by stoichiometry

**Table SM7a. Independent set of reactions modelled by AvPT and used to estimate P-T conditions**

<b>Sample DM1485 (PU)</b>	
Phe(6.1)-Grt(1.22)-Ctd(1.49)-Chl(4.7)-Qz-H <sub>2</sub> O	Phe(2.31)-Grt(1.2)-Ctd(1.48)-Chl(4.8)-Qz-H <sub>2</sub> O
1) ames + 2q = py + mctd + 3H <sub>2</sub> O	1) ames + 2q = py + mctd + 3H <sub>2</sub> O
2) 5alm + 5ames + 4q = 4py + 8mctd + 3daph	2) fctd + daph + 2q = 2alm + 5H <sub>2</sub> O
3) 23alm + 15ames + 12q = 20py + 24fctd + 9daph	3) 5alm + 5ames + 4q = 4py + 8mctd + 3daph
4) 3cel + 5alm + 3ames = 3mu + 5py + 3daph	4) 3cel + 5alm + 3ames = 3mu + 5py + 3daph
Phe(6.11)-Grt(1.21)-Ctd(2.29)-Chl(4.9)-Qz-H <sub>2</sub> O	Phe(6.6)-Grt(1.23)-Ctd(1.33)-Chl(3.7)-Qz-H <sub>2</sub> O
1) ames + 2q = py + mctd + 3H <sub>2</sub> O	1) ames + 2q = py + mctd + 3H <sub>2</sub> O
2) fctd + daph + 2q = 2alm + 5H <sub>2</sub> O	2) fctd + daph + 2q = 2alm + 5H <sub>2</sub> O
3) 5alm + 5ames + 4q = 4py + 8mctd + 3daph	3) 3mctd + 3daph + 6q = py + 5alm + 15H <sub>2</sub> O
4) 3mu + py + 2ames + 4q = 3cel + 8mctd	4) 3mu + py + 2ames + 4q = 3cel + 8mctd
5) 3cel + alm = 3fcel + py	5) 3cel + alm = 3fcel + py
<b>Sample DM1667c (SCU)</b>	
Phe(7.17)-Grt(2.24)-Ctd(1.5)-Lws-Qz-H <sub>2</sub> O	Phe(10.1)-Grt(9.22)-Ctd(2.52)-Lws-Qz-H <sub>2</sub> O
1) py + 3law = gr + 3mctd + 3q + 3H <sub>2</sub> O	1) py + 3law = gr + 3mctd + 3q + 3H <sub>2</sub> O
2) alm + 3law = gr + 3fctd + 3q + 3H <sub>2</sub> O	2) alm + 3law = gr + 3fctd + 3q + 3H <sub>2</sub> O
3) fcel + 2fctd = mu + alm + 2H <sub>2</sub> O	3) 3cel + 2gr + 12mctd + 6q = 3mu + 5py + 6law
4) 3cel + 2gr + 12mctd + 6q = 3mu + 5py + 6law	4) 15cel + 2gr + 12fctd + 6q = 3mu + 12fcel + 5py + 6law
Phe(10.9)-Grt(2.25)-Ctd(2.49)-Lws-Qz-H <sub>2</sub> O	Phe(1.18)-Grt(9.1)-Ctd(2.40)-Lws-Qz-H <sub>2</sub> O
1) py + 3law = gr + 3mctd + 3q + 3H <sub>2</sub> O	1) py + 3law = gr + 3mctd + 3q + 3H <sub>2</sub> O
2) alm + 3law = gr + 3fctd + 3q + 3H <sub>2</sub> O	2) alm + 3law = gr + 3fctd + 3q + 3H <sub>2</sub> O
3) 3cel + 2gr + 12mctd + 6q = 3mu + 5py + 6law	3) 3cel + 2gr + 12mctd + 6q = 3mu + 5py + 6law
<b>Sample DM1281 (BIU)</b>	
Phe(12.2)-Grt(6.3)-Ctd(5.7)-Ky-Coe-H <sub>2</sub> O	Phe(12.1)-Grt(6b.1)-Ctd(6.49)-Ky-Coe-H <sub>2</sub> O
1) 3fctd + 2coe = alm + 2ky + 3H <sub>2</sub> O	1) 3fctd + 2coe = alm + 2ky + 3H <sub>2</sub> O
2) 3mu + py + 4coe = 3cel + 4ky	2) 3mu + py + 4coe = 3cel + 4ky
3) 3cel + alm = 3fcel + py	3) 3cel + alm = 3fcel + py
Phe(6.88)-Grt(6.32)-Ctd(6.36)-Ky-Coe-H <sub>2</sub> O	Phe(8.3)-Grt(10.13)-Ctd(6.33)-Ky-Coe-H <sub>2</sub> O
1) 3fctd + 2coe = alm + 2ky + 3H <sub>2</sub> O	1) 3fctd + 2coe = alm + 2ky + 3H <sub>2</sub> O
2) 3mu + py + 4coe = 3cel + 4ky	2) pa = ky + jd + H <sub>2</sub> O
3) 3cel + alm = 3fcel + py	3) 3mu + py + 4coe = 3cel + 4ky
	4) 3cel + alm = 3fcel + py

**Table SM7b. Independent set of reactions modelled by AvPT and used to estimate P-T conditions****Sample DM1504 (RSU)**Phe(2.34)-Grt(2.2)-Ctd(2.35)-Gln(2.52)-Jd(2.44)-Lws-Qz-H<sub>2</sub>O

- 1)  $py + 3law = gr + 3mctd + 3q + 3H_2O$
- 2)  $alm + 3law = gr + 3fctd + 3q + 3H_2O$
- 3)  $cel + 2mctd = mu + py + 2H_2O$
- 4)  $3mctd + 2jd + 2q = 2pa + py + H_2O$
- 5)  $fccl + 2fctd = mu + alm + 2H_2O$
- 6)  $3pa + fgl = 3fctd + 5jd + 4q + H_2O$
- 7)  $27mu + 9cel + 4spss + 12fgl + 12law = 36fccl + 24pa + 3py + 4gr + 12mnctd$

Phe(6.16)-Grt(1.19)-Ctd(6.8)-Gln(2.52)-Jd(2.44)-Lws-Qz-H<sub>2</sub>O

- 1)  $py + 3law = gr + 3mctd + 3q + 3H_2O$
- 2)  $alm + 3law = gr + 3fctd + 3q + 3H_2O$
- 3)  $cel + 2mctd = mu + py + 2H_2O$
- 4)  $3mctd + 2jd + 2q = 2pa + py + H_2O$
- 5)  $fccl + 2fctd = mu + alm + 2H_2O$
- 6)  $6fccl + 2pa + py + 2jd = 3mu + 3cel + 2fgl$

Phe(6.21)-Grt(2.26)-Ctd(4.4)-Gln(2.52)-Jd(2.44)-Lws-Qz-H<sub>2</sub>O

- 1)  $py + 3law = gr + 3mctd + 3q + 3H_2O$
- 2)  $alm + 3law = gr + 3fctd + 3q + 3H_2O$
- 3)  $cel + 2mctd = mu + py + 2H_2O$
- 4)  $fccl + 2fctd = mu + alm + 2H_2O$
- 5)  $12fccl + py + 4mctd + 8jd + 4q = 5mu + 7cel + 4fgl$

Phe(6.3)-Grt(2.1)-Ctd(2.32)-Gln(2.52)-Jd(2.44)-Lws-Qz-H<sub>2</sub>O

- 1)  $py + 3law = gr + 3mctd + 3q + 3H_2O$
- 2)  $alm + 3law = gr + 3fctd + 3q + 3H_2O$
- 3)  $cel + 2mctd = mu + py + 2H_2O$
- 4)  $3mctd + 2jd + 2q = 2pa + py + H_2O$
- 5)  $fccl + 2fctd = mu + alm + 2H_2O$
- 6)  $3pa + fgl = 3fctd + 5jd + 4q + H_2O$
- 7)  $6fccl + 2pa + py + gr + 2acm = 3mu + 3cel + andr + 2fgl$

**Sample DM1565 (DSU)**Phe(5.12)-Grt(3.15)-Ctd(2.3)-Lws-Qz-H<sub>2</sub>O

- 1)  $py + 3law = gr + 3mctd + 3q + 3H_2O$
- 2)  $alm + 3law = gr + 3fctd + 3q + 3H_2O$
- 3)  $3cel + 2gr + 12mctd + 6q = 3mu + 5py + 6law$

Phe(3.6)-Grt(7.1)-Ctd(2.25)-Lws-Qz-H<sub>2</sub>O

- 1)  $py + 3law = gr + 3mctd + 3q + 3H_2O$
- 2)  $alm + 3law = gr + 3fctd + 3q + 3H_2O$
- 3)  $3cel + 2gr + 12mctd + 6q = 3mu + 5py + 6law$

Phe(5.6)-Grt(3.11)-Ctd(2.32)-Lws-Qz-H<sub>2</sub>O

- 1)  $py + 3law = gr + 3mctd + 3q + 3H_2O$
- 2)  $alm + 3law = gr + 3fctd + 3q + 3H_2O$
- 3)  $3cel + 2gr + 12fctd + 6q = 3mu + py + 4alm + 6law$

**Table SM8 - Mass balance of the staurolite-forming reactions**

**0.264 Chl + 3.496 Ky + 0.123 Grt<sub>c</sub> = 1.000 St**

	Reactants			Products			
Phases	Chl 6.68	Ky 6.66	Grt <sub>c</sub> 6.15	St 6.67	Σreact	Σprod	Residuals
<b>coeff</b>	<b>-0.264</b>	<b>3.496</b>	<b>-0.123</b>	<b>1.000</b>			
SiO <sub>2</sub>	2.59	1.00	2.98	3.94	-3.940	4.544	0.604
Al <sub>2</sub> O <sub>3</sub>	1.47	1.00	1.00	4.61	-4.610	4.006	-0.604
FeO	2.48	0.00	2.30	1.51	-1.510	0.936	-0.574
MnO	0.00	0.00	0.10	0.00	0.000	0.012	0.012
MgO	1.93	0.00	0.45	0.29	-0.290	0.564	0.274
CaO	0.00	0.00	0.14	0.01	-0.008	0.018	0.010
H <sub>2</sub> O	4.00	0.00	0.00	1.00	-1.000	1.055	0.055

**0.263 Chl + 3.712 Ky + 0.064 Grt<sub>c</sub> = 1.000 St**

	Reactants			Products			
Phases	Chl 11.34	Ky 11.32	Grt <sub>c</sub> 11.6	St 11.34	Σreact	Σprod	Residuals
<b>coeff</b>	<b>-0.263</b>	<b>-3.712</b>	<b>-0.064</b>	<b>1.000</b>			
SiO <sub>2</sub>	2.71	1.00	2.90	4.11	-4.110	4.610	0.500
Al <sub>2</sub> O <sub>3</sub>	1.56	1.00	1.00	4.69	-4.685	4.185	-0.500
FeO	2.43	0.00	2.19	1.27	-1.270	0.779	-0.491
MnO	0.00	0.00	0.10	0.00	0.000	0.006	0.006
MgO	1.75	0.00	0.54	0.26	-0.260	0.494	0.234
CaO	0.00	0.00	0.16	0.00	0.000	0.010	0.010
H <sub>2</sub> O	4.00	0.00	0.00	1.00	-1.000	1.052	0.052

**0.211 Chl + 3.620 Ky + 0.131 Grt<sub>M</sub> = 1.000 St**

	Reactants			Products			
Phases	Chl 6.52	Ky 6.53	Grt <sub>M</sub> 6.21	St 6.50	Σreact	Σprod	Residuals
<b>coeff</b>	<b>-0.211</b>	<b>-3.620</b>	<b>-0.131</b>	<b>1.000</b>			
SiO <sub>2</sub>	2.77	1.00	2.99	4.04	-4.040	4.598	0.558
Al <sub>2</sub> O <sub>3</sub>	1.33	1.00	1.00	4.59	-4.590	4.032	-0.558
FeO	1.56	0.00	2.05	1.23	-1.230	0.599	-0.631
MnO	0.00	0.00	0.08	0.00	0.000	0.010	0.010
MgO	3.01	0.00	0.67	0.46	-0.460	0.724	0.264
CaO	0.00	0.00	0.17	0.00	0.000	0.022	0.022
H <sub>2</sub> O	4.00	0.00	0.00	1.00	-1.000	0.846	-0.154

Reactions were balanced using the least-squares method. Stoichiometric coefficients and compositions are expressed in moles.  $\Sigma_{react}$ : overall composition of the reactants;  $\Sigma_{prod}$ : overall composition of the products;  $Residuals$ : residual vector from the method of least squares (molar bulk composition of the product - molar bulk composition of the reactants).